

# Optical Design Considerations for High Conversion Efficiency in Photovoltaics

*Vidya Ganapati*



Electrical Engineering and Computer Sciences  
University of California at Berkeley

Technical Report No. UCB/EECS-2015-61

<http://www.eecs.berkeley.edu/Pubs/TechRpts/2015/EECS-2015-61.html>

May 12, 2015

Copyright © 2015, by the author(s).  
All rights reserved.

Permission to make digital or hard copies of all or part of this work for personal or classroom use is granted without fee provided that copies are not made or distributed for profit or commercial advantage and that copies bear this notice and the full citation on the first page. To copy otherwise, to republish, to post on servers or to redistribute to lists, requires prior specific permission.

# Optical Design Considerations for High Conversion Efficiency in Photovoltaics

by

Vidya Ganapati

A dissertation submitted in partial satisfaction of the

requirements for the degree of

Doctor of Philosophy

in

Engineering - Electrical Engineering and Computer Sciences

in the

Graduate Division

of the

University of California, Berkeley

Committee in charge:

Professor Eli Yablonovitch, Chair  
Professor Connie J. Chang-Hasnain  
Professor Xiang Zhang

Spring 2015

# Optical Design Considerations for High Conversion Efficiency in Photovoltaics

Copyright 2015  
by  
Vidya Ganapati

## Abstract

Optical Design Considerations for High Conversion Efficiency in Photovoltaics

by

Vidya Ganapati

Doctor of Philosophy in Engineering - Electrical Engineering and Computer Sciences

University of California, Berkeley

Professor Eli Yablonovitch, Chair

This thesis explores ways to create highly efficient, thin-film solar cells. Both high short circuit current density and high open circuit voltage are required for high efficiency in photovoltaics. High current is achieved by absorbing most of the above bandgap photons, and then extracting the resulting electrons and holes. To achieve high absorption in thin films, surface texturing is necessary. Surface texturing allows for absorption enhancement due to total internal reflection, known as light trapping. However, in subwavelength-thick solar cells ( $\approx 100$  nm thick), the theory of light trapping is not understood, and both the maximum achievable absorption and the optimal surface texture are open questions. Computational electromagnetic optimization is used to find surface textures yielding an absorption enhancement of 40 times the absorption in a flat solar cell, the highest enhancement achieved in a subwavelength-thick solar cell with a realistic index of refraction. The optimization makes use of adjoint gradient methods, which allow the problem of designing a 3D surface to be computationally tractable.

However, while high current requires high absorption, high voltage requires re-emission of the absorbed photons out of the front surface of the photovoltaic cell. This re-emission out the front of the solar cell is required by the detailed balance formalism outlined by Shockley and Quisser in 1961. At the open circuit voltage condition, where no current is collected, ideally all absorbed photons are eventually re-emitted out the front surface of the solar cell. The small escape cone for a semiconductor/air interface, as described by Snell's law, makes it difficult for the photon to escape out of the front surface; it is much more likely for the luminescent photon to be lost to an absorbing back substrate. Thus, a back reflector on a solar cell is crucial to obtaining high voltage, as it helps the internally emitted photons in the cell escape out of the front surface. The open circuit voltage difference between a solar cell with a back mirror and a solar cell with an absorbing substrate is quantified, and it is found that the benefit of using a back mirror depends on the absorptivity of the solar cell material. The back mirror concept is extended to the sub-cells of a multijunction cell, and an air gap as an "intermediate" reflector is proposed and analyzed. In a dual junction solar cell, it is shown that proper mirror design with air gaps and antireflection coatings leads to

an increase in open circuit voltage, resulting in a  $\approx 5\%$  absolute efficiency increase in the solar cell.

Finally, it is shown that these concepts in high efficiency solar cells can be extended to thermophotovoltaics. In solar photovoltaics, radiation from the sun is converted to electricity with photovoltaic cells. In thermophotovoltaics, radiation from a local heat source is converted to electricity with photovoltaic cells. This method of converting heat to electricity can be extremely efficient if sub-bandgap photons are reflected back and re-absorbed by the hot source (which is usually around  $1200^\circ\text{C}$ ). Greater than 50% efficient heat to electricity conversion with thermophotovoltaics is possible if the photovoltaic cells have good back mirrors.

To my mother, father, and brother, for being my #1 fans.

# Contents

<b>Contents</b>	<b>ii</b>
<b>List of Figures</b>	<b>iv</b>
<b>List of Tables</b>	<b>x</b>
<b>1 Introduction</b>	<b>1</b>
<b>2 The Voltage Boost Enabled by a Back Mirror</b>	<b>3</b>
2.1 Optical Model of the Solar Cell . . . . .	3
2.2 Open-Circuit Voltage, $V_{oc}$ . . . . .	4
2.3 Voltage Penalty for No Back Mirror, $\Delta V_{nm}$ . . . . .	8
2.4 Chapter Summary . . . . .	17
<b>3 Air Gaps as Intermediate Selective Reflectors for Multi-Bandgap Cells</b>	<b>18</b>
3.1 Theory . . . . .	19
3.2 Structures . . . . .	21
3.3 Optimal 2-Bandgap Cell . . . . .	26
3.4 Optimal Multi-Bandgap Cells . . . . .	29
3.5 Practical Considerations . . . . .	29
3.6 Chapter Summary . . . . .	30
<b>4 Design of Subwavelength Light Trapping Textures</b>	<b>31</b>
4.1 Optimization Algorithm . . . . .	33
4.2 Adjoint Method for Electromagnetic Optimization . . . . .	35
4.3 Optimization Results . . . . .	40
4.4 Applying Manufacturing Constraints . . . . .	45
4.5 Chapter Summary . . . . .	47
<b>5 Thermophotovoltaics with the Photovoltaic Cell as the Spectral Filter</b>	<b>58</b>
5.1 Theory . . . . .	62
5.2 Efficiency of Single Bandgap Thermophotovoltaics . . . . .	65
5.3 Efficiency of Dual Bandgap Thermophotovoltaics . . . . .	65

5.4	Selective Source and Reflective Back Mirror . . . . .	66
5.5	Reaching Carnot Efficiency . . . . .	68
5.6	Chapter Summary . . . . .	69
<b>6</b>	<b>Concentrating Solar Technologies</b>	<b>74</b>
6.1	Single Bandgap Cells Under Concentration . . . . .	75
6.2	Dual Bandgap Cells Under Concentration . . . . .	75
6.3	Solar Thermophotovoltaics . . . . .	77
6.4	Chapter Summary . . . . .	78
	<b>Bibliography</b>	<b>80</b>

# List of Figures

2.1	The $J - V$ characteristic for an ideal solar cell with bandgap $E_g = 1.43$ eV. The maximum power point (MPP) is indicated in red. The open-circuit voltage is the $x$ -intercept, and the short-circuit current density is the $y$ -intercept. The efficiency at the MPP is 33.4%. . . . .	5
2.2	The relationship between power and voltage. We use a maximum power point tracker (MPPT) to continually operate the cell at the maximum power point voltage. . . . .	6
2.3	Diagram of a solar cell at open circuit voltage with semiconductor index of refraction $n_s = 3.5$ on an index-matched substrate (analogous to the case of a GaAs cell on a GaAs substrate). Incident photons (shown in yellow) refract towards the normal inside the semiconductor, due to the index mismatch. These incident photons are absorbed and then re-emitted (the re-emitted photons have energies close to the bandgap, and are drawn in red to show the downshift in energy). Most of these internally luminescent photons escape from the bottom surface into the index-matched substrate, as the probability being in the escape cone of the semiconductor/air interface is low. . . . .	7
2.4	Diagram of the case of a solar cell on a perfectly reflecting back mirror; in this case, at open circuit, all the incident photons are absorbed and eventually emitted out of the front surface. . . . .	7
2.5	The breakdown of internal photons in a GaAs cell, grown on a substrate for a 1 $\mu\text{m}$ thick cell. The spectrum is shown for total internal emission, normalized to unity (blue). Of the total internal spectrum, the fraction of photons reabsorbed by the cell (purple), photons escaping out the front surface (red), and photons emitted in the substrate (yellow), are shown. . . . .	12
2.6	The breakdown of internal photons in a GaAs cell, grown on a substrate for a 100 nm thick cell. The spectrum is shown for total internal emission, normalized to unity (blue). Of the total internal spectrum, the fraction of photons reabsorbed by the cell (purple), photons escaping out the front surface (red), and photons emitted in the substrate (yellow), are shown. . . . .	13

2.7	The absorption coefficient as a function of photon energy, around the bandedge of GaAs. The blue crosses represent the data from [17], showing a bump around the bandedge due to absorption at the exciton energy. The absorption coefficient fit described in [5] ignores this exciton bump. We use the fit in [5], except at the bandedge, where we model the exciton bump with a fourth degree polynomial. The red line shows our fit. . . . .	14
2.8	The voltage penalty $\Delta V_{nm}$ for a GaAs cell on an index-matched substrate, as a function of the re-absorption probability $P_{abs}$ , as given by Eqns. (2.7), (2.19), and (2.22). Each value of $P_{abs}$ corresponds to a certain cell thickness $L$ , which is denoted on the top $x$ -axis of the graph. Horizontal lines indicate where $\Delta V_{nm} = 0$ , for the case of a perfect back reflector, and where $\Delta V_{nm} = -13.2mV$ , for the case of an air interface ( $n = 1$ ) at the back of the cell. For a 1 $\mu m$ cell on substrate, $\Delta V_{nm} = -78mV$ , and for a 100 nm cell on substrate, $\Delta V_{nm} = -93mV$ . In the limit of a cell that is optically thin to the internal luminescence ( $P_{abs} \rightarrow 0$ ), $\Delta V_{nm} = -98mV$ , consistent with our derived lower bound for $\eta_{ext}$ . In the limit of a cell that is optically thick to the internal luminescence ( $P_{abs} \rightarrow 1$ ), we see that $\Delta V_{nm} = -66mV$ , consistent with our derived upper bound for $\eta_{ext}$ . . . . .	16
3.1	Bandgaps of different materials are placed in a stack, from largest bandgap on top to smallest on the bottom in a multi-bandgap cell. The question arises, how do we design intermediate mirrors that reflect internally luminescent photons without impeding the transmission of externally incident photons? . . . . .	19
3.2	Case (1); a dual bandgap solar cell without an intermediate or a back mirror; the top cell, bottom cell, and substrate are index matched with $n_s = 3.5$ . . . . .	22
3.3	The efficiencies as a function of top and bottom bandgap for Case (1), a dual junction solar cell without an intermediate or a back mirror; the cells are assumed to be optically thin to the internally luminescent photons. . . . .	23
3.4	Case (2); a dual bandgap solar cell without an intermediate mirror but with a back mirror; the top and bottom cells are index matched with $n_s = 3.5$ . . . . .	24
3.5	The efficiencies as a function of top and bottom bandgap for Case (2), a dual junction solar cell without an intermediate or a back mirror. . . . .	25
3.6	Case (3); a dual bandgap solar cell with an air gap intermediate mirror, with perfect antireflection coatings and a perfect back mirror. . . . .	26
3.7	The efficiencies as a function of top and bottom bandgap for Case (3), a dual junction cell with an air gap intermediate mirror and perfect back mirror. . . . .	27
3.8	Tandem cell efficiency, top cell open circuit voltage, and bottom cell current for bandgaps $E_{g1} = 1.73$ eV and $E_{g2} = 0.94$ eV, for Case (2); no intermediate mirror and a perfect back mirror, assuming optically thin cells and Case (3); an air gap intermediate mirror and a perfect back mirror. . . . .	28

4.1	The bottom surface texture of the absorbing material is computationally optimized. This diagram is a schematic of 1 unit cell; there are periodic boundary conditions along the $yz$ and $xz$ planes. . . . .	34
4.2	We want to increase the absorption, and equivalently, the Poynting vector into the solar cell material by optimizing a periodic surface texture function. . . . .	36
4.3	The question we ask is: at what $x'$ should a small piece of material be added, and at what $x'$ should material be removed to increase my Figure of Merit? . . .	36
4.4	We can derive the change in figure of merit due to adding a piece of material at a particular $x'$ . . . . .	37
4.5	We can express the $\delta E$ and $\delta H$ from the addition of a polarization with Green's functions solutions in Einstein notation. . . . .	38
4.6	The second insight we need is to establish the symmetry in the Green's functions.	38
4.7	The second insight we need is to establish the symmetry in the Green's functions.	39
4.8	With two simulations we can calculate the Shape Derivative. . . . .	40
4.9	Without the adjoint method, we needed $n + 1$ simulations in order to calculate the Shape Derivative. . . . .	41
4.10	(a) The initial absorption enhancement as a function of frequency and (b) a top-down view of the surface texture; the colors show the height of the absorbing material (from the antireflection coating to the bottom dielectric, as seen in Fig. 4.1).	42
4.11	(a) The final absorption enhancement as a function of frequency and (b) a top-down view of the surface texture; the colors show the height of the absorbing material (from the antireflection coating to the bottom dielectric, as seen in Fig. 4.1).	42
4.12	The reciprocal ( $k$ -) space representation for the final texture seen in Fig. 4.11. The blue pie slices represent the phase of the complex exponential Fourier coefficients.	43
4.13	The absorption enhancement for the texture in Fig. 4.11, plotted as a function of frequency at normal incidence (blue) and angle averaged (green). . . . .	43
4.14	The absorption enhancement factor (AE) averaged over frequency and polarization, as a function of incident angle $\theta$ in the $xz$ plane (blue) and the $yz$ plane (red). . . . .	44
4.15	The surface textures and absorption enhancement as a function of frequency for different initial conditions, revealing a broad optimum. . . . .	45
4.16	The absorption enhancement factor (AE) averaged over frequency and polarization, as a function of incident angle $\theta$ in the $xz$ plane (blue) and the $yz$ plane (red). . . . .	46
4.17	The absorption enhancement factor (AE) averaged over frequency and polarization, as a function of incident angle $\theta$ in the $xz$ plane (blue) and the $yz$ plane (red). . . . .	47
4.18	The absorption enhancement factor (AE) averaged over frequency and polarization, as a function of incident angle $\theta$ in the $xz$ plane (blue) and the $yz$ plane (red). . . . .	48
4.19	The photonic bandstructure for the texture in Fig. 4.15(b). . . . .	49

4.20	(a) The initial absorption enhancement as a function of frequency and (b) a top-down view of the surface texture, for a symmetric texture with a slight perturbation along the diagonal. . . . .	50
4.21	(a) The final absorption enhancement as a function of frequency and (b) a top-down view of the surface texture, showing broken mirror symmetry, from almost symmetric initial conditions seen in Fig. 4.20. . . . .	50
4.22	The reciprocal space representation for the texture with broken mirror symmetry in Fig. 4.21. The blue pie slices represent the phase of the complex exponential Fourier coefficients. . . . .	51
4.23	Optimizations were carried out at periodicities from 50 to 800 nm, in increments of 50 nm. For each periodicity, at least 3 optimizations were completed for randomly chosen initial starting noise. The Figure of Merit (absorption enhancement for the worst performing frequency and polarization at normal incidence) is plotted for each optimization. . . . .	51
4.24	The Figure of Merit (minimum absorption enhancement at normal incidence) plotted for 100 randomly generated textures of 710 nm periodicity. For comparison, the Figure of Merit for the optimized texture in Fig. 4.15(b) is shown by the dotted red line. . . . .	52
4.25	The (a) reciprocal k-space diagram and (b) real-space top down view of the median randomly generated texture from Fig. 4.24. . . . .	52
4.26	The absorption enhancement as a function of frequency at normal incidence for the optimized texture from Fig. 4.15(b) (blue) compared with the median random texture from Fig. 4.25 (green). Lines are averaged over the two orthogonal polarizations. . . . .	53
4.27	The absorption enhancement as a function of frequency, angle averaged, for the optimized texture from Fig. 4.15(b) (blue) compared with the median random texture from Fig. 4.25 (green). . . . .	53
4.28	The Figure of Merit (minimum absorption enhancement at normal incidence) plotted for 11 randomly generated textures of 2300 nm periodicity. For comparison, the Figure of Merit for the optimized texture in Fig. 4.15(b) is shown by the dotted red line. . . . .	54
4.29	A top-down view of the surface texture, for the randomly generated texture with periodicity of $2300 \text{ nm} = 10\lambda_n = 3.5$ , with median Figure of Merit (minimum absorption enhancement). . . . .	54
4.30	The absorption enhancement as a function of frequency at normal incidence for the optimized texture from Fig. 4.15(b) (blue) compared with the median random texture with 2300 nm periodicity from Fig. 4.29 (green). Lines are averaged over the two orthogonal polarizations. . . . .	55
4.31	The absorption enhancement as a function of frequency, angle averaged, for the optimized texture from Fig. 4.15(b) (blue) compared with the median random texture with 2300 nm periodicity from Fig. 4.29 (green). . . . .	55
4.32	Setup for texture optimization with a height amplitude constraint. . . . .	56

4.33	Final texture for the optimization with a height amplitude constraint and absorption enhancement for normal incidence light. . . . .	56
4.34	Angle averaged and normal incidence performance for the constrained height texture in Fig. 4.33. . . . .	57
4.35	The absorption enhancement factor (AE) averaged over frequency and polarization, as a function of incident angle $\theta$ in the $xz$ plane (blue) and the $yz$ plane (red) for the texture in Fig. 4.33. . . . .	57
5.1	For high efficiency, below bandgap photons need to be recycled back to the hot source. This is done with either (a) a spectrally selective source, such as a photonic crystal, which exhibits low emissivity of below bandgap photons (low emissivity of photons is analogous to high reflectivity of photons back to the source) or (b) with a mirror on the back of the photovoltaic cells which reflects the infrared photons back to the source. . . . .	60
5.2	Reflectivity of a standard production GaAs solar cell from Alta Devices Inc. (The world record cell had even higher sub-bandgap reflectivity, 98%.) Achieving the same step function response, in an InGaAs alloy, would be ideal for thermophotovoltaics. . . . .	61
5.3	Perspective view of the thermophotovoltaic chamber. . . . .	62
5.4	Cross-sectional view of the thermophotovoltaic chamber. . . . .	63
5.5	The efficiency as a function of photovoltaic cell infrared reflectivity for single junction cells. The source radiation temperature is $1200^{\circ}C$ , the cell temperature is $20^{\circ}C$ , and $\eta_{ext} = 0.3$ . . . . .	66
5.6	The efficiency as a function of photovoltaic cell infrared reflectivity for single junction cells. The source radiation temperature is $1500^{\circ}C$ , the cell temperature is $20^{\circ}C$ , and $\eta_{ext} = 0.3$ . . . . .	67
5.7	The blackbody power spectrum, for blackbody sources at $1500^{\circ}C$ and $1200^{\circ}C$ . For a 0.8eV bandgap cell and a $1200^{\circ}C$ source, the power absorbed by the solar cell is indicated by the blue region, and the power recycled back to the hot source is indicated by the red region. Similarly for a 0.95eV bandgap cell and a $1500^{\circ}C$ source, the regions of recycled power and absorbed photon are highlighted in red and blue, respectively. . . . .	68
5.8	The short circuit current ( $J_{sc}$ ) as a function of bandgap, for blackbody sources at $1500^{\circ}C$ and $1200^{\circ}C$ . For a 0.8 eV bandgap cell and a $1200^{\circ}C$ hot source, 4% of the photons emitted by the blackbody are above bandgap and thus absorbed by the photovoltaic cell, while 96% are recycled back to the hot source, as indicated by the red dashed lines. . . . .	69
5.9	The efficiency as a function of photovoltaic cell infrared reflectivity for dual junction cells. $E_{g1}$ is the bandgap of the top cell in the dual junction stack, and $E_{g2}$ is the bandgap of the bottom cell. The source radiation temperature is $1200^{\circ}C$ , the cell temperature is $20^{\circ}C$ , and for both top and bottom cells, $\eta_{ext} = 0.3$ . . . . .	70

5.10	The efficiency as a function of photovoltaic cell infrared reflectivity for dual junction cells. $E_{g1}$ is the bandgap of the top cell in the dual junction stack, and $E_{g2}$ is the bandgap of the bottom cell. The source radiation temperature is $1500^{\circ}\text{C}$ , the cell temperature is $20^{\circ}\text{C}$ , and for both top and bottom cells, $\eta_{ext} = 0.3$ . . . . .	71
5.11	The thermophotovoltaic efficiency plotted as a function of the hot source sub-bandgap reflectivity and the cold side sub-bandgap reflectivity for a photovoltaic cell with bandgap 0.8 eV and a hot source temperature of $1200^{\circ}\text{C}$ . . . . .	72
5.12	The efficiency of a thermophotovoltaic system assuming 100% back reflectivity and $\eta_{ext} = 100\%$ , as a function of the bandwidth above the bandgap that is transmitted to the cell (blue line) and assuming 99% back reflectivity (red line). . . . .	73
6.1	Efficiency of single bandgap solar cells under maximum concentration. . . . .	75
6.2	Efficiency of dual bandgap solar cells under maximum concentration. . . . .	76
6.3	Efficiency of solar thermophotovoltaics as a function of back mirror sub-bandgap reflectivity. We denote the temperature of the intermediate layer and the bandgap at each point. . . . .	79

# List of Tables

3.1	Efficiency of Best Dual Bandgap Cells . . . . .	26
3.2	Efficiency of Best Multi-Bandgap Cells . . . . .	29
3.3	Efficiency of InGaP (1.8 eV) & GaAs (1.4 eV) Dual Bandgap Cells . . . . .	30
4.1	Absorption enhancement factor ( $AE$ ) results. . . . .	49

## Acknowledgments

I would like to begin by thanking my advisor, Professor Eli Yablonovitch. Prof. Yablonovitch taught me how to find the important scientific problems, and simplify these problems to gain fundamental insights, while always remaining skeptical of results. He also emphasized the importance of clarity in communication, a skill as important as the technical ones. I'd like to thank the my qualifying and thesis committee members, Professors Laura Waller, Ming Wu, Tarek Zohdi, Connie J. Chang-Hasnain, and Xiang Zhang. Their comments and questions helped me greatly clarify my dissertation work.

I have had the fortune to work with some wonderful collaborators. Dr. Owen Miller patiently mentored me in inverse design and the physics of solar cells, and put up with my endless questioning. Dr. Miller was fundamental in the development of the numerical light trapping work, and contributed significantly to the algorithm design and implementation. His doctoral thesis also provided the inspiration for Chapters 2 & 3. I have collaborated from the beginning to the end with Samarth Bhargava, and our many discussions have informed insights into the adjoint method for electromagnetics applications. Collaboration with Professor Laura Waller lead to insights in using the adjoint method in Fourier optics and phase retrieval. My undergraduate researcher, Chi-Sing Ho, contributed to the work on intermediate mirrors for multi-bandgap solar cells. Her initial designs of Bragg stacks ultimately led to the conclusion that an air gap intermediate mirror is necessary to obtain a voltage boost in multi-bandgap cells. My other undergraduate researcher, Joeson Wong, contributed to the implementation of constraints in the numerical light trapping work. The work in Chapter 2 regarding the distinction between the “optically thick” and “optically thin” cases was informed by discussions with Dr. Myles Steiner and Dr. Sarah Kurtz at the National Renewable Energy Laboratory. Finally, I'd like to also acknowledge the members of the “Light-Material Interactions in Energy Conversion” Energy Frontier Research Center led by Professor Harry Atwater at Caltech, and all the students I had fruitful discussions with on solar cells, including Dr. Emily Kosten, Professor Vivian Ferry, and John Lloyd.

I was lucky to have the financial support of the Department of Energy Office of Science Graduate Fellowship and UC Berkeley Chancellor's Fellowship. I was even luckier to have the moral support of my colleagues in the opto groups, my roommates over the years, the trivia team, and my sweet friends. I'd also like to thank my undergraduate research advisor from MIT, Professor Tonio Buonassisi, who taught me to always keep a positive outlook.

My family is pretty incredible. I would like to thank my older brother who helped me not take myself too seriously and boosted my spirits. My mother and father have always been my biggest supporters. They have always cheered me on and encouraged me to never give up. This work would not be possible without them.

# Chapter 1

## Introduction

In 2014, the solar electric capacity of the United States was 17,500 MW [1]. The annual installed capacity is growing exponentially [1], and the oil giant Shell predicts that solar will provide almost 40% of our global energy needs by 2100 [2]. The potential dominance of solar energy means that small improvements to the efficiency of solar photovoltaics can have large ramifications. This thesis explores the fundamental origins of efficiency in solar photovoltaics, and looks at how improvements in the optical design of the photovoltaic cell can lead to improvements in efficiency.

Improvements in efficiency lowers cost; this is because the cost of photovoltaics can be broken down into “module,” “inverter,” and “balance of system” costs. The module cost is the cost of the actual photovoltaic panels, the inverter cost is the cost of the conversion of the direct current (DC) photovoltaic cell output to alternating current (AC), and the balance of system cost is the lumped cost of everything else, including soft costs and wiring to the grid. The inverter and balance of system costs are approximately fixed per module. Even if the module cost is invariant or slightly increased with higher efficiency, higher efficiency will bring the overhead costs down. This argument is further strengthened by the trend of decreasing percentage of total cost taken up by the module cost [3]. To justify device-level solar cell research, it is not enough to aim to just decrease the module cost, the efficiency must be improved as well. In this thesis, we look to both reducing module cost without sacrificing efficiency, as well as improving efficiency.

For highly efficient solar cells, high material quality is necessary. However, this is not the full picture. Optical design considerations, such as the inclusion of a highly reflecting back mirror, is crucial to approaching theoretical thermodynamic efficiencies. At the open-circuit voltage condition of the photovoltaic cell, absorbed photons can be re-emitted as luminescence internal to the cell. To achieve a high voltage, it is important that these photons are extracted from the front surface of the cell. The importance of the back mirror can be seen in the Gallium Arsenide (GaAs) photovoltaic cells created by Alta Devices. Through a process of epitaxial lift-off, Alta Devices was able to create cells a few microns thick, with a highly reflecting mirror on the backside. Without epitaxial lift-off, the GaAs cell would remain on the growth substrate, leading to loss of internally luminescent photons out

of the backside, rather than favorable extraction through the front surface. The Alta Devices GaAs cell reached a record-breaking efficiency of 28.8% [4], a testament to the importance of optical design.

In this thesis, we look to understand the fundamental origins of high efficiency, find ways to practically increase efficiency, and drastically reduce material costs by surface texturing. Chapter 2 focuses on improving efficiency by using reflecting mirrors on the backside of GaAs solar cells. This chapter illustrates how the absorptivity of the material dictates the voltage improvement available by using a back mirror on the solar cell. Chapter 3 extends the idea of a reflecting back mirror to the case of multi-bandgap solar cells, where different bandgap materials are layered from smallest bandgap on the bottom to the largest bandgap on the top. In this case, we need intermediate mirrors between the sub-cells that both reflect and transmit the appropriate photons, and Chapter 3 argues that air gaps serve as the optimal intermediate mirrors for this task. Chapter 4 explores light trapping techniques that would allow a cell on the order of 100 nm to absorb the same amount of light as a cell a few microns thick. This would allow the material cost of the absorbing layer of the solar cell to become negligible, while preserving the efficiency of the cell. Chapter 5 moves away from solar photovoltaics to thermo-photovoltaics. In this chapter, we look at how a local terrestrial heat source can be converted to electricity by a photovoltaic cell. We predict efficiencies of heat to electricity conversion with reasonable assumptions in this chapter, finding that  $> 50\%$  heat to electricity conversion can be achieved in a scalable manner. In Chapter 6, we look at the efficiencies of solar photovoltaic technologies under concentration.

## Chapter 2

# The Voltage Boost Enabled by a Back Mirror

Improvements to the optical design of a solar cell have recently enabled efficiencies close to the Shockley-Queisser limit [5]. For example, in part by increasing the back mirror reflectivity of the solar cell, Alta Devices achieved a record efficiency of 28.8% with a 1-sun, single junction Gallium Arsenide (GaAs) solar cell [4]. In this chapter, we will quantify the voltage difference between a cell with a back mirror and a cell without a back mirror.

### 2.1 Optical Model of the Solar Cell

We begin by introducing the ideal single bandgap solar cell, as described by Shockley and Queisser in 1961 [6], deriving the limiting efficiency following the procedure in [5]. We assume step function absorption (all photons above the bandgap energy are absorbed) and a perfect antireflection coating on the front surface of the solar cell. In this thesis, we will assume infinite carrier mobility and perfect carrier collection in order to keep the focus on the optical design and photon management in the solar cell.

Our analysis begins with a cell in the dark, at thermal equilibrium with the surroundings. The cell absorbs blackbody radiation from the external environment. The blackbody radiation  $b(E)$  can be approximated by the tail of the blackbody formula:

$$b(E) = \frac{2E^2}{h^3c^2} \exp\left(-\frac{E}{k_B T}\right), \quad (2.1)$$

where the units of  $b$  are [photons/(time  $\times$  area  $\times$  energy  $\times$  steradian)].  $E$  is the photon energy,  $h$  is Planck's constant,  $c$  is the speed of light, and  $k_B T$  is the thermal energy.

The photon flux into the front surface of the solar cell due to absorption of the blackbody is given as:

$$L_{bb} = 2\pi \int_0^\infty \int_0^{\frac{\pi}{2}} A(E)b(E) \sin \theta \cos \theta d\theta dE, \quad (2.2)$$

where  $\theta$  is the angle from the normal to the cell, and  $A(E, \theta) = A(E)$  is the step function absorptivity for  $E_g$ . Since the cell is in thermal equilibrium, this expression is also equivalent to the photon flux emitted out of the front surface.

When the sun illuminates the cell, it moves into quasi-equilibrium, with chemical potential  $qV$  (this is equivalent to the separation of the quasi-Fermi levels, where  $q$  is the charge of an electron and  $V$  is the voltage). Under illumination, the photon flux out the front of the cell,  $L_{ext}$ , is given by:

$$L_{ext}(V) = \exp\left(\frac{qV}{kT}\right) L_{bb} = \exp\left(\frac{qV}{kT}\right) 2\pi \int_{E_g}^\infty \int_0^{\frac{\pi}{2}} b(E) \sin \theta \cos \theta d\theta dE. \quad (2.3)$$

The external luminescence yield,  $\eta_{ext}$ , is defined as the ratio of the rate of radiative flux out the top,  $L_{ext}$ , to the total emission rate of photons  $L_{ext} + L_{other}$ , where  $L_{other}$  is the sum of the radiative flux out of the bottom of the cell and non-radiative recombination within the cell:

$$\eta_{ext} = \frac{L_{ext}}{L_{ext} + L_{other}}. \quad (2.4)$$

The absorption of photons from the sun is  $\int a(E)S(E)dE$ , where  $S$  is the number of photons in the solar spectrum per unit area per unit time. The current of the solar cell is given by the absorption of photons from the sun minus the emission of photons out of the cell. From Eqn. 2.4, we get  $L_{ext} + L_{other} = \frac{L_{ext}}{\eta_{ext}}$ . Thus the  $J - V$  characteristic of the solar cell is given by:

$$J = \int_{E_g}^\infty S(E)dE - L_{ext} - L_{other} = \int_{E_g}^\infty S(E)dE - \frac{1}{\eta_{ext}} \pi \exp\left(\frac{qV}{kT}\right) \int_{E_g}^\infty b(E)dE, \quad (2.5)$$

where  $J$  is the current density and  $V$  is the voltage of the top cell.

If we assume a perfectly reflecting back mirror, and no non-radiative recombination, we have  $\eta_{ext} = 1$ . We plot the  $J - V$  characteristic of this ideal case in in Fig. 2.1. We want to operate at the point of maximum power output on this graph. Multiplying Eqn. (2.5) by  $V$  yields the power density - current characteristic, which is plotted in Fig. 2.1. We want the maximum power output from our solar cell, so we operate it at the voltage corresponding to the maximum power point (MPP) on the power density-current curve.

## 2.2 Open-Circuit Voltage, $V_{oc}$

The expression for the open circuit voltage is given by setting  $J = 0$  in Eqn. 2.5:

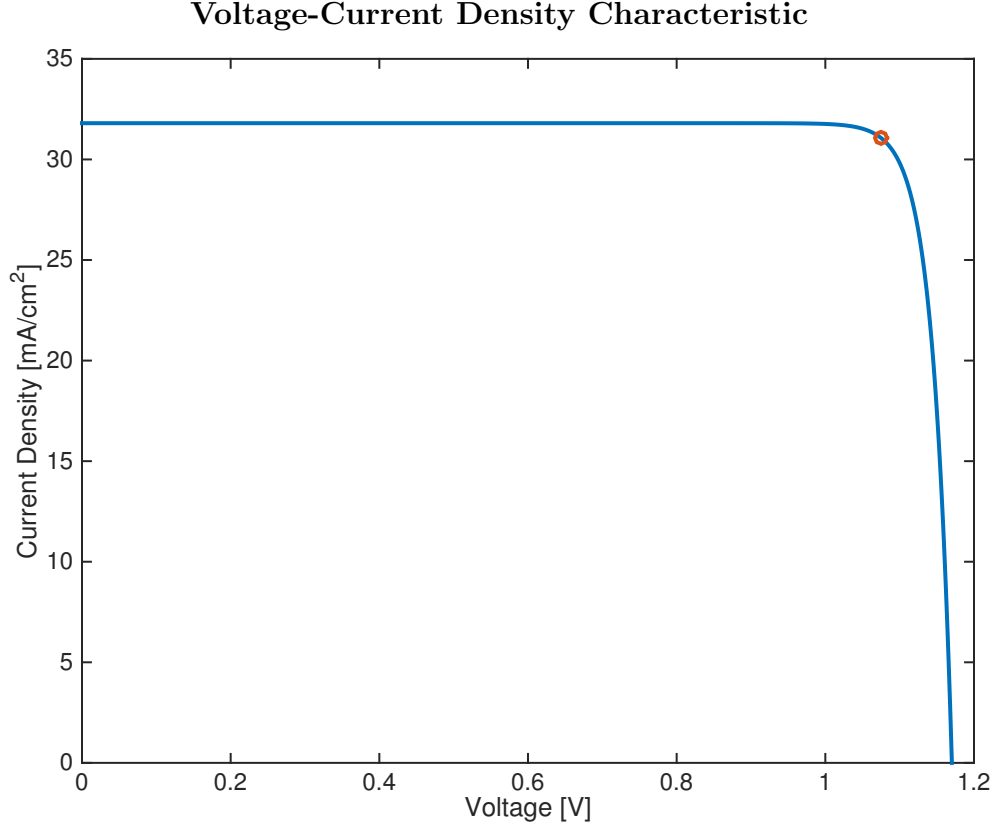


Figure 2.1: The  $J - V$  characteristic for an ideal solar cell with bandgap  $E_g = 1.43$  eV. The maximum power point (MPP) is indicated in red. The open-circuit voltage is the  $x$ -intercept, and the short-circuit current density is the  $y$ -intercept. The efficiency at the MPP is 33.4%.

$$V_{oc} = \frac{kT}{q} \ln \left( \frac{\int_{E_g}^{\infty} S(E) dE}{\pi \int_{E_g}^{\infty} b(E) dE} \right) - \frac{kT}{q} \ln \left( \frac{1}{\eta_{ext}} \right). \quad (2.6)$$

The open circuit voltage,  $V_{oc}$ , can be expressed as [5], [7]:

$$V_{oc} = V_{oc, ideal} - \frac{kT}{q} \ln \left( \frac{1}{\eta_{ext}} \right). \quad (2.7)$$

From Eqn. 2.7, we see that the open circuit voltage penalty from ideal when  $\eta_{ext} < 1$ , is  $\frac{kT}{q} \ln \left( \frac{1}{\eta_{ext}} \right)$ .

Conventionally, III-V solar cells, such as GaAs, are grown lattice-matched on substrate, resulting in a high quality film of material on a lossy substrate (as the substrate is generally of poor quality). At open-circuit voltage, in such a cell, we have the situation as illustrated in Fig. 2.2. In the case of a solar cell with high radiative recombination, at open-circuit voltage, incident photons are absorbed and radiatively re-emitted internally. These photons

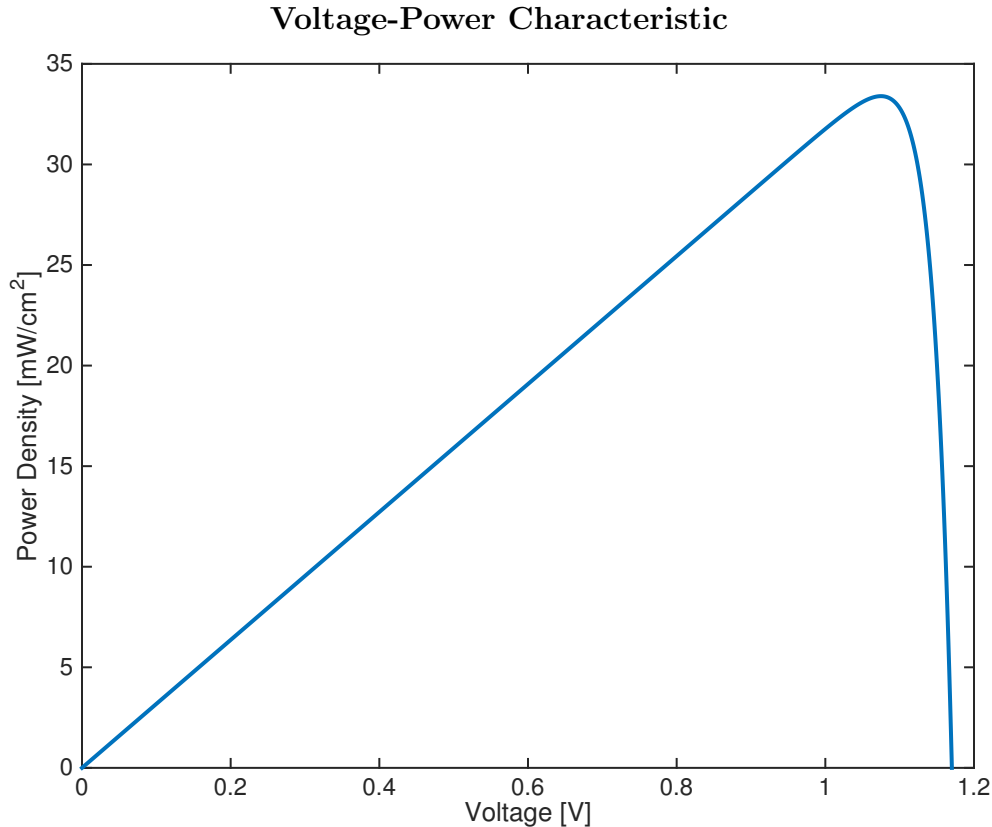


Figure 2.2: The relationship between power and voltage. We use a maximum power point tracker (MPPT) to continually operate the cell at the maximum power point voltage.

can be re-absorbed multiple times before escaping out of the solar cell through either the front or back surface. For this case, we can find  $\eta_{ext}$  from Eqn. (2.4). In Eqn. (2.4),  $L_{other}$  is the rate of emission into the back substrate. The substrate is index-matched to the cell, so due to the large index mismatch of the air and the semiconductor at the top surface,  $L_{other} \gg L_{ext}$ .

We can understand that emission out of the back surface is a loss process by realizing that photon emission out of the front surface is required by detailed balance, but emission out of the back is not [5], [6], [8]. We do not absorb through the back surface, so we don't want to emit out of that surface.

However, with epitaxially lifted off solar cells [9], [10], where the thin GaAs film is lifted off from the substrate and a back mirror is applied, we see a much different picture, as illustrated in Fig. 2.2. In the ideal case, where we have a perfect back reflector and no non-radiative recombination, at open circuit voltage, we have  $\eta_{ext} = 1$  and all absorbed photons are eventually re-emitted out of the front surface of the cell [5], [11], [12]. This situation, in contrast to the one in Fig. 2.2, will result in the ideal characteristic illustrated in Fig. 2.1 with  $\eta_{ext} = 1$ .

## Cell Without Back Mirror

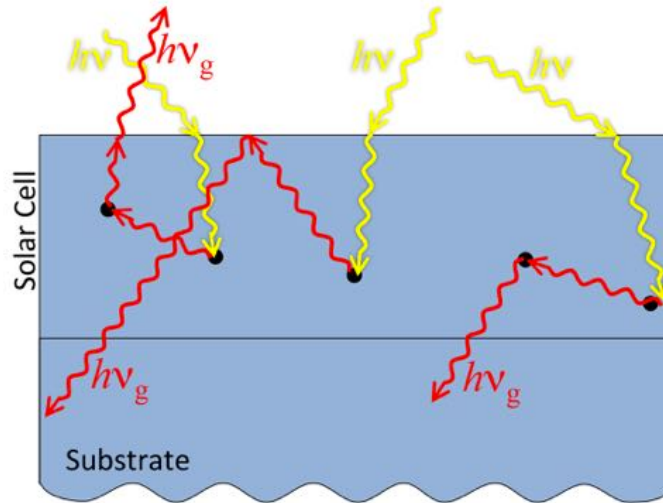


Figure 2.3: Diagram of a solar cell at open circuit voltage with semiconductor index of refraction  $n_s = 3.5$  on an index-matched substrate (analogous to the case of a GaAs cell on a GaAs substrate). Incident photons (shown in yellow) refract towards the normal inside the semiconductor, due to the index mismatch. These incident photons are absorbed and then re-emitted (the re-emitted photons have energies close to the bandgap, and are drawn in red to show the downshift in energy). Most of these internally luminescent photons escape from the bottom surface into the index-matched substrate, as the probability being in the escape cone of the semiconductor/air interface is low.

## Cell With Back Mirror

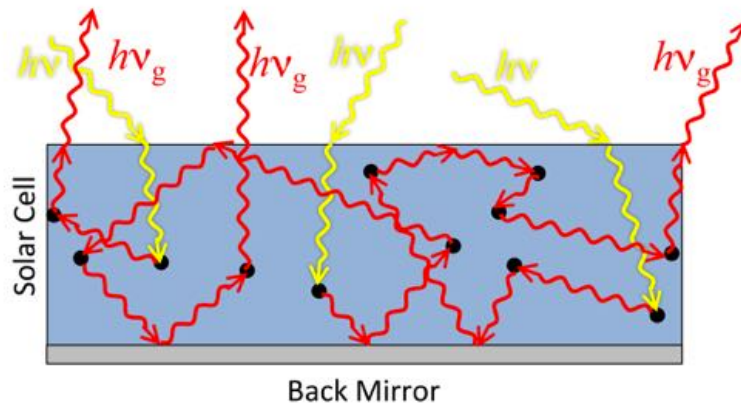


Figure 2.4: Diagram of the case of a solar cell on a perfectly reflecting back mirror; in this case, at open circuit, all the incident photons are absorbed and eventually emitted out of the front surface.

## 2.3 Voltage Penalty for No Back Mirror, $\Delta V_{nm}$

In the case of a solar cell of ideal material with only radiative recombination, but with no back mirror, we will have  $\eta_{ext} < 1$ , and we denote the open circuit voltage penalty for this case as  $\Delta V_{nm} = V_{oc, \text{ no mirror}} - V_{oc, \text{ ideal}}$ .

We first derive the upper and lower bounds of  $\eta_{ext}$ , in the limits of weak and strong absorption of the internal luminescence. We then generalize to find  $\eta_{ext}$  for an arbitrary absorption spectrum. In our derivations, we make the assumption of no non-radiative recombination and a perfect antireflection coating on the cell, as well as an index matched substrate below.

### Lower Bound for $\eta_{ext}$

We take a look at the limiting case where the cell is optically thin (i.e. weakly absorbing) to the internally luminescent photon energies. For this limit, we can recognize that the probability of front surface escape, relative to substrate absorption, is the fraction of solid angle that is subtended by the escape cone [13]. We can derive  $\eta_{ext}$  for Case (1a) as follows [14]:

$$\eta_{ext} = \frac{2\pi \int_0^{\sin^{-1}(\frac{1}{n_s})} \sin \theta d\theta}{2\pi \int_0^\pi \sin \theta d\theta} = \frac{1}{2} \left( 1 - \sqrt{1 - \frac{1}{n_s^2}} \right) \approx \frac{1}{4n_s^2}. \quad (2.8)$$

### Upper Bound for $\eta_{ext}$

We now look at the limiting case of a material that is very strongly absorbing of the internal luminescence.

The external luminescence yield,  $\eta_{ext}$ , can be equivalently defined as the ratio of radiative emission out the front of the cell, to total loss rate of photons out of the cell [5]. We have:

$$\eta_{ext} = \frac{L_{ext}}{L_{ext} + L_{int\downarrow}}, \quad (2.9)$$

where  $L_{ext}$  is the radiative emission rate out of the front of the cell, and  $L_{int\downarrow}$  is the emission rate out of the back of the cell.

At the top surface, since we assume a perfect antireflection coating, we can assume perfect transmittance of internally luminescent photons in the escape cone  $\theta_s$  (given by Snell's law,  $n_s \sin \theta_s = 1$ ). There is total internal reflection for internal luminescent photons outside the escape cone. Due to the many absorption events inside the material (strong absorber assumption), the internal photons hitting the top surface have a Lambertian distribution. The angle-averaged transmittance of the internally luminescent photons through the top surface,  $T_{int\uparrow}$ , is thus given by [14]:

$$T_{int\uparrow} = \frac{2\pi \int_0^{\sin^{-1}(\frac{1}{n_s})} \sin \theta \cos \theta d\theta}{2\pi \int_0^{\frac{\pi}{2}} \sin \theta \cos \theta d\theta} = \frac{1}{n_s^2}, \quad (2.10)$$

where the  $\cos \theta$  term accounts for the Lambertian distribution.

Since the cell is free of non-radiative recombination, the only other photon flux out of the cell is out the rear surface, which is described by rear luminescent transmittance  $T_{int\downarrow}$ .  $T_{int\downarrow}$  is unity because the top cell is index-matched to the substrate below. Applying (2.9) and (2.10) yields:

$$\eta_{ext} = \frac{T_{int\uparrow}}{T_{int\uparrow} + T_{int\downarrow}} = \frac{1}{1 + n_s^2} \quad (2.11)$$

Thus, in the case when the cell is a very strong re-absorber of the internal luminescence,  $\eta_{ext}$  is a factor of 4 higher than when the cell is a very weak re-absorber of internal luminescence. For a semiconductor index of refraction of  $n_s = 3.5$ , such as in GaAs,  $\eta_{ext} \approx 8\%$  in the limit of a cell that is optically thick to the internal luminescence and  $\eta_{ext} \approx 2\%$  in the limit of an optically thin cell. The corresponding open circuit penalties for having no back mirror are  $\Delta V_{nm} \approx -60mV$  and  $\Delta V_{nm} \approx -100mV$ , respectively.

The question arises, in the case of a real material, which factor of 4 is applicable? The answer to this question will let us quantify how much voltage boost is possible when an absorbing substrate is replaced with a back mirror. In order to reconcile this factor of 4, we derive  $\eta_{ext}$  as a function of GaAs absorption coefficient and thickness.

## Real Absorption Spectrum, $\eta_{ext}$

To find  $\eta_{ext}$  and  $\Delta V_{nm}$  with the absorption spectrum of GaAs, we again follow the analysis in [5]. In the dark, under no illumination, blackbody radiation is absorbed by the cell through the front surface. The blackbody radiation absorbed through the front  $b_{\downarrow}(E)$  is:

$$b_{\downarrow}(E) = \frac{2E^2}{c^2 h^3 \left( \exp\left(\frac{E}{k_B T}\right) - 1 \right)} A(E) \approx \frac{2E^2}{c^2 h^3} \left( \exp\left(-\frac{E}{k_B T}\right) \right) A(E), \quad (2.12)$$

where the blackbody spectrum  $b_{\downarrow}(E)$  is in units of photons/area/time/energy,  $A(E)$  is the absorptivity,  $E$  is the photon energy,  $c$  is the speed of light,  $h$  is Planck's constant,  $k_B$  is the Boltzmann constant, and  $T$  is the solar cell temperature.

The photons incident on the front surface show a Lambertian distribution. Upon entering the higher index semiconductor, they refract towards the normal. The absorptivity  $A(E)$  is thus averaged over all incident angles:

$$A(E) = 2\pi \int_0^{\frac{\pi}{2}} \left( 1 - \exp\left(-\frac{\alpha(E)L}{\cos \theta_2}\right) \right) \sin \theta \cos \theta d\theta \approx 2\pi (1 - \exp(-\alpha(E)L)) \int_0^{\frac{\pi}{2}} \sin \theta \cos \theta d\theta, \quad (2.13)$$

where  $\theta$  is the incident angle,  $\theta_2 = \sin^{-1} \frac{\sin \theta}{n_s}$ , is the angle inside the semiconductor,  $\alpha(E)$  is the absorption coefficient as a function of photon energy, and  $L$  is the cell thickness. Since there is a large refractive index mismatch between air and the semiconductor, we can approximate  $\cos \theta_2 \approx 1$ .

In the dark, in thermal equilibrium, the emission from the front of the cell equals the absorption through the front. Under a potential  $V$ , the emission  $L_{ext}(E)$  takes the form:

$$L_{ext}(E) = \frac{2E^2}{c^2 h^3 \left( \exp \left( \frac{E - qV}{k_B T} \right) - 1 \right)} A(E) \approx \frac{2E^2}{c^2 h^3} \exp \left( \frac{-E}{k_B T} \right) \exp \left( \frac{qV}{k_B T} \right) A(E), \quad (2.14)$$

where  $q$  is the charge of an electron.

The blackbody radiation absorbed from the back surface takes the form:

$$b_{\uparrow}(E) = \frac{2n_s^2 E^2}{c^2 h^3 \left( \exp \left( \frac{E}{k_B T} \right) - 1 \right)} A_{back}(E) \approx \frac{2n_s^2 E^2}{c^2 h^3} \exp \left( -\frac{E}{k_B T} \right) A_{back}(E), \quad (2.15)$$

where  $A_{back}(E)$  is the absorptivity of the incident photons on the back surface. The factor of  $n_s^2$  accounts for the increased density of states in the index-matched substrate. If an incident photon from the back is within the escape cone, it sees a single pass through the cell. If it is outside the escape cone, it sees a double pass, due to total internal reflection. Thus, we have:

$$A_{back}(E) = 2\pi \int_0^{\frac{\pi}{2}} \left( 1 - \exp \left( -\frac{f(\theta)\alpha(E)L}{\cos \theta} \right) \right) \sin \theta \cos \theta d\theta dE, \quad (2.16)$$

where  $f(\theta)$  is given as:

$$f(\theta) = \begin{cases} 1, & \text{if } \theta < \theta_c \\ 2, & \text{otherwise} \end{cases} \quad (2.17)$$

where the critical angle  $\theta_c$  is given by Snell's law as  $\theta_c = \sin^{-1} \frac{1}{n_s}$ .

Again, the absorption through the back of the cell is equivalent to the emission out the back of the cell in thermal equilibrium. Under a potential  $V$ , the emission out the back,  $L_{int\downarrow}(E)$  is given as follows:

$$L_{int\downarrow}(E) = \frac{2n_s^2 E^2}{c^2 h^3 \left( \exp \left( \frac{E - qV}{k_B T} \right) - 1 \right)} A_{back}(E) \approx \frac{2n_s^2 E^2}{c^2 h^3} \exp \left( -\frac{E}{k_B T} \right) \exp \left( \frac{qV}{k_B T} \right) A_{back}(E). \quad (2.18)$$

(Equation 12)

Applying Eqn. (2.9), we get the external luminescence yield  $\eta_{ext}$ :

$$\begin{aligned}
\eta_{ext} &= \frac{\int_0^\infty L_{ext}(E)dE}{\int_0^\infty L_{ext}(E)dE + \int_0^\infty L_{int\downarrow}(E)dE} \\
&= \frac{\int_0^\infty \frac{2E^2}{c^2h^3} \exp\left(-\frac{E}{k_B T}\right) A(E)dE}{\int_0^\infty \frac{2E^2}{c^2h^3} \exp\left(-\frac{E}{k_B T}\right) A(E)dE + \int_0^\infty \frac{2n_s^2 E^2}{c^2h^3} \exp\left(-\frac{E}{k_B T}\right) A_{back}(E)dE}.
\end{aligned} \tag{2.19}$$

The external luminescence yield derived here from detailed balancing can also be derived with geometrical ray tracing as in [15].

The total internal radiation  $R_{int}(E)$ , in units of photons/area/time/energy can be given as:

$$R_{int}(E) = \frac{8\pi n_s^2 E^2}{c^2 h^3 \left( \exp\left(\frac{E-qV}{k_B T}\right) - 1 \right)} \alpha(E)L \approx \frac{8\pi n_s^2 E^2}{c^2 h^3} \exp\left(-\frac{E}{k_B T}\right) \exp\left(\frac{qV}{k_B T}\right) \alpha(E)L. \tag{2.20}$$

Photons that are not emitted out of the front surface or the back surface of the solar cell must be reabsorbed. We can thus write the reabsorbed radiation  $R_{abs}(E)$ , in units of photons/area/time/energy as:

$$R_{abs}(E) = R_{int}(E) - L_{int\downarrow}(E) - L_{ext}(E). \tag{2.21}$$

The probability that a luminescent photon is reabsorbed,  $P_{abs}$ , is thus given as:

$$P_{abs} = \frac{\int_0^\infty R_{abs}(E)dE}{\int_0^\infty R_{int}(E)dE}. \tag{2.22}$$

After an incident photon is absorbed and re-emitted radiatively, there are 3 options:

1. internal re-absorption,
2. emission out the back surface, or
3. emission out the front surface.

Figs. 2.3 and 2.3 show the fate of internal photons, as a function of photon energy. This graph is modeled after the breakdown of internal photons in the silicon solar cell, as in [16]. The total internal emission spectrum (2.20) is normalized to an area of unity, and the spectrum of reabsorbed photons (2.21), emission out the back surface (2.18), and emission out the front surface (2.14) are also normalized by the same factor. Fig. 2.3 shows the spectrum of internal luminescence for a 1  $\mu\text{m}$  thick GaAs cell, and Fig. 2.3 concerns a 100 nm GaAs cell. In Figs. 2.3 and 2.3 and following figures, we assume the temperature of the cell  $T = 20^\circ\text{C}$ .

For the absorption coefficient of GaAs,  $\alpha(E)$ , we use the fit by [5] to the data in [17], with one modification. The fit in [5] ignores the exciton bump at the band-edge, here, we

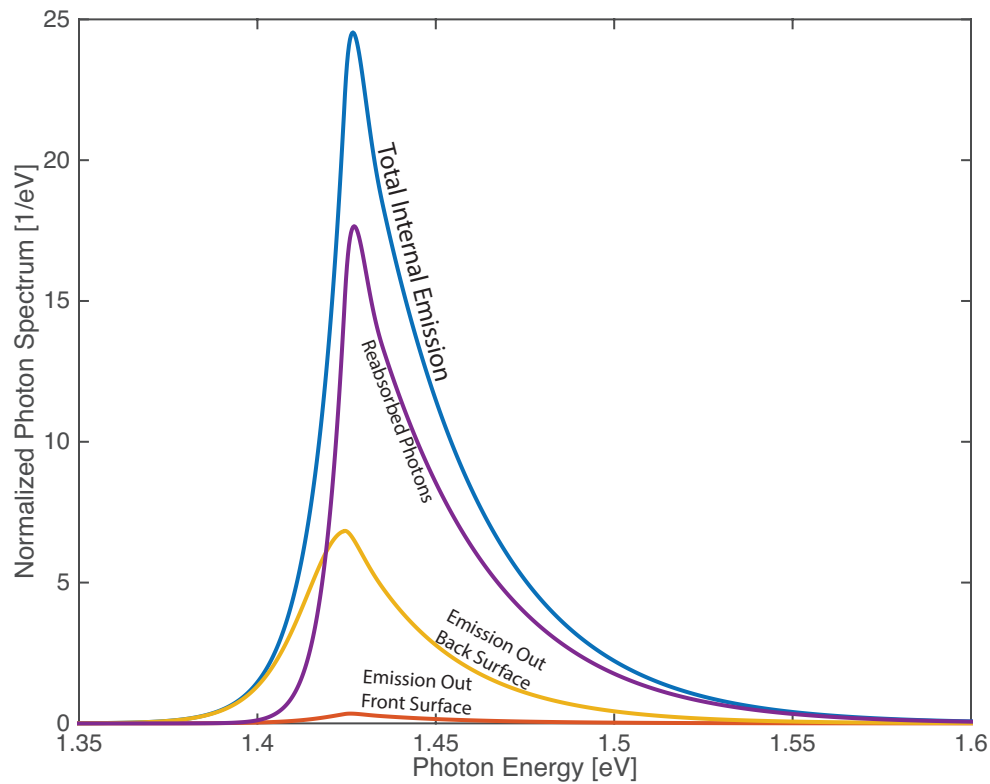
**Fate of Internal Luminescence: 1  $\mu\text{m}$  Thick GaAs Cell on Substrate**

Figure 2.5: The breakdown of internal photons in a GaAs cell, grown on a substrate for a 1  $\mu\text{m}$  thick cell. The spectrum is shown for total internal emission, normalized to unity (blue). Of the total internal spectrum, the fraction of photons reabsorbed by the cell (purple), photons escaping out the front surface (red), and photons emitted in the substrate (yellow), are shown.

## Fate of Internal Luminescence: 100 nm Thick GaAs Cell on Substrate

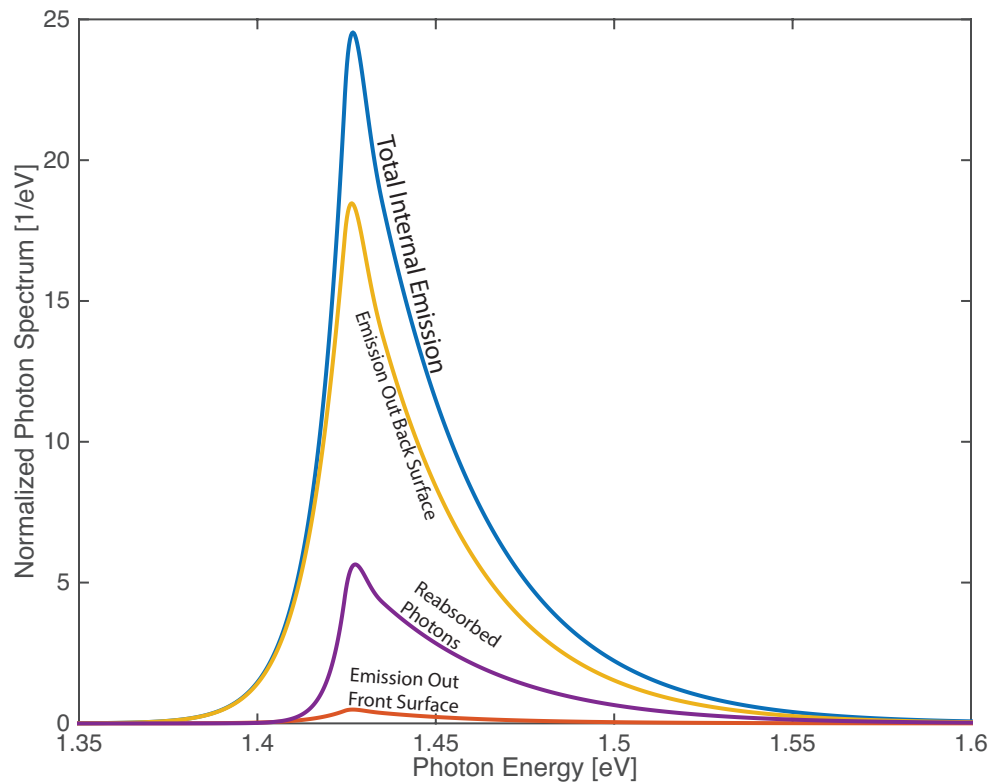


Figure 2.6: The breakdown of internal photons in a GaAs cell, grown on a substrate for a 100 nm thick cell. The spectrum is shown for total internal emission, normalized to unity (blue). Of the total internal spectrum, the fraction of photons reabsorbed by the cell (purple), photons escaping out the front surface (red), and photons emitted in the substrate (yellow), are shown.

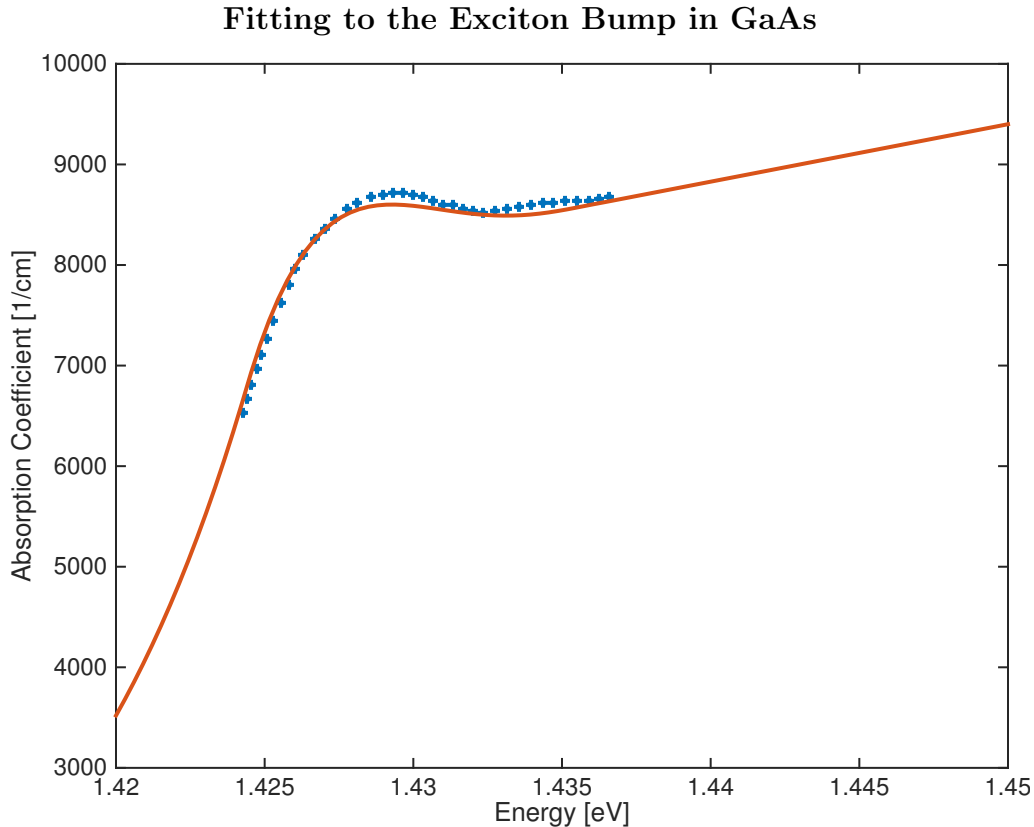


Figure 2.7: The absorption coefficient as a function of photon energy, around the bandedge of GaAs. The blue crosses represent the data from [17], showing a bump around the bandedge due to absorption at the exciton energy. The absorption coefficient fit described in [5] ignores this exciton bump. We use the fit in [5], except at the bandedge, where we model the exciton bump with a fourth degree polynomial. The red line shows our fit.

model this bump with a fourth degree polynomial curve fit to the measured data in [17]; see Fig. 2.3.

In Fig. 2.3, we show the spectrum and breakdown of internal photons in a 1  $\mu\text{m}$  thick cell. The majority of internal photons are reabsorbed, a small amount is emitted out of the back surface into the index-matched substrate, and an even smaller amount escapes out of the front surface. On the other hand, in Fig. reffate100, in the thinner 100 nm cell, the majority of photons are emitted out of the back surface and a small amount is reabsorbed (again, a tiny portion of photons escape out of the front surface of the cell). A thicker cell is more likely to re-absorb internal photons before they can escape. The external luminescence yield  $\eta_{ext}$  is the ratio of the emission out the front surface to the total emission out of the front and back surfaces. From the spectra in Figs. 2.3 and 2.3, we can see that  $\eta_{ext}$  will be greater for the thicker 1  $\mu\text{m}$  cell. The intuition for this is as follows: each re-absorption event randomizes the angular direction of the internal photon. More re-absorption events

allow the internal photon more chances to be in the escape cone, and thus be re-emitted out of the front surface. Thus, in the thicker cell will have a higher  $\eta_{ext}$ .

In Fig. 2.3, we plot the voltage penalty  $\Delta V_{nm}$  for a GaAs cell on an index-matched substrate, as a function of the re-absorption probability  $P_{abs}$  (each value of  $P_{abs}$  corresponds to a certain GaAs cell thickness  $L$  which is also denoted on the graph). We see from Fig. 2.3 that for a 1  $\mu\text{m}$  cell on substrate,  $\Delta V_{nm} = -78\text{mV}$ , and for a 100 nm cell on substrate,  $\Delta V_{nm} = -93\text{mV}$ . In the limit of a cell that is optically thin to the internal luminescence ( $P_{abs} \rightarrow 0$ ), we see that  $\Delta V_{nm} = -98\text{mV}$  in Fig. 2.3, which is consistent with Eqn. (2.7) and Eqn. (2.8). In the limit of a cell that is optically thick to the internal luminescence ( $P_{abs} \rightarrow 1$ ), we see that  $\Delta V_{nm} = -66\text{mV}$ , which is consistent with Eqn. (2.7) and Eqn. (2.11). To reach the limit of a cell that is optically thick to the internal luminescence ( $P_{abs} \rightarrow 1$ ), we must have a cell that is infinitely thick.

In Fig. 2.3, we plot horizontal reference lines for  $\Delta V_{nm} = 0$ , the case of a perfect back reflector, and  $\Delta V_{nm} = -13.2\text{mV}$ , the case of an air interface ( $n = 1$ ) at the back of the cell. To find  $\Delta V_{nm}$  for the case of a semiconductor/air interface at the back surface, we use Eqn. (2.19), modifying  $A_{back}(E)$  to:

$$A_{back, \text{air}}(E) = 2\pi(1 - \exp(-\alpha(E)L)) \int_0^{\frac{\pi}{2}} (1 - R(\theta)) \sin \theta \cos \theta d\theta, \quad (2.23)$$

where  $R(\theta)$  is the reflectivity at the air/semiconductor interface. The Lambertian angle averaged transmissivity  $\int_0^{\frac{\pi}{2}} (1 - R(\theta)) \sin \theta \cos \theta d\theta = 68\%$ . Thus  $\Delta V_{nm} = -13.2\text{mV}$  by Eqn. (2.19) and Eqn. (2.7). It should be noted that though the front surface is also an interface to air, we assume an antireflection coating on the front, so  $A_{back, \text{air}}(E) \neq A(E)$ .

For a high efficiency solar cell, very high absorption of the above bandgap photons is required for high short circuit current. Paradoxically, even though we may have almost step function absorption of incident photons, the cell is not necessarily strongly absorbing of the internal luminescence. We can resolve this paradox by realizing that the internal luminescence is downshifted in energy from the incident photons. Due to the Urbach tail in the absorption spectra of many materials [18], a portion of this internal luminescence is even below the bandedge, where we see very weak absorption. Consequently, it is reasonable to assume both step function absorption and very weak re-absorption of internal luminescence, as we will do in Chapter 3.

Current GaAs cells are a few microns thick [15], and it may seem unrealistic to consider very thin cells in Fig. 2.3, such as cells that are only 100 nm thick, as the current should be low due to poor absorption of incident photons. However, due to advanced surface texturing to enable light trapping as we will see in Chapter 4, they can be capable of absorbing as much as planar 1  $\mu\text{m}$  thin films. A textured 100 nm cell would be optically thick to the incident photons, but optically thin to the internal luminescence.

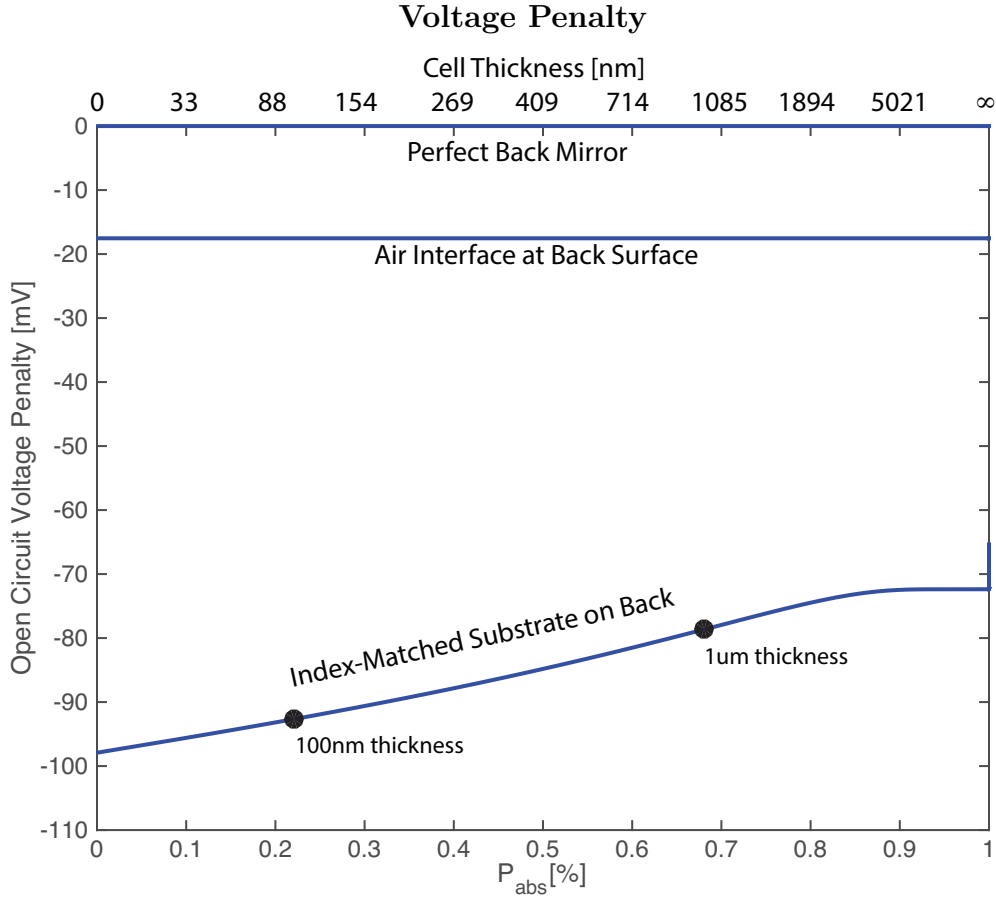


Figure 2.8: The voltage penalty  $\Delta V_{nm}$  for a GaAs cell on an index-matched substrate, as a function of the re-absorption probability  $P_{abs}$ , as given by Eqns. (2.7), (2.19), and (2.22). Each value of  $P_{abs}$  corresponds to a certain cell thickness  $L$ , which is denoted on the top  $x$ -axis of the graph. Horizontal lines indicate where  $\Delta V_{nm} = 0$ , for the case of a perfect back reflector, and where  $\Delta V_{nm} = -13.2mV$ , for the case of an air interface ( $n = 1$ ) at the back of the cell. For a 1  $\mu m$  cell on substrate,  $\Delta V_{nm} = -78mV$ , and for a 100 nm cell on substrate,  $\Delta V_{nm} = -93mV$ . In the limit of a cell that is optically thin to the internal luminescence ( $P_{abs} \rightarrow 0$ ),  $\Delta V_{nm} = -98mV$ , consistent with our derived lower bound for  $\eta_{ext}$ . In the limit of a cell that is optically thick to the internal luminescence ( $P_{abs} \rightarrow 1$ ), we see that  $\Delta V_{nm} = -66mV$ , consistent with our derived upper bound for  $\eta_{ext}$ .

## 2.4 Chapter Summary

The analysis in this chapter has allowed us to see what voltage benefit we will have when replacing an index-matched back substrate with a back mirror. For a real material absorption spectrum, such as GaAs, it is unrealistic to use the strong absorption limit of  $\eta_{ext} \approx \frac{1}{n_s^2}$ , as coming close to this limit requires a GaAs cell of infinite thickness. This is due to the Urbach tail at the bandedge, which means that a portion of the internal luminescence will have energy below the bandedge, where GaAs is very weakly absorbing. For a 100 nm GaAs cell, we are close to the optically thin limit for the internal luminescence, with  $\Delta V_{nm} = -93mV$ . This means that when we replace a back substrate with a back mirror, it is possible to pick up 93mV in open circuit voltage in the 100 nm thick cell. For thicker cells, the voltage penalty decreases, with a 1 um thick cell having  $\Delta V_{nm} = -78mV$ . The back mirror has already played an important role in achieving the current record single junction efficiency [5], and will become even more important in the future, as thinner cells with light trapping textures are produced, which we will discuss further in Chapter 4.

## Chapter 3

# Air Gaps as Intermediate Selective Reflectors for Multi-Bandgap Cells

We have established that to create a highly efficient single bandgap solar cell, we need a highly reflective back mirror. Efficient external luminescence is a pre-requisite for high voltage in a solar cell. A good back reflector provides multiple opportunities for a luminescent photon to escape out of the front surface of the cell, and was instrumental in achieving the record single bandgap solar cell efficiency [5].

However, to increase efficiency further, a logical step is towards multi-bandgap cells. In a multi-bandgap solar cell, bandgaps of different materials are placed in a stack, from largest bandgap on top to smallest on the bottom (see Fig. 3). The top cell absorbs all the photons above its bandgap, and the lower energy photons are transmitted to the next bandgap. It is simple to place a back mirror underneath the bottom-most cell in the stack, as shown in Fig. 3, and obtain a voltage boost in the bottom-most cell. In the past year, a new record of 31.1% was set by the National Renewable Energy Laboratory, for a dual bandgap solar cell under 1 sun illumination, by improving voltage in the bottom cell with a back mirror[19]. However, the question arises, how can we get that same voltage boost in the other sub-cells of the stack?

Intermediate mirrors in a multi-bandgap solar cell can enhance the voltage for each cell in the stack. These intermediate mirrors need to have the added function of transmitting the below bandgap photons to the next cell in the stack. A practical implementation of an intermediate selective reflector is an air gap sandwiched by antireflection coatings. The air gap provides perfect reflection for angles outside the escape cone, and the antireflection coating transmits angles inside the escape cone. As the incoming sunlight is within the escape cone, it is transmitted on to the next cell, while most of the internally trapped luminescence is reflected. In this chapter, we calculate that air gap intermediate reflectors, along with a back mirror, can provide an absolute efficiency increase of  $\approx 5\%$  in multi-bandgap cells.

## Multi-Bandgap Solar Cell

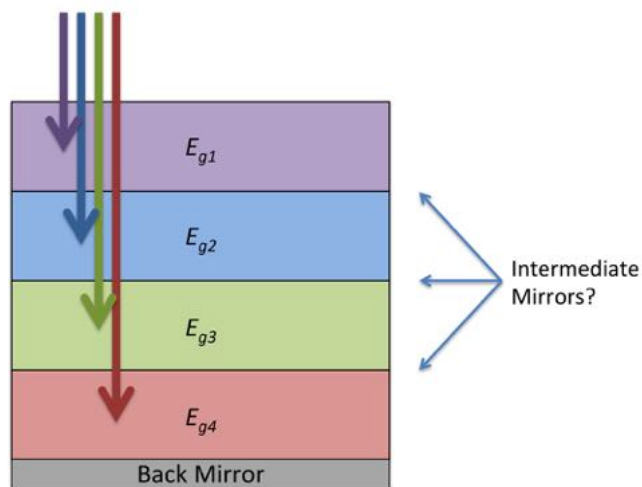


Figure 3.1: Bandgaps of different materials are placed in a stack, from largest bandgap on top to smallest on the bottom in a multi-bandgap cell. The question arises, how do we design intermediate mirrors that reflect internally luminescent photons without impeding the transmission of externally incident photons?

### 3.1 Theory

The quasi-equilibrium derivation given by Shockley and Queisser [6] yields the limiting efficiency of a solar cell with one material bandgap. Refs. [20]–[25] extend the analysis to multiple bandgaps, obtaining the limiting efficiencies with multiple material bandgaps. Of these, [20], [21], [24] analyze the case where the cells are electrically connected in series, so each cell must operate at the same current. Nonetheless, in our following theoretical analysis of the multi-bandgap cell, we assume that each cell is electrically independent (i.e. each cell has two terminal connections), in order to find limiting efficiencies. Refs. [22], [24], [25] look at the case where there are no intermediate mirrors and all the cells are index matched. Multi-bandgap cells with intermediate reflectors were analyzed in [20], [22], but the effect of improved luminescence extraction in boosting the voltage was not accounted for. Here, we account for the voltage boost that arises from improved external extraction from each bandgap of a tandem cell.

We derive the limiting efficiency of multi-bandgap cells following a similar procedure to the derivation for single bandgap cells in [5]. We assume step function absorption (all photons above the bandgap energy are absorbed, and all photons below the bandgap energy are transmitted).

We will first consider the top cell, which consists of the material with the largest bandgap,  $E_{g1}$ . The analysis of this top cell is similar to the single bandgap case derived in [5], also

summarized in Chapter 2. We re-iterate the main points of the derivation to illustrate the differences in analysis of the sub-cells underneath the top cell.

The analysis begins in the dark, at thermal equilibrium, with the cell absorbing blackbody radiation from the external environment. The blackbody radiation  $b(E)$  can be approximated by the tail of the blackbody formula:

$$b(E) = \frac{2E^2}{h^3c^2} \exp\left(-\frac{E}{kT}\right), \quad (3.1)$$

where the units of  $b$  are [photons/(time  $\times$  area  $\times$  energy  $\times$  steradian)].  $E$  is the photon energy,  $h$  is Planck's constant,  $c$  is the speed of light, and  $kT$  is the thermal energy. The photon flux through the front surface of the solar cell due to absorption of the blackbody is given as:

$$L_{bb} = 2\pi \int_0^{infy} \int_0^{\frac{\pi}{2}} A(E, \theta) b(E) \sin \theta \cos \theta d\theta dE, \quad (3.2)$$

where  $\theta$  is the angle from the normal to the cell, and  $A(E, \theta) = A(E)$  is the step function absorptivity for  $E_{g1}$ . Since the cell is in thermal equilibrium, this expression is also equivalent to the photon flux emitted out of the front surface. When the sun illuminates the cell, it moves into quasi-equilibrium, with chemical potential  $qV$  (this is equivalent to the separation of the quasi-Fermi levels, where  $q$  is the charge of an electron and  $V$  is the voltage). Under illumination, the photon flux out the front of the cell,  $L_{ext}$ , is given by:

$$L_{ext}(V) = \exp\left(\frac{qV}{kT}\right) \times L_{bb} = \exp\left(\frac{qV}{kT}\right) 2\pi \int_{E_{g1}}^{\infty} \int_0^{\frac{\pi}{2}} b(E) \sin \theta \cos \theta d\theta dE, \quad (3.3)$$

where we have represented the step function absorptivity  $A(E)$  through the limits of integration.

The external luminescence yield,  $\eta_{ext}$ , is defined as the ratio of the rate of radiative flux out the top,  $L_{ext}$ , to the total loss rate of photons from the cell. We assume the cell is free of non-radiative recombination in this analysis. Thus, the total loss rate of photons is given as  $L_{ext} + L_{int\downarrow}$ , where  $L_{int\downarrow}$  is the radiative flux out the bottom to the next cell below:

$$\eta_{ext} = \frac{L_{ext}}{L_{ext} + L_{int\downarrow}}. \quad (3.4)$$

The absorption of photons from the sun is  $\int a(E)S(E)dE$ , where  $S$  is the number of photons in the solar spectrum per unit area per unit time. The current of the solar cell is given by the absorption of photons from the sun minus the emission of photons out of the cell. From Eqn. 3.4, we get  $L_{ext} + L_{int\downarrow} = \frac{L_{ext}}{\eta_{ext}}$ . Thus the  $J - V$  characteristic of the top cell is given by:

$$J_1(V_1) = \int_{E_{g1}}^{\infty} S(E)dE - L_{ext} - L_{int\downarrow} = \int_{E_{g1}}^{\infty} S(E)dE - \frac{1}{\eta_{ext}} \pi \exp\left(\frac{qV_1}{kT}\right) \int_{E_{g1}}^{\infty} b(E)dE, \quad (3.5)$$

where  $J_1$  is the current density and  $V_1$  is the voltage of the top cell. The value of  $V_1$  should be chosen to be the maximum power point of the cell to extract maximum power from the top cell.

The expression for the open circuit voltage of the top cell is given by setting  $J = 0$  in Eqn. 3.5:

$$V_{oc,1} = \frac{kT}{q} \ln\left(\frac{\int_{E_{g1}}^{\infty} S(E)dE}{\pi \int_{E_{g1}}^{\infty} b(E)dE}\right) - \frac{kT}{q} \ln\left(\frac{1}{\eta_{ext}}\right). \quad (3.6)$$

From Eqn. 3.6, we see that the open circuit voltage penalty when  $\eta_{ext} < 1$  is  $\frac{kT}{q} \ln\left(\frac{1}{\eta_{ext}}\right)$ .

We now consider the second cell beneath the first cell. The absorption of photons from the sun is now given as  $\int_{E_{g2}}^{E_{g1}} S(E)dE$ , (assuming step function absorptivity for the second cell as well). In the  $J - V$  characteristic of the second cell, there is an extra term to account for the radiative flux out of the bottom of the top cell that is absorbed by the second cell. Since from Eqn. 3.4,  $L_{int\downarrow} = \frac{L_{ext}}{\eta_{ext}} - L_{ext}$ , the downward flux is given by:

$$L_{int\downarrow} = \left(\frac{1}{\eta_{ext}} - 1\right) \pi \exp\left(\frac{qV_1}{kT}\right) \int_{E_{g1}}^{\infty} b(E)dE. \quad (3.7)$$

By analogy to Eqn. 3.5 the  $J - V$  characteristic of the second cell is thus given by:

$$\begin{aligned} J_2(V_2, V_1) = \int_{E_{g2}}^{E_{g1}} S(E)dE + \left(\frac{1}{\eta_{ext,1}} - 1\right) \pi \exp\left(\frac{qV_1}{kT}\right) \int_{E_{g1}}^{\infty} b(E)dE \\ - \frac{1}{\eta_{ext,2}} \pi \exp\left(\frac{qV_2}{kT}\right) \int_{E_{g2}}^{\infty} b(E)dE, \end{aligned} \quad (3.8)$$

where  $\eta_{ext,1}$  refers to the external fluorescence yield of the top cell, and  $\eta_{ext,2}$  refers to the second cell. The derivation of the  $J - V$  characteristic for cells below the second follows the same procedure as for the second cell.

## 3.2 Structures

### Case (1): No Intermediate Mirror, No Back Reflector

We first consider the case of a dual bandgap solar cell without an intermediate mirror or back mirror (see Fig. 3.2). The top and bottom cells are index matched, on an absorbing substrate, and we assume a perfect antireflection coating on the top cell. We assume that the

**Case (1) Dual Bandgap Cell**

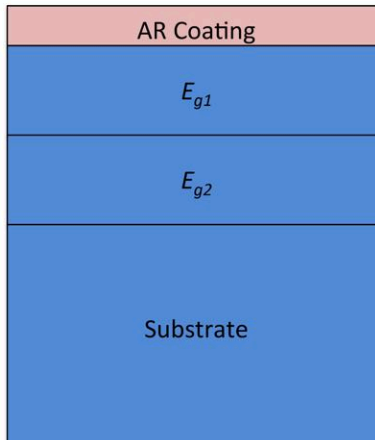


Figure 3.2: Case (1); a dual bandgap solar cell without an intermediate or a back mirror; the top cell, bottom cell, and substrate are index matched with  $n_s = 3.5$ .

cells are optically thin to the luminescent photon energies. As discussed in Chapter 2, though it appears contradictory to assume both step-function absorption and weak absorption of internal luminescence, this approximation is actually reasonable.

The external luminescence yield,  $\eta_{ext}$ , can also be described as the probability that an absorbed photon escapes out the front surface [5]. For the limit of a very optically thin cell, we can determine that  $\eta_{ext} \approx \frac{1}{4n_s^2}$  by recognizing that the probability of front surface escape, relative to substrate absorption, is the fraction of solid angle that is subtended by the escape cone [13], as discussed in Chapter 2. We plot the efficiencies as a function of bandgaps in Fig. 3.2. In Fig. 3.2, and in the following calculations, we assume cell temperature of  $T = 20^\circ C$ , two terminal connections to each cell, 1 sun concentration, and an index of refraction of  $n_s = 3.5$  for all the cells. We model the radiation from the sun with the Air Mass 1.5 Global tilt spectrum [26].

**Case (2): No Intermediate Mirror, Perfect Back Reflector**

The second case we consider is a multi-bandgap solar cell without an intermediate reflector, with a perfect back mirror (see Fig. 3.2). The top and bottom cells are index matched, and we assume a perfect antireflection coating on the top cell. The  $\eta_{ext}$  for the top cell remains the same as in Case (1), but we have  $\eta_{ext} = 1$  for the bottom cell. The top cell basically acts as a transparent layer to the internal luminescence from the bottom cell, as these photons are low enough in energy. The efficiency of this structure as a function of bandgaps is plotted in Fig. 3.2.

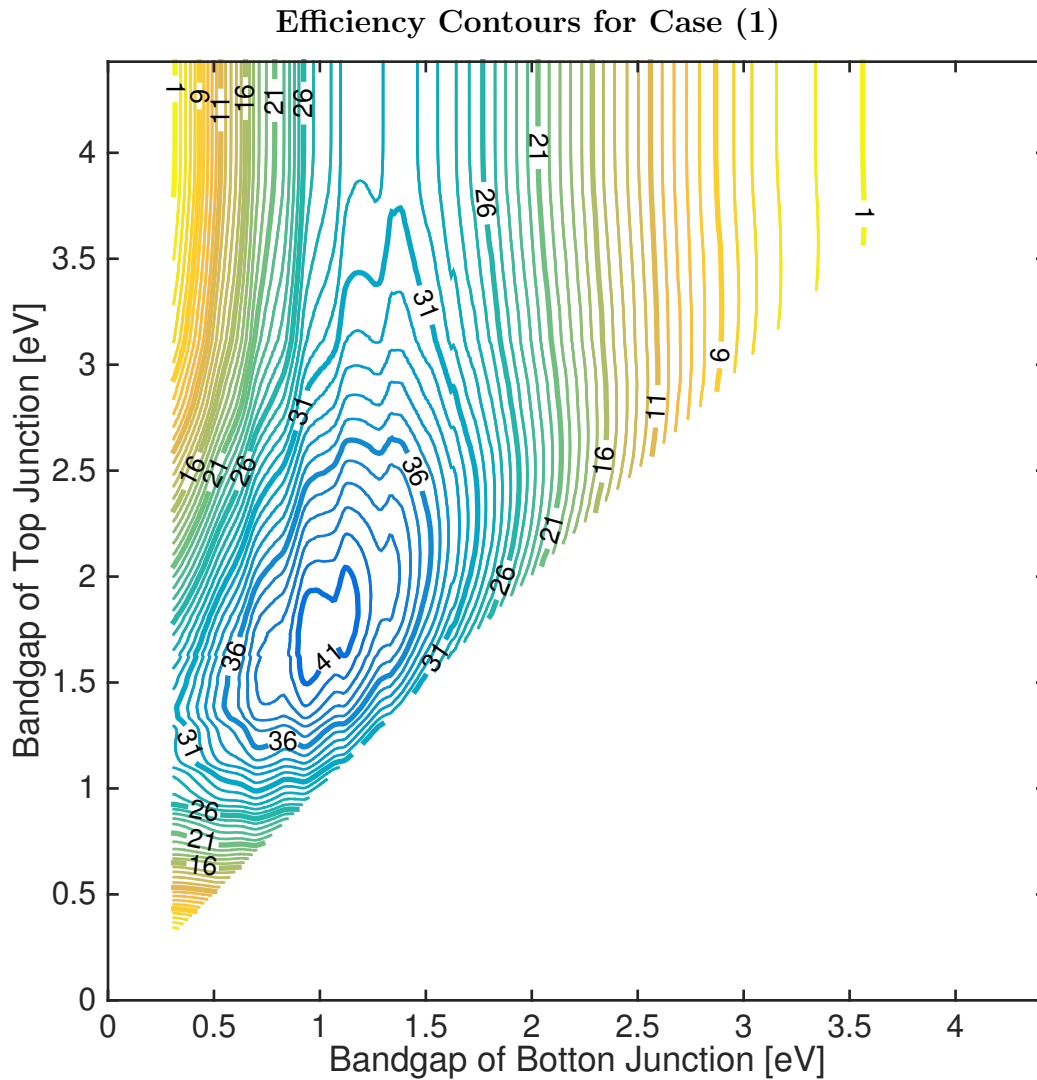


Figure 3.3: The efficiencies as a function of top and bottom bandgap for Case (1), a dual junction solar cell without an intermediate or a back mirror; the cells are assumed to be optically thin to the internally luminescent photons.

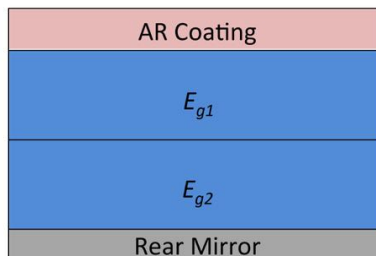
**Case (2) Dual Bandgap Cell**

Figure 3.4: Case (2); a dual bandgap solar cell without an intermediate mirror but with a back mirror; the top and bottom cells are index matched with  $n_s = 3.5$ .

**Case (3): An Air Gap Intermediate Mirror, Perfect Back Mirror**

An intermediate mirror for a dual bandgap cell must satisfy the requirements of (1) reflecting the internally luminescent photons of the top cell and (2) transmitting the externally incident photons that are below the bandgap of the top cell but above the bandgap of the bottom cell.

These dual requirements for an intermediate mirror appear difficult to satisfy, as we must satisfy them for photons at all energies and angles. Air gaps provide the following opportunity:

- (1) We obtain total internal reflection for the photons outside of the escape cone, as described by Snell's law. Due to the high index mismatch between the semiconductor and air, most of the internally luminescent photons are outside the escape cone and are thus reflected.
- (2) The externally incident photons, upon entrance into our structure, refract into the escape cone of the top cell material, as described by Snell's law. Thus, we can use antireflection coatings to transmit the photons in the escape cone to the next cell.

The internally luminescent photons are created at all angles, while the transmitted solar photons have a limited angular range. Therefore angular filtering by an air gap can be employed instead of spectral filtering, to recycle the luminescent photons.

We assume an air gap for the intermediate mirror, sandwiched by perfect antireflection coatings, as well as a perfect back mirror and perfect top antireflection coating, see Fig. 3.2. In this scenario,  $\eta_{ext,1} = 0.5$ , as the front and back interfaces of the top cell are identical. With a perfect back reflector,  $\eta_{ext,2} = 1$ , as all the photons must eventually escape out the front of the device.

In Fig. 3.2, we plot the efficiency of the dual bandgap cell as a function of top and bottom bandgaps, assuming an air gap intermediate mirror, sandwiched by perfect antireflection coatings, as well as a perfect back mirror, and perfect top antireflection coating.

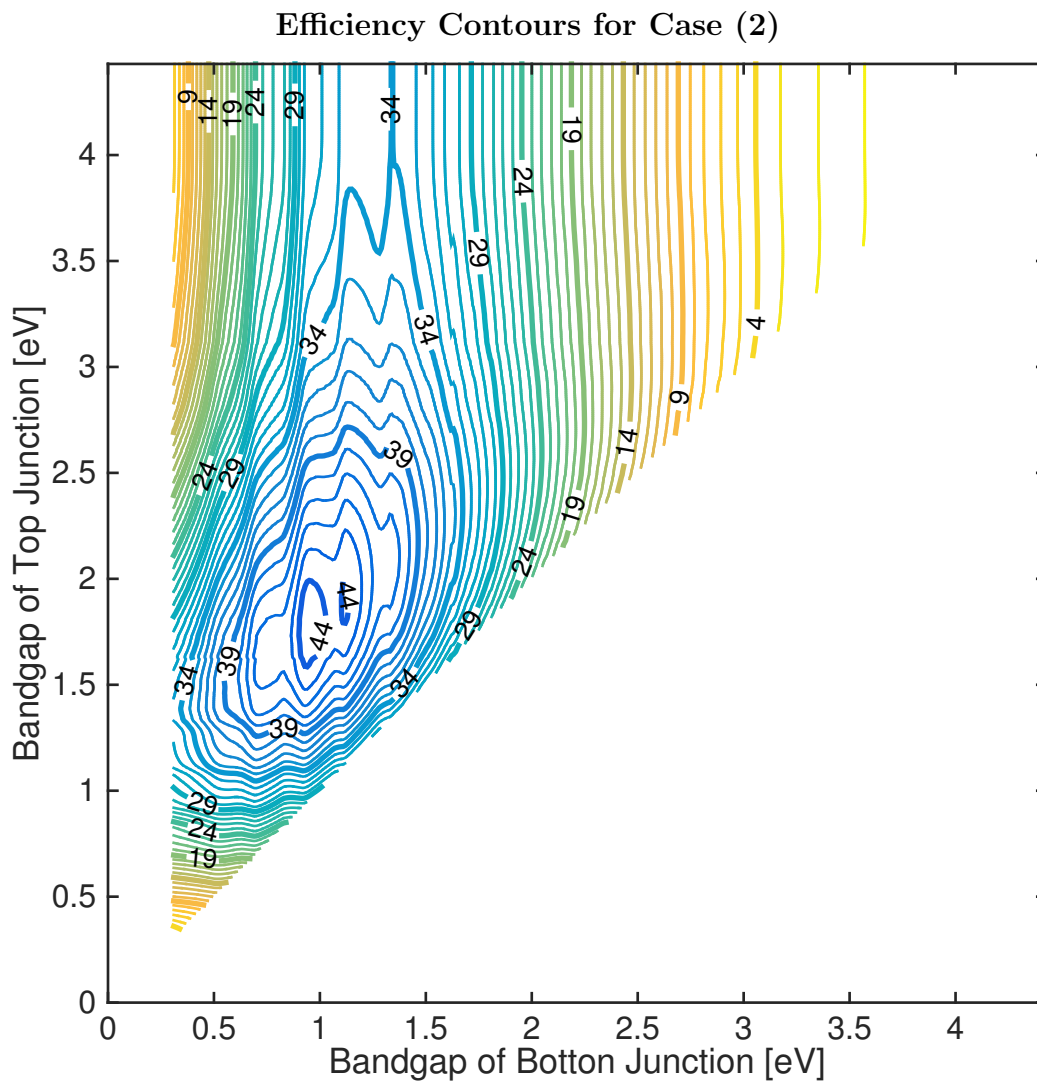


Figure 3.5: The efficiencies as a function of top and bottom bandgap for Case (2), a dual junction solar cell without an intermediate or a back mirror.

Case (3) Dual Bandgap Cell



Figure 3.6: Case (3); a dual bandgap solar cell with an air gap intermediate mirror, with perfect antireflection coatings and a perfect back mirror.

### 3.3 Optimal 2-Bandgap Cell

In Table 3.3 we compare the efficiencies for the optimal pairs of bandgaps in Cases (1)-(3). We pick up  $\approx 5\%$  absolute in efficiency for going from a naïve design with no mirrors (Case (1)), to an advanced optical design with intermediate and back mirrors (Case(3)).

Table 3.1: Efficiency of Best Dual Bandgap Cells

	$E_{g1}$	$E_{g2}$	Efficiency
Case (1)	1.73 eV	0.95 eV	41.9%
Case (2)	1.74 eV	0.94 eV	44.7%
Case (3)	1.73 eV	0.94 eV	46.3%

To isolate the effect of the intermediate mirror, we compare Case (2) (no intermediate mirror, perfect back mirror) with Case (3) (air gap intermediate mirror, perfect back mirror). In Fig. 3.3, we plot the open circuit voltage of the top cell, short circuit current of the bottom cell, and overall cell efficiency for Case (1) and Case (3). The optimal bandgaps from Case (3) are used in this comparison ( $E_{g1}=1.73$  eV and  $E_{g2}=0.94$  eV).

Eqn. 3.6 allows us to calculate the open circuit voltage penalties from ideal. The thermal voltage is 25 mV, so in Case (3), with the air gap intermediate mirror, the top cell sees a voltage penalty of  $25mV \times \ln(2) = 17mV$ . With no intermediate mirror, as in Case (2), the top cell sees a voltage drop of  $25mV \times \ln(4n_s^2) = 97mV$ , with  $n_s = 3.5$ . Thus, as we see in Fig. 3.3, the top cell voltage difference between Case (2) and Case (3) is 80mV.

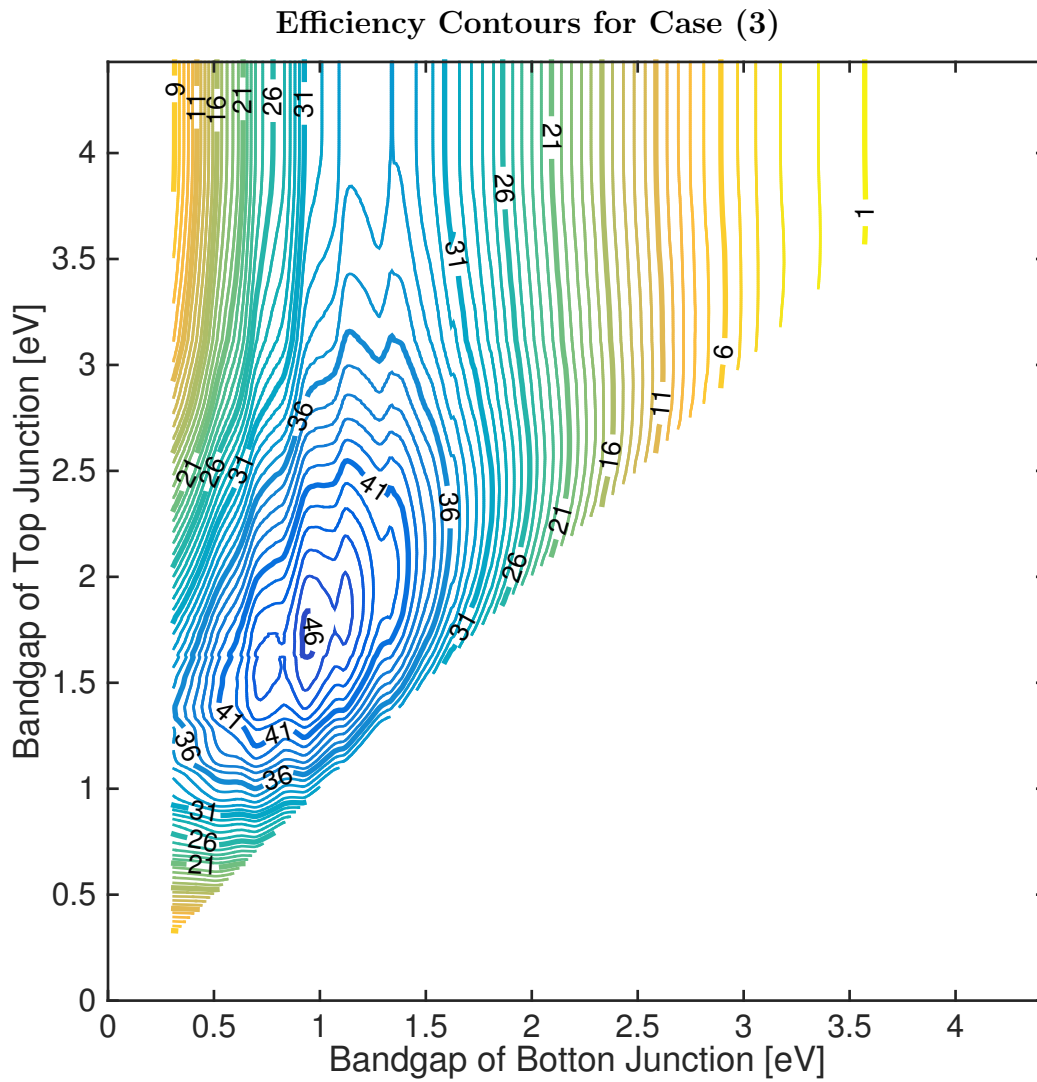


Figure 3.7: The efficiencies as a function of top and bottom bandgap for Case (3), a dual junction cell with an air gap intermediate mirror and perfect back mirror.

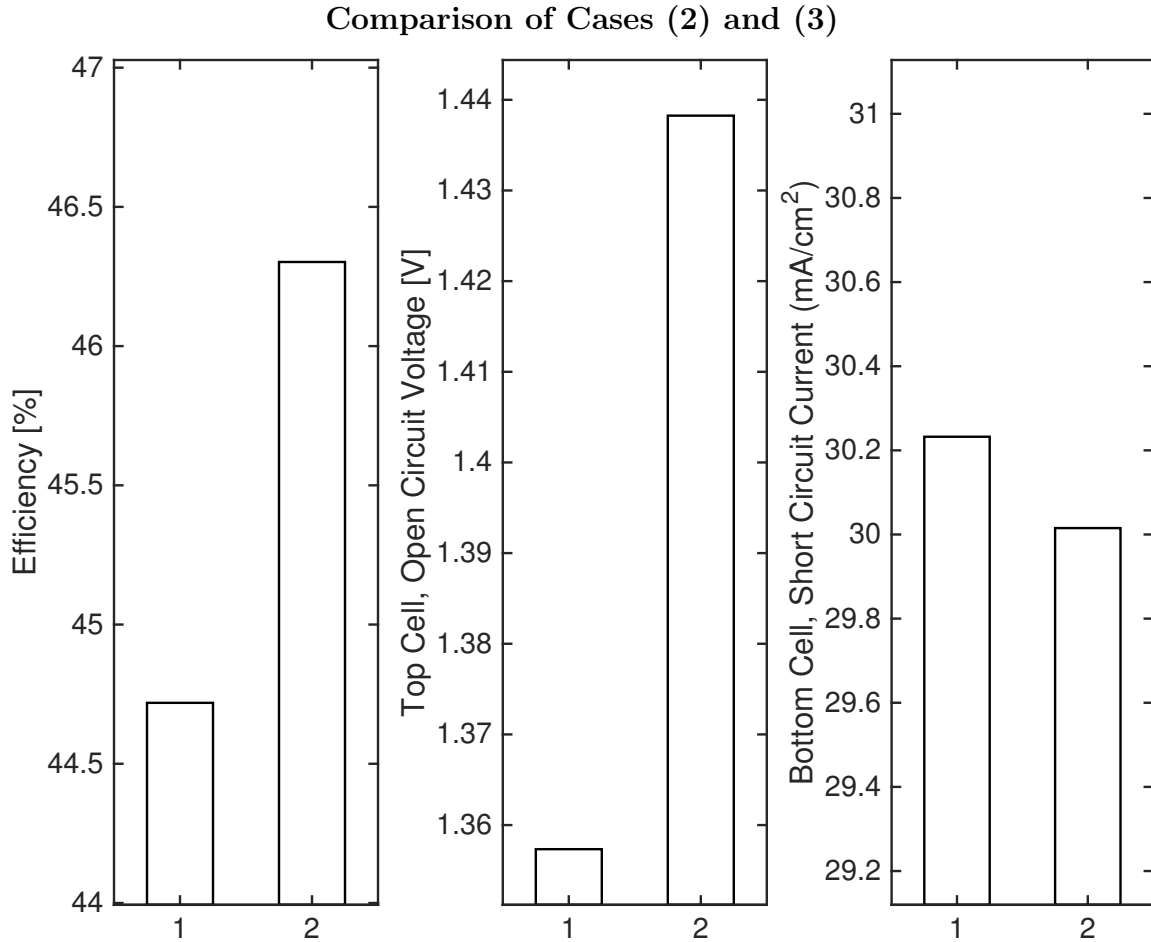


Figure 3.8: Tandem cell efficiency, top cell open circuit voltage, and bottom cell current for bandgaps  $E_{g1} = 1.73$  eV and  $E_{g2} = 0.94$  eV, for Case (2); no intermediate mirror and a perfect back mirror, assuming optically thin cells and Case (3); an air gap intermediate mirror and a perfect back mirror.

As a result of the intermediate mirror, there is also a slight decrease in current in the bottom cell. This current decrease is due to the loss of radiative emission out the back of the top cell that is then absorbed by the bottom cell. The effect of current loss in the bottom cell is not enough to offset the effect of gain in voltage of the top cell with the intermediate mirror. Thus the tandem efficiency increases by  $\approx 2\%$  absolute with the air gap intermediate mirror.

### 3.4 Optimal Multi-Bandgap Cells

We now calculate the limiting efficiency of multi-bandgap cells with 1 through 6 bandgaps, for Cases (1)-(3), see Table 3.4. The efficiencies are calculated at the optimal bandgaps; the bandgaps for 4-6 cells are taken from [20].

Table 3.2: Efficiency of Best Multi-Bandgap Cells

# of Bandgaps	$E_{g1}$	$E_{g2}$	$E_{g3}$	$E_{g4}$	$E_{g5}$	$E_{g6}$	Case (1)	Case (2)	Case (3)
1	1.34						30.7%	34.0%	
2	1.73	0.94					41.9%	44.7%	46.3%
3	2.04	1.40	0.93				48.0%	49.8%	52.1%
4	2.23	1.63	1.14	0.70			51.3%	53.0%	56.1%
5	2.39	1.83	1.37	0.97	0.70		53.9%	55.0%	58.5%
6	2.53	2.02	1.64	1.34	0.96	0.69	55.7%	56.7%	60.3%

In this chapter, we have assumed  $n_s = 3.5$  for the refractive indices of all the cells. Due to the large refractive index mismatch with air ( $n = 1$ ), the escape cone given by Snell's law is  $\sin^{-1}(\frac{1}{3.5}) \approx 17^\circ$  from the normal. Thus, when there is no back mirror, the photon escape probability from the top surface,  $\eta_{ext}$ , is greatly diminished. Looking at Table 3.4 and Fig. 3.3, we see that we pick up  $\approx 2\%$  from the intermediate mirror in the case of 2 bandgaps. For more bandgaps, we pick up a similar absolute efficiency increase.

### 3.5 Practical Considerations

Refs. [19], [27], [28] achieve experimental efficiencies of 31.1%, 30.8%, and 30.3%, respectively, for the tandem cell of InGaP ( $E_g = 1.8$  eV) on GaAs ( $E_g = 1.4$  eV). We extract the limiting efficiencies from Figs. 2-6 for these materials and list in Table 3.5. For this combination of bandgaps, the absolute efficiency increase from Case (1) to Case (3) under 1 sun is 2.7%. Though the air gap presents mechanical and manufacturing difficulties, it is a feasible architecture, as demonstrated experimentally in [29]. Future work can take into account the detailed absorption spectrum of real materials, non-radiative recombination,

the actual quality of the antireflection coatings, shading losses between cells, resistive losses from introducing contact fingers above and below each cell, and the actual differing indices of refraction for the sub-cells, among other non-idealities.

Table 3.3: Efficiency of InGaP (1.8 eV) & GaAs (1.4 eV) Dual Bandgap Cells

	Efficiency
Case (1)	37.8%
Case (2)	39.1%
Case (3)	40.5%

## 3.6 Chapter Summary

An intermediate reflector has the dual burden of reflecting the internally luminescent photons and transmitting below bandgap photons. We thus propose an air gap sandwiched with antireflection coatings to serve as the intermediate reflector, using angular selectivity by total internal reflection to achieve frequency selectivity. Together with a perfect back mirror, in dual bandgap cells, this results in a  $\approx 5\%$  absolute efficiency improvement over cells without mirrors.

## Chapter 4

# Design of Subwavelength Light Trapping Textures

Light trapping in solar cells allows for increased current and voltage, as well as reduced materials cost. It is known that in geometrical optics, a maximum  $4n^2$  absorption enhancement factor can be achieved by randomly texturing the surface of the solar cell, where  $n$  is the material refractive index. This ray-optics absorption enhancement limit only holds when the thickness of the solar cell is much greater than the optical wavelength. In subwavelength thin films, the fundamental questions remain unanswered:

- (1) what is the subwavelength absorption enhancement limit and
- (2) what surface texture realizes this optimal absorption enhancement?

We turn to computational electromagnetic optimization in order to design nanoscale textures for light trapping in subwavelength thin films. For high-index thin films, in the weakly absorbing limit, our optimized surface textures yield an angle- and frequency-averaged enhancement factor  $\approx 39$ . They perform roughly 30% better than randomly textured structures, but they fall short of the ray optics enhancement limit of  $4n^2 \approx 50$ .

Texturing of solar cell surfaces allows for absorption enhancement, owing to the coupling of incident light rays to totally internally reflected modes within the cell, i.e. light trapping. It is known that in the ray-optics regime, where the thickness of the solar cell is much greater than the wavelength of light, that the maximum absorption for weakly absorbed rays is given by [13]:

$$A = \frac{\alpha d}{\alpha d + \frac{1}{4n^2}}, \quad (4.1)$$

where  $\alpha$  is the absorption coefficient,  $d$  the thickness of the material, and  $n$  the index of refraction. This maximum absorption limit assumes a perfect rear mirror. We can compare this to the single-pass absorption of weakly absorbed light:

$$A = 1 - e^{-\alpha d} \approx \alpha d. \quad (4.2)$$

The absorption enhancement is the actual absorption divided by the single pass absorption. The maximum absorption enhancement in the ray-optics regime is thus given by Eqn. 4.1 divided by Eqn. 4.2; in the limit of a very weakly absorbing material the absorption enhancement is given by  $4n^2$ .

With light trapping, we can achieve high absorption, even for thin absorber layers. Short circuit current ( $J_{sc}$ ) and fill factor improvements occur due to better carrier extraction in thin layers. Additionally, open circuit voltage ( $V_{oc}$ ) improvements occur, owing to better photon extraction [30]. In high quality materials, such as gallium arsenide, efficiency improvement can be substantial, due to improvement in external fluorescence yield [5], [31]. We also reduce material cost by achieving the same current in a thinner material.

In recent years, light trapping has seen renewed interest in the subwavelength regime, which is applicable to increasingly thin solar cells [32], [33]. Current high efficiency GaAs cells are  $\approx 2$   $\mu\text{m}$  thick, and if we want to reduce that thickness to  $\approx 100$  nm, subwavelength light trapping textures are necessary. In this subwavelength regime, where the thickness of the solar cell is less than the optical wavelength, traditional ray optics does not hold, and the fundamental unanswered questions are: what is the upper bound on absorption enhancement, and what surface texture realizes this limit?

In the subwavelength regime, there are discrete propagating modes (i.e. modes that are totally internally reflected), which can no longer be modeled as a continuum density of states. Stuart and Hall [34] attempted to establish the absorption enhancement limit in the subwavelength by accounting for these discrete propagating modes, but they make the assumption that the introduced texture does not change the modal structure from that of a flat slab. This assumption does not hold, especially for thin solar cells where the amplitude of the texture is on the order of the thickness. In order to calculate a true limit in the subwavelength, the full modal structure needs to be taken into account, self-consistently. Yu et al. [33], [35], [36] also attempt to establish a fundamental limit in the subwavelength regime, but their approach depends on knowledge of the modal structure. In this work, we make no assumptions about the modal structure. We numerically find the optimal subwavelength surface texture by using computational inverse electromagnetic design.

Our work differs from prior efforts to find the optimal surface texture for thin absorber layers in the following ways:

- (1) Our absorber thickness is subwavelength, i.e. the wavelength of the light in the material is greater than the average thickness of the material. Many papers look at texturing for absorber thicknesses in the micron range [37]–[48], a regime generally governed by ray optics.
- (2) To evaluate the light trapping performance of a texture for a flat-plate, non-concentrating, non-tracking solar cell, we report the absorption enhancement averaged over frequency and over all angles in the hemisphere. A valid comparison against the ray optics limit must be angle- and frequency-averaged, instead of over a limited angular range [37]–[39], [48]–[53] or a narrowband of frequencies [54], [55].

- (3) To derive general principles, we treat a weakly absorbing material with broadband, single-pass absorption of 1.6%. This weak single pass absorption reveals the full benefit of light trapping. Stronger absorbance would saturate the maximum absorption enhancement possible, as seen in Refs. [43], [56]–[64].
- (4) We utilize a high index absorber material with  $n = 3.5$ . Though Refs. [32], [37], [65] exceed the ray optics limit for subwavelength absorber layers, they do so for a low-index absorber ( $n < 2$ ) sandwiched by a higher index cladding.
- (5) In our optimization, we look for the most general optimal 3D texture, rather than optimizing a 2D texture (with no variation along the third dimension) [55], [66] or making constraints on the shape, such as optimizing 1D or 2D grating parameters [37], [43], [52], [60] or the arrangement of nanowires [44].

## 4.1 Optimization Algorithm

The optimization geometry is shown in Fig. 4.1, and is meant to be consistent with the practical requirements of a thin film solar cell. The setup consists of a weakly absorbing semiconductor material of index  $n = 3.5$ , with average thickness of 100 nm, and a flat top surface compatible with a conventional anti-reflection coating. The unknown texture on the bottom surface is specified within 2D periodic boundary conditions. The absorption is evaluated in the important solar frequency range, 350 THz to 400 THz (1.45 eV to 1.65 eV, or 750 nm to 860 nm free space wavelength), a bandwidth relative to center frequency of 1/8. This is a bandedge photon energy range where even a direct bandgap semiconductor like GaAs needs some absorption assistance. We do not consider the full solar spectral bandwidth when designing a surface texture, since at most higher frequencies the direct gap absorption is sufficient. Note that Maxwell’s Equations are scale-invariant, meaning that solutions described here can be scaled to different bandgaps.

The average thickness of 100 nm is less than a half wavelength in the material, placing us in the subwavelength regime. An artificial weakly absorbing material ( $n_{real} = 3.5$  and  $\alpha = 1.6 \times 10^3 \text{ cm}^{-1}$ ) is chosen in order to arrive at general conclusions related to weak optical absorption. The semiconductor is specified to have a uniform  $\alpha d = 0.016$  single-pass absorption throughout the band, small enough to benefit from light trapping, but large enough to allow faster numerical convergence and accuracy. A more highly absorbing material might saturate at 100% absorption, obscuring the benefit of the surface texturing.

An antireflection (AR) coating is applied to the top of the solar cell structure: it is fixed at a quarter wavelength (108 nm) for the center wavelength in the optimization bandwidth, with  $n_{AR} = \sqrt{n_{air} \times n_{absorber}} = 1.85$ . A bottom surface texture was chosen for the absorber layer so we can keep the antireflection coating fixed in our optimization algorithm. Beneath the absorber layer is a non-absorbing back dielectric layer of  $n = 1.5$  (adjusted to 133 nm average thickness) followed by a perfect back reflector.

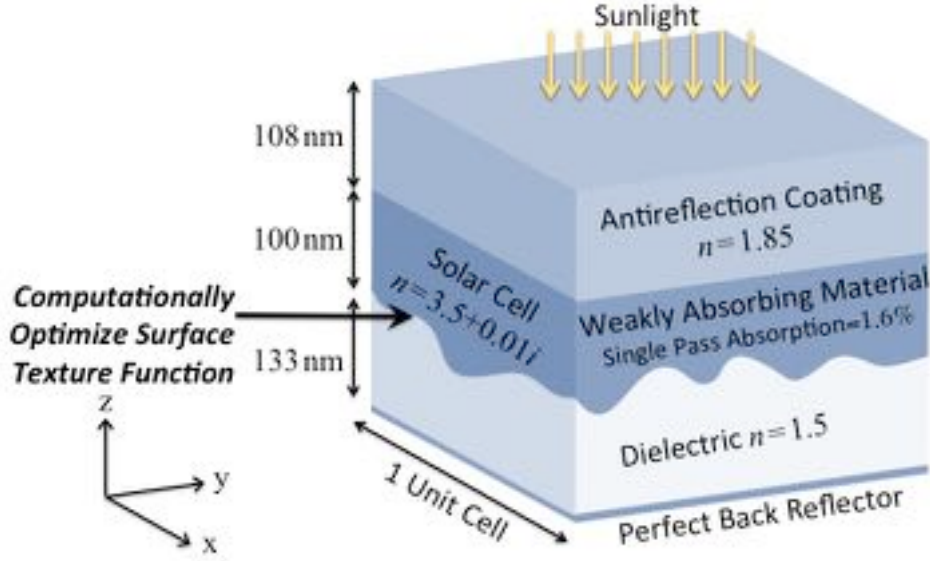


Figure 4.1: The bottom surface texture of the absorbing material is computationally optimized. This diagram is a schematic of 1 unit cell; there are periodic boundary conditions along the  $yz$  and  $xz$  planes.

The periodic surface texture function,  $h$ , is represented by a truncated Fourier series:

$$h(x, y) = \sum_{m=-2}^2 \sum_{n=-2}^2 c_{mn} e^{i \frac{m2\pi x}{\Lambda_x}} e^{i \frac{n2\pi y}{\Lambda_y}}, \quad (4.3)$$

where  $\Lambda$  is the periodicity, and  $c_{mn}$  are the Fourier coefficients. In our optimization algorithm, we keep the periodicity and the zeroth order Fourier coefficient (the average absorber layer thickness) fixed, and allow the other Fourier coefficients to evolve. We truncate the Fourier series to avoid small highly resonant features that would not be robust in manufacturing.

Our optimization algorithm scripts are written in MATLAB [67], following the procedure described in Ref. [30]. Our optimization uses an adjoint gradient method to search for a local optimum [68]. We describe this method further in the next section. To find the absorption of the solar cell, we simulate the solar cell structure of Fig. 4.1 in “Lumerical FDTD Solutions,” [69] a commercial finite-difference time-domain solver for Maxwell’s Equations, evaluating the absorption at 30 points within the frequency bandwidth. Each iteration takes approximately 15 minutes on our computational cluster of 128 cores, and the optimization converges after about 25 iterations.

The selection of the Figure of Merit is critical. We maximize the absorption enhancement at the frequency with the lowest absorption, a minimax Figure of Merit [70], which allows us to achieve good absorption over the whole frequency band. In one iteration, we evaluate the absorption for each frequency, at each of the two perpendicular polarizations of normally

incident light. We then take the lowest absorption as the Figure of Merit. At the end of the optimization, we compute the angle-averaged performance. The Lambertian angle-averaged performance as a function of frequency is given by:

$$\int_0^{2\pi} \int_0^{\frac{\pi}{2}} AE(\theta, \phi) \times \cos(\theta) \times \sin(\theta) d\theta d\phi, \quad (4.4)$$

where  $AE$  is the absorption enhancement found by dividing the absorption by the average single pass absorption  $\alpha d = 0.016$ , and averaging over the two perpendicular polarizations. At the end of the full optimization, we evaluate Eq. 4.4 by simulating 12 angles over the hemisphere, with two orthogonal polarizations for every angle.

## 4.2 Adjoint Method for Electromagnetic Optimization

In order to optimize the surface texture for increased absorption enhancement, we first find the gradient of our figure of merit with respect to our shape parameters, and then use these gradients with the method of steepest descent to update our texture. In this section, we describe the adjoint method, a way to obtain the gradients in constant time, regardless of the number of shape parameters.

We want to increase the absorption, and equivalently, the Poynting vector into the solar cell material (see Figure 4.2) by optimizing a periodic surface texture function. (We really want to optimize for absorption enhancement, but that is the same thing as optimizing for the absorption, given that we keep the average thickness constrained to a constant value.) The question we ask is: at what  $x'$  should a small piece of material be added, and at what  $x'$  should material be removed to increase my Figure of Merit (see Figure 4.3)? We could do  $n + 1$  electromagnetic simulations, 1 initial simulation then 1 per grid point to figure this out, but that is very computationally intensive.

$$\begin{aligned} J &= \text{Figure of Merit} \\ &= \frac{1}{P_{\text{inc}} * \alpha L} \int \frac{1}{2} \text{Re} \left[ \vec{E}(x) \times \vec{H}^*(x) \right] \cdot (-\hat{z}) dx \\ &\approx \frac{\delta A}{P_{\text{inc}} * \alpha L} \sum_n \frac{1}{2} \text{Re} \left[ \vec{E}(x_n) \times \vec{H}^*(x_n) \right] \cdot (-\hat{z}) \\ &= \frac{\delta A}{P_{\text{inc}} * \alpha L} \sum_n \frac{1}{2} \text{Re} \left[ E_y(x_n) H_x^*(x_n) - E_x(x_n) H_y^*(x_n) \right] \end{aligned}$$

We can derive the change in figure of merit due to adding a piece of material at a particular  $x'$  (see Figure 4.4):

$$\delta J \approx \frac{\partial J}{\partial E_y} \delta E_y + \frac{\partial J}{\partial H_x^*} \delta H_x^* + \frac{\partial J}{\partial E_x} \delta E_x + \frac{\partial J}{\partial H_y^*} \delta H_y^*$$

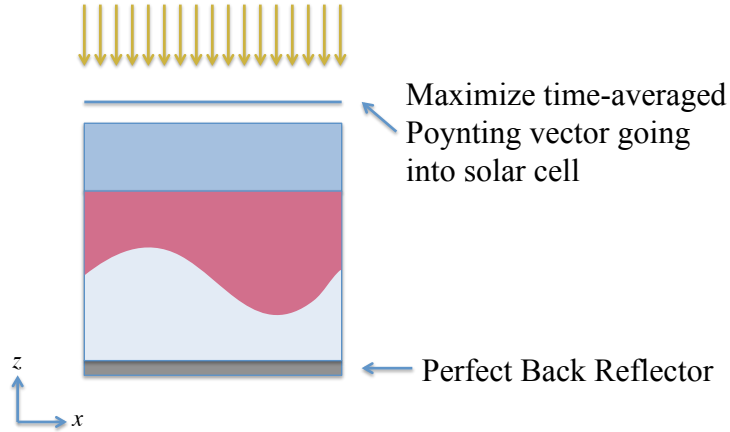


Figure 4.2: We want to increase the absorption, and equivalently, the Poynting vector into the solar cell material by optimizing a periodic surface texture function.

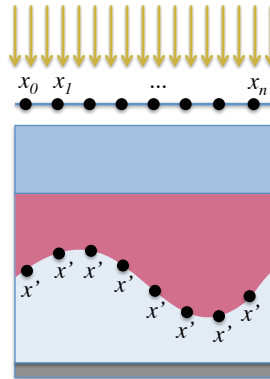


Figure 4.3: The question we ask is: at what  $x'$  should a small piece of material be added, and at what  $x'$  should material be removed to increase my Figure of Merit?

$$= \frac{\delta A}{P_{\text{inc}} * \alpha L} \sum_n \frac{1}{2} \text{Re} \left[ E_y^*(x_n) \delta H_x(x_n) + H_x^*(x_n) \delta E_y(x_n) - E_x^*(x_n) \delta H_y(x_n) - H_y^*(x_n) \delta E_x(x_n) \right]$$

The first insight needed in this method is that adding a piece of material can be approximated to adding a dipole of polarization:

$$\vec{P}(x') = \epsilon_0 \delta \epsilon_r \vec{E}^{(2)}(x')$$

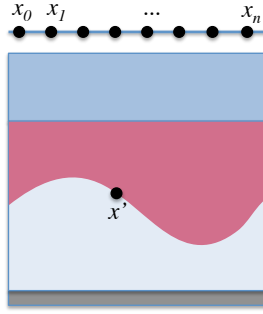


Figure 4.4: We can derive the change in figure of merit due to adding a piece of material at a particular  $x'$ .

The polarization is proportional to the electric field in the material. This cannot simply be approximated to the existing electric field, as the perpendicular component of the field is discontinuous across a material boundary.

$$\begin{aligned}
 \vec{E}^{(2)} &= \vec{E}_{\text{parallel}}^{(2)} + \frac{\vec{D}_{\text{perp}}^{(2)}}{\varepsilon^{(2)}} \\
 &\approx \vec{E}_{\text{parallel}}^{(1)} + \frac{\vec{D}_{\text{perp}}^{(1)}}{\varepsilon^{(2)}} \\
 &= \vec{E}_{\text{parallel}}^{(1)} + \frac{\varepsilon^{(1)} \vec{E}_{\text{perp}}^{(1)}}{\varepsilon^{(2)}}
 \end{aligned}$$

We obtain:

$$\vec{P} = \varepsilon_0 \delta \varepsilon_r \left( \vec{E}_{\text{parallel}}^{(1)} + \frac{\varepsilon^{(1)} \vec{E}_{\text{perp}}^{(1)}}{\varepsilon^{(2)}} \right)$$

We can express the  $\delta E$  and  $\delta H$  from the addition of a polarization with Green's functions solutions in Einstein notation (see Figure 4.5):

$$\begin{aligned}
 \delta E_i &= G_{ij}^{\text{EP}}(x_n, x') P_j \\
 \delta H_i &= G_{ij}^{\text{HP}}(x_n, x') P_j
 \end{aligned}$$

Substituting these above expressions into our expression for  $\delta J$ :

$$\delta J \approx \frac{\delta A \delta \text{Vol}}{P_{\text{inc}} * \alpha L} \sum_n \frac{1}{2} \text{Re} \left[ E_y^*(x_n) G_{xj}^{\text{HP}}(x_n, x') P_j(x') + H_x^*(x_n) G_{yj}^{\text{EP}}(x_n, x') P_j(x') \right]$$

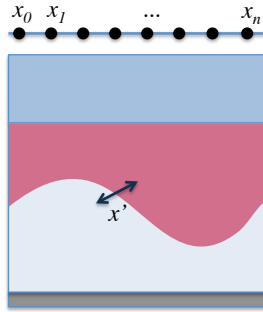


Figure 4.5: We can express the  $\delta E$  and  $\delta H$  from the addition of a polarization with Green's functions solutions in Einstein notation.

$$\left[ -E_x^*(x_n) G_{yj}^{\text{HP}}(x_n, x') P_j(x') - H_y^*(x_n) G_{xj}^{\text{EP}}(x_n, x') P_j(x') \right]$$

We have not decreased our computational burden with this dipole approximation, we still need  $n + 1$  simulations to get  $\delta J$  for adding a dipole at each  $x'$ . The second insight we need is to establish the symmetry in the Green's functions. We have, as shown visually in Figure 4.6:

$$G_{ij}^{\text{EP}}(x_n, x') = G_{ji}^{\text{EP}}(x', x_n)$$

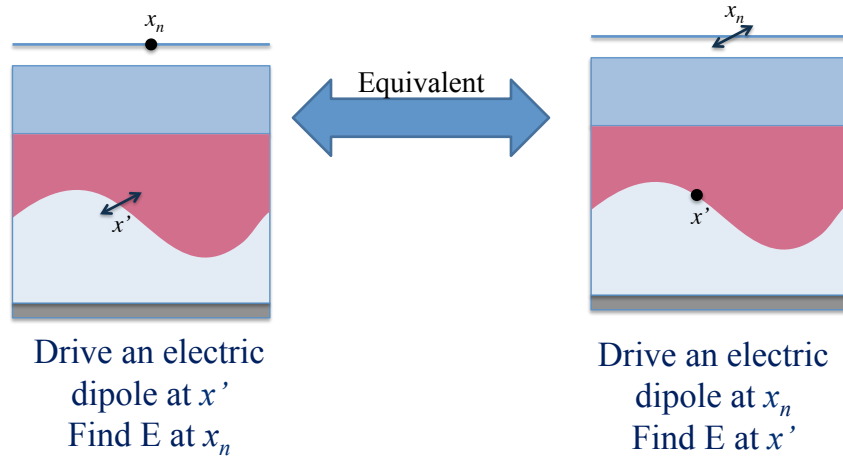


Figure 4.6: The second insight we need is to establish the symmetry in the Green's functions.

and as shown in Figure 4.7:

$$G_{ij}^{\text{HP}}(x_n, x') = -G_{ji}^{\text{EM}}(x', x_n)$$

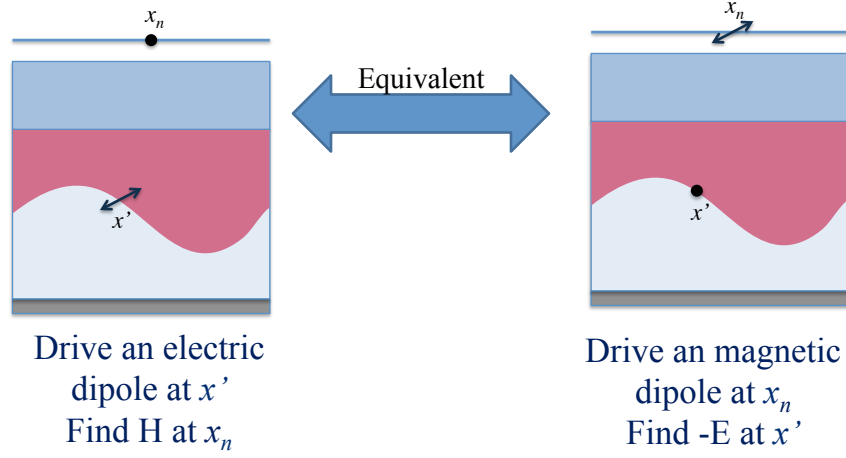


Figure 4.7: The second insight we need is to establish the symmetry in the Green's functions.

We obtain:

$$\begin{aligned}
 \delta J &= \frac{\delta A \delta \text{Vol}}{P_{\text{inc}} * \alpha L} \sum_n \frac{1}{2} \text{Re} \left[ -G_{jx}^{\text{EM}}(x', x_n) E_y^*(x_n) P_j(x') + G_{jy}^{\text{EP}}(x', x_n) H_x^*(x_n) P_j(x') \right. \\
 &\quad \left. + G_{jy}^{\text{EM}}(x', x_n) E_x^*(x_n) P_j(x') - G_{jx}^{\text{EP}}(x', x_n) H_y^*(x_n) P_j(x') \right] \\
 &= \frac{\delta A \delta \text{Vol}}{P_{\text{inc}} * \alpha L} \sum_n \frac{1}{2} \text{Re} \left[ \left( -G_{jx}^{\text{EM}}(x', x_n) E_y^*(x_n) + G_{jy}^{\text{EP}}(x', x_n) H_x^*(x_n) \right. \right. \\
 &\quad \left. \left. + G_{jy}^{\text{EM}}(x', x_n) E_x^*(x_n) - G_{jx}^{\text{EP}}(x', x_n) H_y^*(x_n) \right) P_j(x') \right] \\
 &= \frac{\delta A \delta \text{Vol}}{P_{\text{inc}} * \alpha L} \sum_n \frac{1}{2} \text{Re} \left[ \vec{E}^A \cdot \vec{P} \right] \\
 &= \frac{\delta A \delta \text{Vol}}{P_{\text{inc}} * \alpha L} \sum_n \frac{1}{2} \text{Re} \left[ \left( \vec{E}_{\text{parallel}}^A + \frac{\vec{D}_{\text{perp}}^A}{\varepsilon^{(1)}} \right) \cdot \varepsilon_0 \delta \varepsilon_r \left( \vec{E}_{\text{parallel}}^{(1)} + \frac{\varepsilon^{(1)} \vec{E}_{\text{perp}}^{(1)}}{\varepsilon^{(2)}} \right) \right]
 \end{aligned}$$

This means that instead of placing a dipole at each point where we might add or subtract material, and simulating separately to measure the  $\delta J$  at the  $x_n$ , we can place dipoles at the  $x_n$  and measure the  $\delta J$  for adding or subtracting material at the  $x'$  from one simulation.

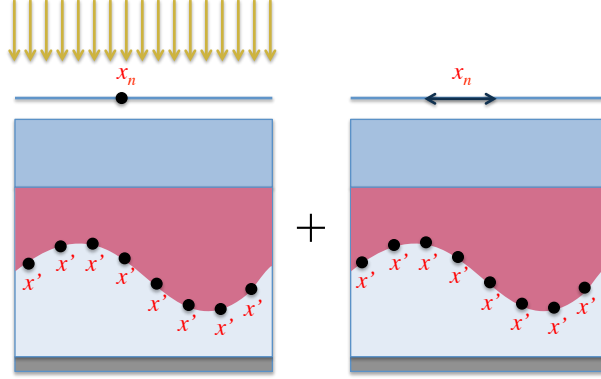


Figure 4.8: With two simulations we can calculate the Shape Derivative.

With two simulations, one for  $\vec{E}^{(1)}$  and one for  $\vec{E}^A$ , we can calculate the “Shape Derivative” (see Figure 4.8); i.e. we know the  $\delta J$  at each point along the boundary of the solar cell surface for incrementally adding or subtracting material. We can translate this to the  $\delta J$  achievable by changing the values of the Fourier series coefficients. Before, we needed  $n + 1$  simulations in order to calculate the Shape Derivative (see Figure 4.9). We are more efficient now, because we use the field data at every  $x'$ , before, we threw away this data, only using the field data at the  $x_n$  (for further detail, see Ref. [30]).

The adjoint method has also been applied successfully with problems in Fourier optics, see Refs. [71], [72].

### 4.3 Optimization Results

We started the algorithm from noisy initial conditions with fixed periodicity of 710 nm ( $= 3.1\lambda_n = 3.5$ ). We randomly picked initial Fourier coefficients in the range of 0 to 8 nm. In this first example, we achieved a minimum absorption enhancement  $AE = 32$  for a 100 nm average thickness absorber layer at normal incidence. The progression of the surface texture and absorption enhancement at normal incidence from the first iteration to the last is shown in Figs. 4.10 and 4.11. The reciprocal space representation (the magnitudes and phases of the Fourier coefficients) of the final surface is shown in Fig. 4.12. The effect of our minimax Figure of Merit in optimizing for the lowest absorbing frequency and for achieving high absorption over the full band can be seen in this progression. Resonant peaks from the initial case flatten out, and both the minimum and average absorption enhancement improve. The angle-averaged performance is shown in Fig. 4.13, Fig. 4.14 shows the angle-resolved performance. Angle- and frequency-averaged, this texture achieves an absorption enhancement of  $AE = 23$  relative to 1.6% single pass absorption.

Our optimization algorithm is sensitive to initial conditions; Fig. 4.15 shows three cases

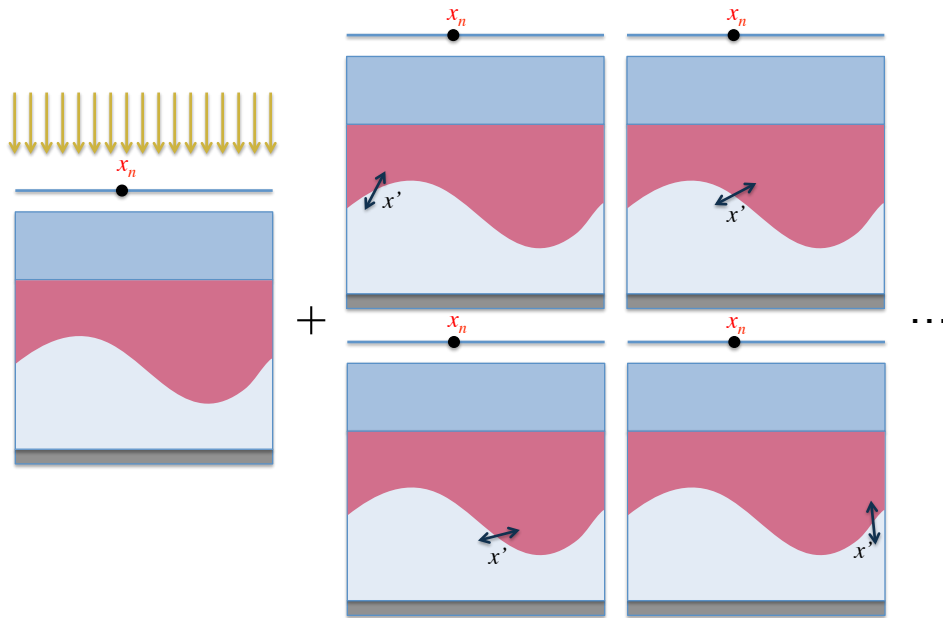


Figure 4.9: Without the adjoint method, we needed  $n + 1$  simulations in order to calculate the Shape Derivative.

of the final texture and final absorption enhancement both at normal incidence and angle averaged for different initial conditions. Figs. 4.16, 4.17, and 4.18 show the angle-resolved performance for Fig. 4.15(a), Fig. 4.15(b), and Fig. 4.15(c), respectively. From different initial conditions, we obtain different textures reaching similar angle- and frequency-averaged absorption enhancements of  $AE = 22$ ,  $24$ , and  $19$ . The best angle- and frequency-averaged absorption enhancement of  $AE = 24$  is seen in the texture in Fig. 4.15(b). A common feature of the textures is large height amplitude. The full amplitudes for the textures in Figs. 4.11, 4.15(a), 4.15(b), and 4.15(c) are  $\Delta h = 196$  nm,  $224$  nm,  $218$  nm, and  $217$  nm, respectively. The photonic bandstructure of the optimized texture from Fig. 4.15(b) is shown in Fig. 4.19. The optimization domain (the bandwidth of frequencies that we simulate) is highlighted in Fig. 4.19. The bandstructure visually shows the need for a high modal density in the optimization domain; the optimization needs modes for the incident light to couple to.

The second common feature we observe is asymmetry within the unit cell. The optimal structures appear to break the inherent mirror symmetries of the problem, with a feature growing along one of the diagonals. To demonstrate that this symmetry breaking is not an artifact of the starting noise, we started another optimization from initial symmetrized conditions, with a slight perturbation along the diagonal, as shown in Fig. 4.20. The result of the algorithm is shown 15 iterations later in Fig. 4.21 (reciprocal space diagram in Fig. 4.22). We see that this perturbation has been amplified along the diagonal, suggesting that symmetry breaking is a fundamental feature of optimal textures. There appears to be

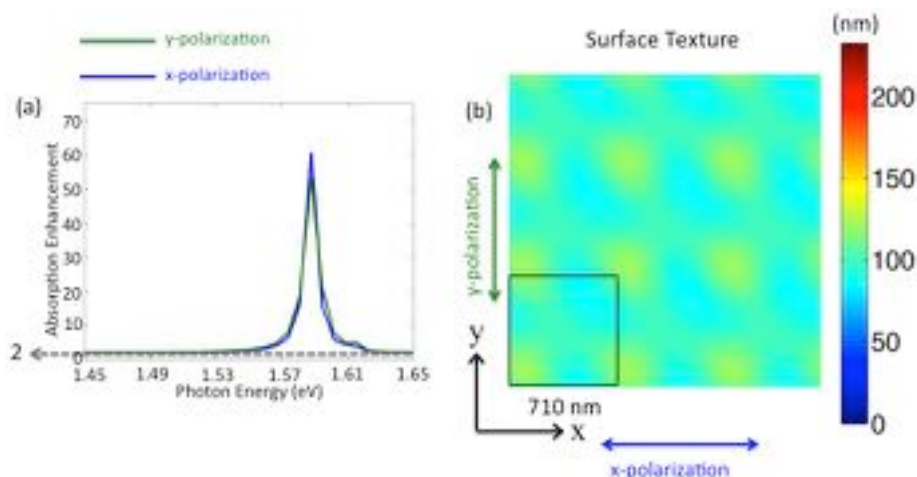


Figure 4.10: (a) The initial absorption enhancement as a function of frequency and (b) a top-down view of the surface texture; the colors show the height of the absorbing material (from the antireflection coating to the bottom dielectric, as seen in Fig. 4.1).

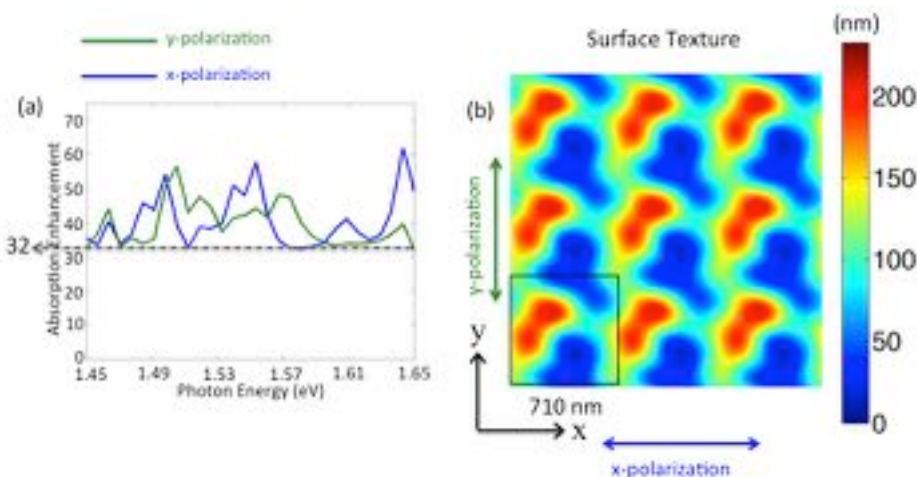


Figure 4.11: (a) The final absorption enhancement as a function of frequency and (b) a top-down view of the surface texture; the colors show the height of the absorbing material (from the antireflection coating to the bottom dielectric, as seen in Fig. 4.1).

no significance to the direction of the asymmetric component: the symmetry will break in the opposite direction (along  $x = -y$ ) if the initial perturbation is in that direction.

In our optimizations, we kept the periodicity fixed at 710 nm. To find the optimal periodicity, we ran a sweep of optimizations with fixed periodicities from 50 nm to 800 nm in increments of 50 nm. Fig. 4.23 plots the Figure of Merit (absorption enhancement at the minimum performing frequency) achieved in these optimizations. The smaller periodicities

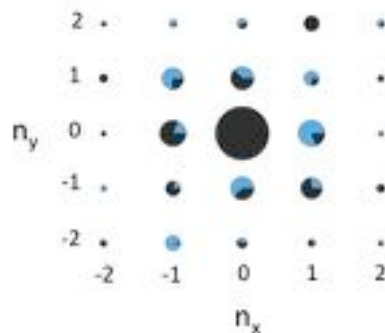


Figure 4.12: The reciprocal ( $k$ -) space representation for the final texture seen in Fig. 4.11. The blue pie slices represent the phase of the complex exponential Fourier coefficients.

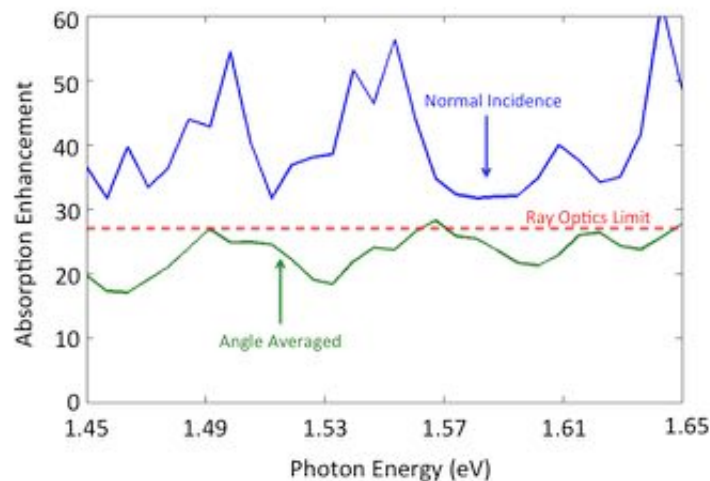


Figure 4.13: The absorption enhancement for the texture in Fig. 4.11, plotted as a function of frequency at normal incidence (blue) and angle averaged (green).

did not optimize well; periodicities less than 350 nm did not achieve minimum absorption enhancement  $AE > 10$ . The best optimizations occurred at 700 nm; perhaps because this periodicity brought the optimization frequency band high into the photonic bandstructure where the optical density of states is large.

Since the optimum is not unique, it is possible that any randomly generated pattern with large amplitude could achieve a similar Figure of Merit. To check this, we randomly generated Fourier coefficients for 100 textures with a periodicity of 710 nm, with amplitudes ranging from  $\Delta h = 223$  to 233 nm, and simulated the absorption of these structures. The

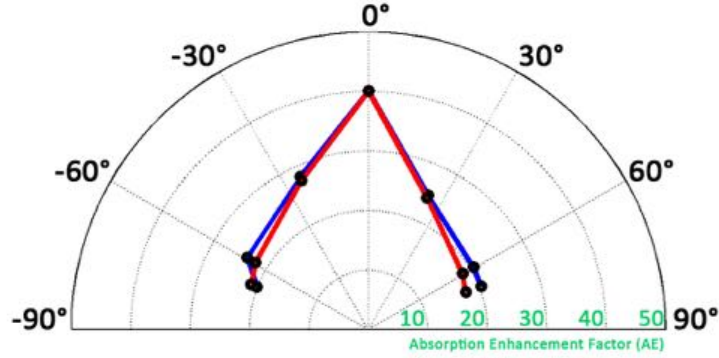


Figure 4.14: The absorption enhancement factor ( $AE$ ) averaged over frequency and polarization, as a function of incident angle  $\theta$  in the  $xz$  plane (blue) and the  $yz$  plane (red).

Figure of Merits (the lowest absorption as a function of frequency at normal incidence, for the worst performing polarization) of these random structures are plotted in Fig. 4.24, and the random texture with the median Figure of Merit  $AE = 13$  is shown in Fig. 4.25. In Figs. 4.26 and 4.27, the random texture with the median Figure of Merit is compared with the optimized texture shown in Fig. 4.15(b). The Figure of Merit for the optimized texture is over two times greater than the median Figure of Merit in the randomly generated patterns. A comparison of angle- and frequency-averaged absorption performance (shown in Fig. 4.27) shows a 33% increase in the optimized textures absorption enhancement over the median randomly generated pattern.

We also check the performance of a completely random texture (i.e. a texture with infinite periodicity). We randomly generated Fourier coefficients to the 5th order for a periodicity that is  $10\lambda_n = 3.5 = 2300$  nm, with a total texture amplitude between  $\Delta h = 223$  nm and 233 nm. Our large periodicity approximates a texture with infinite periodicity (the supercell approach). The resulting Figures of Merit for 11 different random supercell textures is shown in Fig. 4.28. The texture with the median Figure of Merit of  $AE = 13$  is shown in Fig. 4.29; this median Figure of Merit is the same as for the random textures on a 710 nm periodicity. Fig. 4.30 compares the median supercell texture to the optimized texture at normal incidence. Additionally, the angle- and frequency-averaged performance (see Fig. 4.31) of the optimized texture is 26% better than the median random supercell. Our result that a periodic texture can perform better than a random one is in agreement with Ref. [73]. Our absorption enhancement factor ( $AE$ ) results are summarized in Table 4.3.

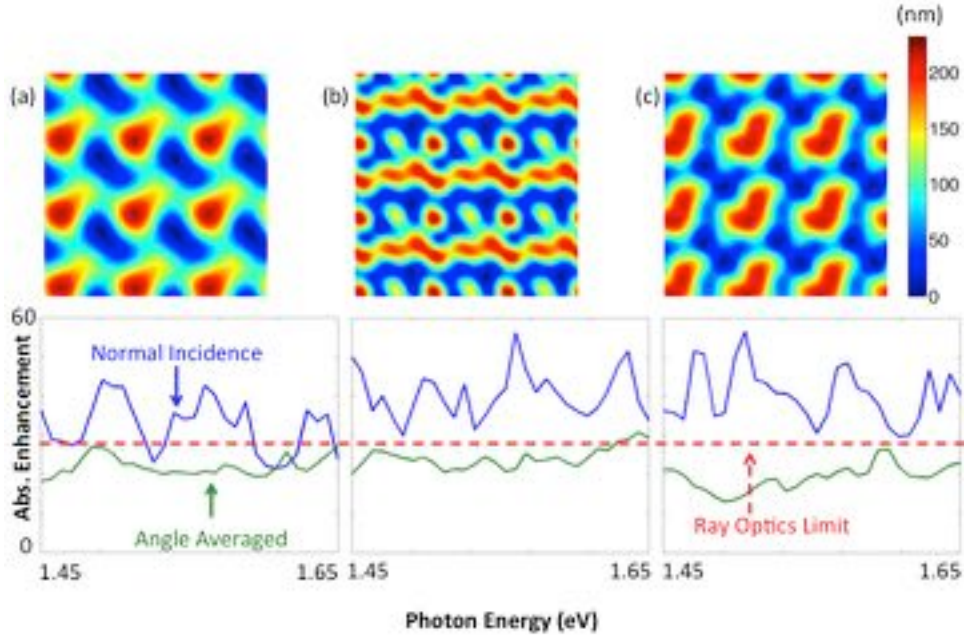


Figure 4.15: The surface textures and absorption enhancement as a function of frequency for different initial conditions, revealing a broad optimum.

In Table 4.3, the absorption enhancement factors are relative to a finite 1.6% single pass absorption. To compare these results with the  $4n^2$  ray-optics absorption enhancement limit, we need to account for the finite absorption in our structure. This can be done by using Eqn. 4.1, which can be written more generally as:

$$A = \frac{\alpha d}{\alpha d + \frac{1}{4n^2}} = \frac{\alpha d}{\alpha d + \frac{1}{E}}, \quad (4.5)$$

where  $E$  is the limiting enhancement factor when the single pass absorption is very weak ( $\alpha d < 1.6\%$ ).  $E$  represents the highest possible enhancement factor, which should be compared to the ideal  $E = 4n^2 \approx 50$  case. For our optimized case of  $AE = 24$  at  $\alpha d = 0.016$ ,  $E = 39$ .

## 4.4 Applying Manufacturing Constraints

Our practical goal in designing a solar cell texture is to achieve complete light absorption in the thinnest possible layer, with a manufacturable texture. The fact that our optimization is non-convex and there are many local optima is to our favor here. We should be able to apply manufacturing constraints and still converge to an optimal solution. In the previous

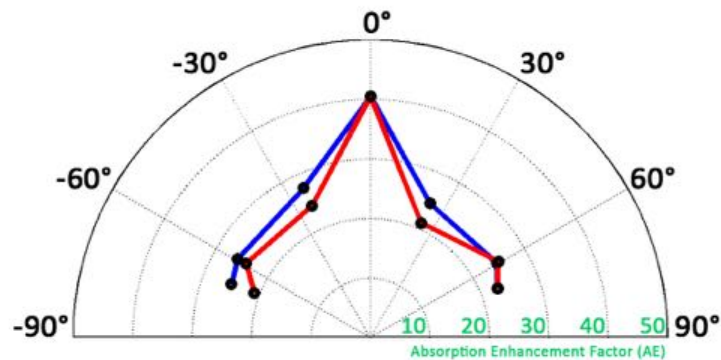


Figure 4.16: The absorption enhancement factor (AE) averaged over frequency and polarization, as a function of incident angle  $\theta$  in the  $xz$  plane (blue) and the  $yz$  plane (red).

calculations, we permitted the texture height amplitude to go from 0 nm to 223 nm, however this would cause difficulties in creating electrical contacts in a real solar cell. In this section, we constrain the texture amplitude to 123 nm, which is much more realistic. The optimization setup is shown in Fig. 4.32, this setup is identical to Fig. 4.1 except for the constraint on the texture height amplitude.

The result from a constrained height amplitude optimization is shown in Figs. 4.33, 4.34, and 4.35. For this texture, we have  $AE = 23$ , which is comparable to the textures without a height amplitude constraint.

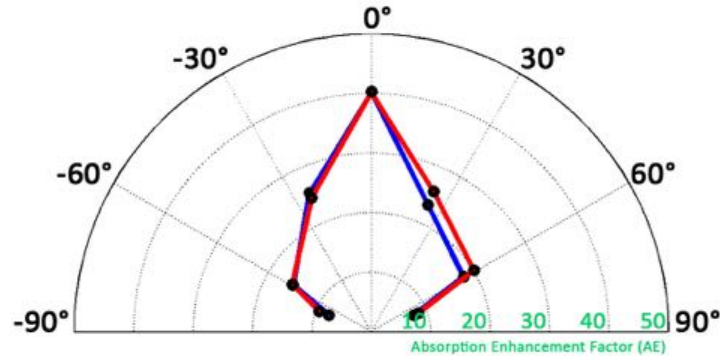


Figure 4.17: The absorption enhancement factor (AE) averaged over frequency and polarization, as a function of incident angle  $\theta$  in the  $xz$  plane (blue) and the  $yz$  plane (red).

## 4.5 Chapter Summary

In the ray optics regime, random structures are optimal for achieving absorption enhancement [13]. In the subwavelength regime, it appears that computationally optimized surface textures perform better than randomly generated ones. We have discovered a broad optimum, with many textures achieving similar figures of merit. This broad optimum means that even when manufacturing constraints are applied, we can find an optimal solution. We have shown that our optimized structures perform about  $1.3\times$  better than randomly generated structures for angle- and frequency-averaged absorption. We report an angle- and frequency-averaged absorption enhancement factor in the weakly absorbing limit of  $E = 39$ , for a texture on a high index material of subwavelength thickness. This enhancement is  $\approx 80\%$  of the ray optics limit  $E = 4n^2 \approx 50$ .

Though we do not prove a fundamental limit, the absorption enhancement factor arising from these optimizations is less than the ray-optics limit. It should be noted that for practical purposes, meeting or exceeding the ray-optics limit in the subwavelength might be unnecessary. For example, starting from a  $1\ \mu\text{m}$  film thickness, which for some materials makes a good solar cell even without light-trapping, an enhancement factor  $E = 50$  would permit a reduced film thickness of 20 nm which is almost too thin for manufacturing purposes. A more reasonable 100 nm solar cell thickness requires an enhancement  $E \approx 10$ , which is easily achieved.

In evaluating the performance of a solar cell texture for light trapping, it is important

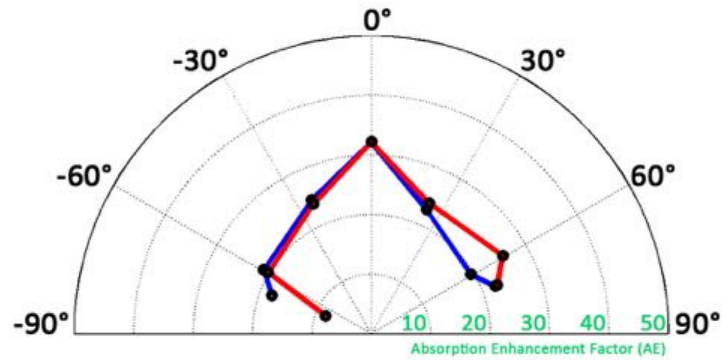


Figure 4.18: The absorption enhancement factor (AE) averaged over frequency and polarization, as a function of incident angle  $\theta$  in the  $xz$  plane (blue) and the  $yz$  plane (red).

to take into account both the average performance, as well as the worst performance over frequency. A texture with a few resonant peaks may yield a high average performance in theory, but when applied to a real material, the resonant peaks will saturate at 100% absorption, and the total photons absorbed will be low. This electromagnetic optimization procedure obtains both a broadband absorption spectrum and a high average absorption.

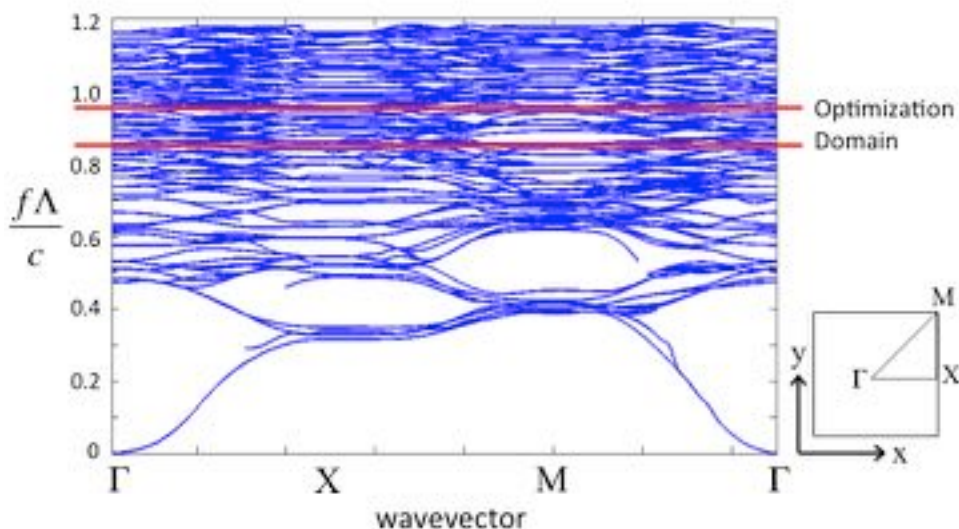


Figure 4.19: The photonic bandstructure for the texture in Fig. 4.15(b).

 Table 4.1: Absorption enhancement factor ( $AE$ ) results.

	Best Optimized Texture	Median Random Texture ( $\Lambda = 710$ nm)	Median Random Supercell Texture ( $\Lambda = 2300$ nm)	Ray Optics Limit
Figure of Merit (worst enhancement factor over frequency and polarization at normal incidence)	29	13	13	
Angle- and Frequency-Averaged Enhancement Factor	24	18	19	28

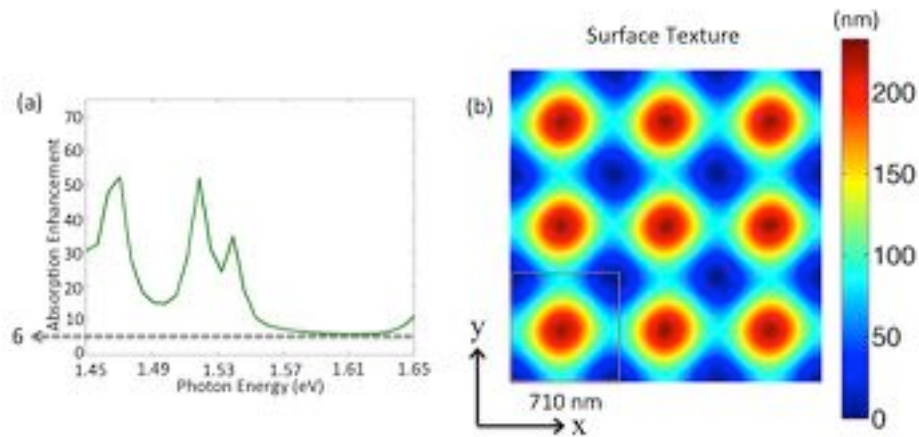


Figure 4.20: (a) The initial absorption enhancement as a function of frequency and (b) a top-down view of the surface texture, for a symmetric texture with a slight perturbation along the diagonal.

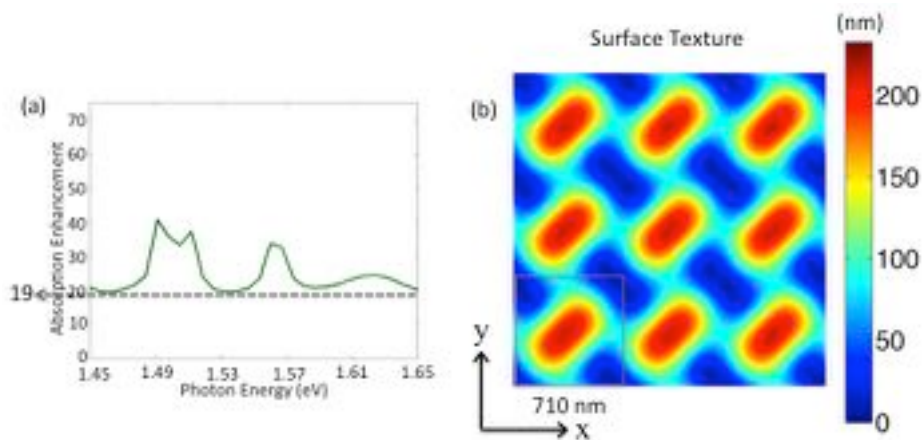


Figure 4.21: (a) The final absorption enhancement as a function of frequency and (b) a top-down view of the surface texture, showing broken mirror symmetry, from almost symmetric initial conditions seen in Fig. 4.20.

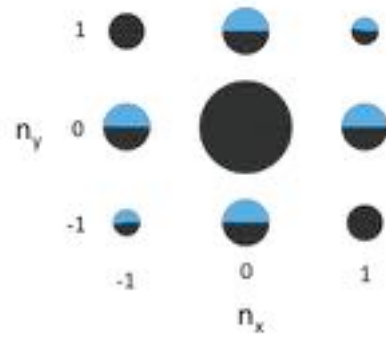


Figure 4.22: The reciprocal space representation for the texture with broken mirror symmetry in Fig. 4.21. The blue pie slices represent the phase of the complex exponential Fourier coefficients.

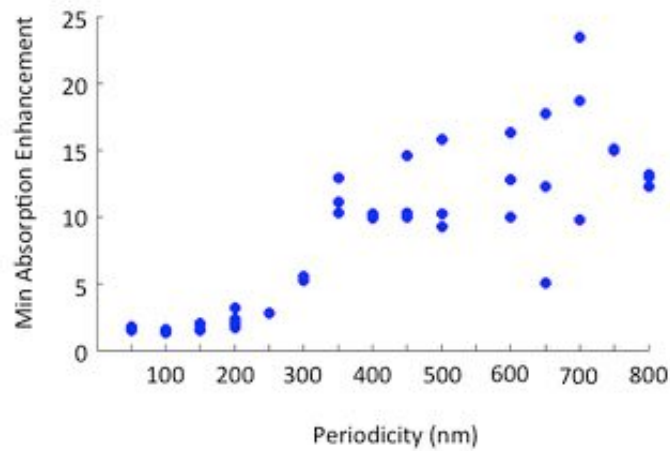


Figure 4.23: Optimizations were carried out at periodicities from 50 to 800 nm, in increments of 50 nm. For each periodicity, at least 3 optimizations were completed for randomly chosen initial starting noise. The Figure of Merit (absorption enhancement for the worst performing frequency and polarization at normal incidence) is plotted for each optimization.

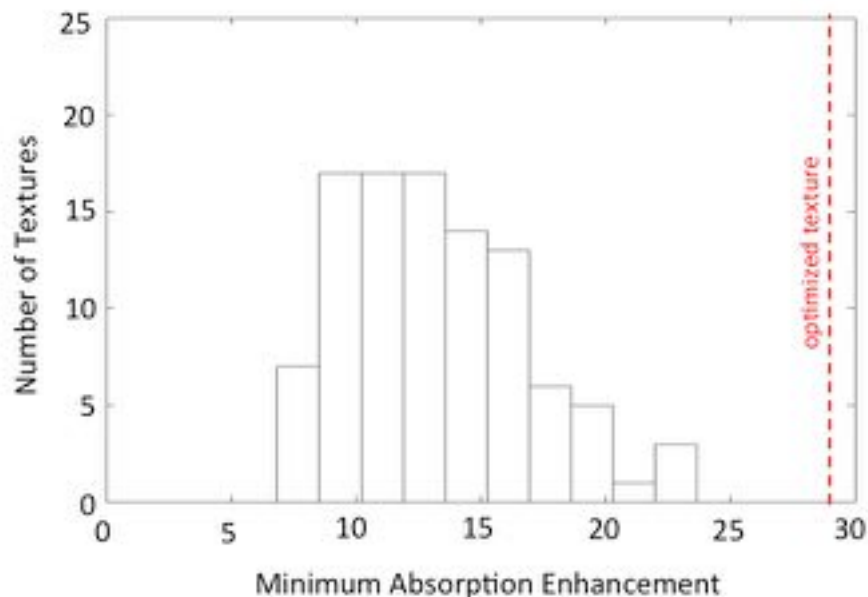


Figure 4.24: The Figure of Merit (minimum absorption enhancement at normal incidence) plotted for 100 randomly generated textures of 710 nm periodicity. For comparison, the Figure of Merit for the optimized texture in Fig. 4.15(b) is shown by the dotted red line.

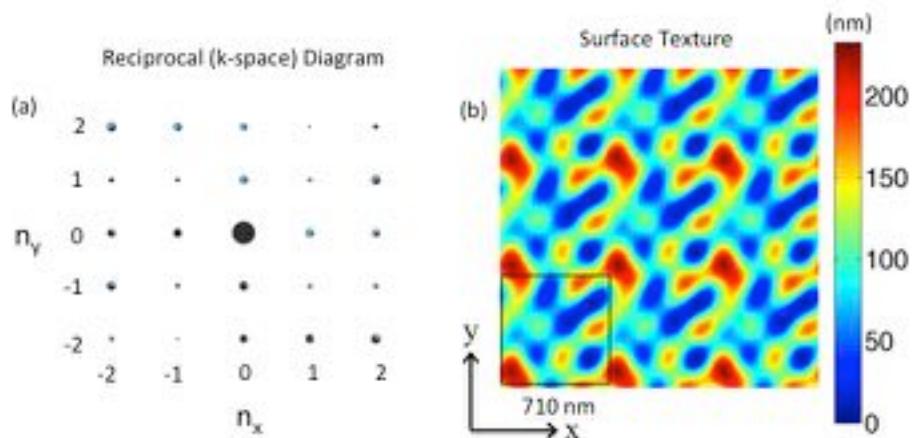


Figure 4.25: The (a) reciprocal k-space diagram and (b) real-space top down view of the median randomly generated texture from Fig. 4.24.

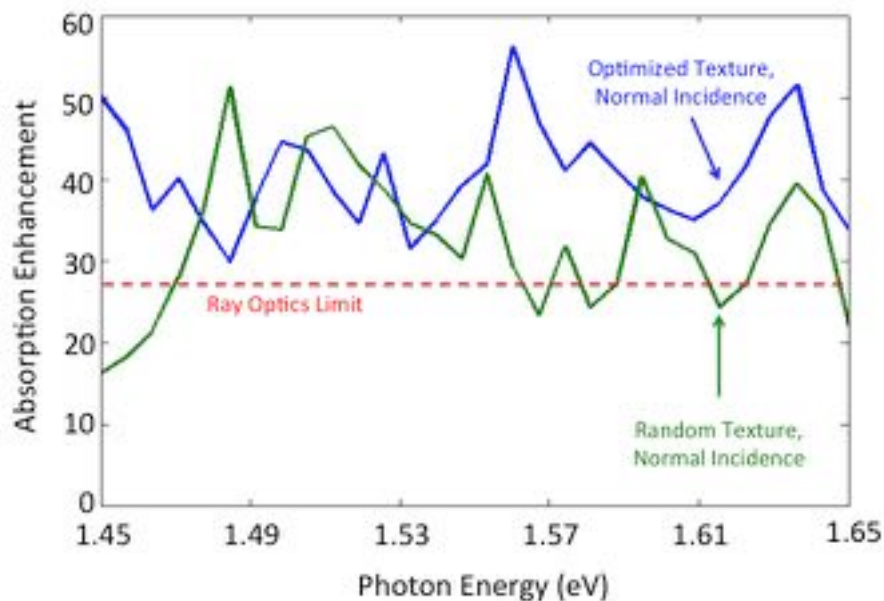


Figure 4.26: The absorption enhancement as a function of frequency at normal incidence for the optimized texture from Fig. 4.15(b) (blue) compared with the median random texture from Fig. 4.25 (green). Lines are averaged over the two orthogonal polarizations.

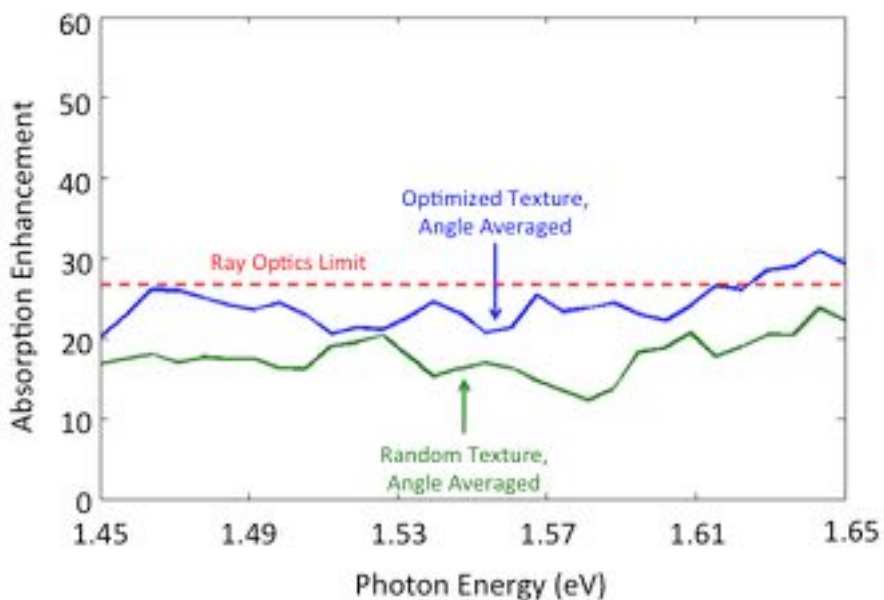


Figure 4.27: The absorption enhancement as a function of frequency, angle averaged, for the optimized texture from Fig. 4.15(b) (blue) compared with the median random texture from Fig. 4.25 (green).

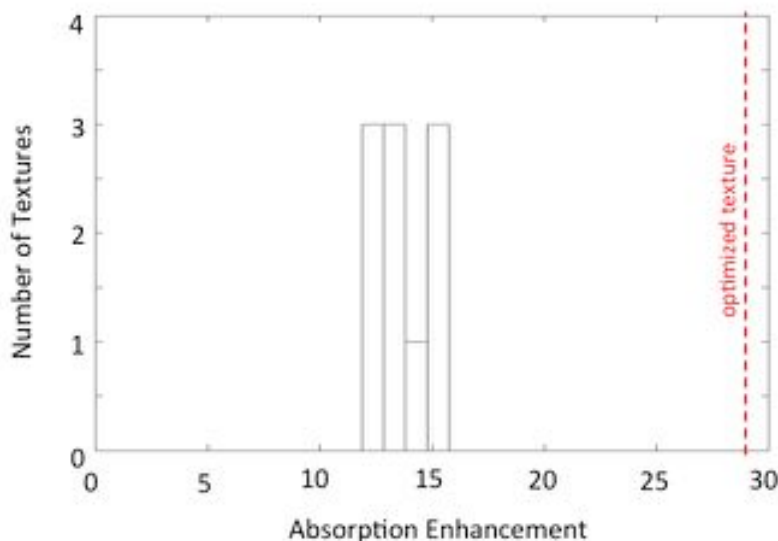


Figure 4.28: The Figure of Merit (minimum absorption enhancement at normal incidence) plotted for 11 randomly generated textures of 2300 nm periodicity. For comparison, the Figure of Merit for the optimized texture in Fig. 4.15(b) is shown by the dotted red line.

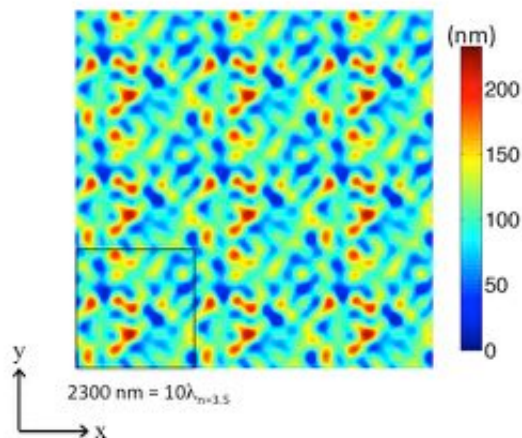


Figure 4.29: A top-down view of the surface texture, for the randomly generated texture with periodicity of  $2300 \text{ nm} = 10\lambda_n = 3.5$ , with median Figure of Merit (minimum absorption enhancement).

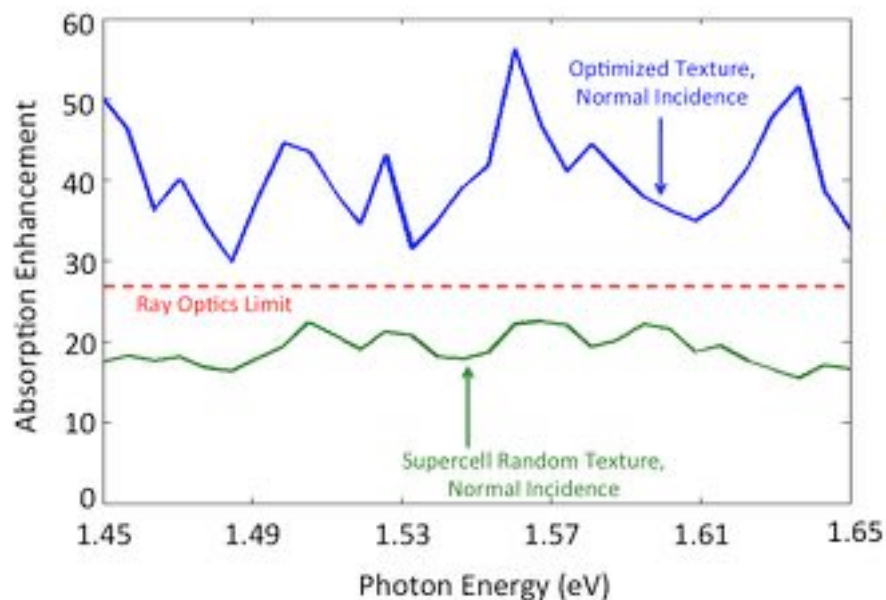


Figure 4.30: The absorption enhancement as a function of frequency at normal incidence for the optimized texture from Fig. 4.15(b) (blue) compared with the median random texture with 2300 nm periodicity from Fig. 4.29 (green). Lines are averaged over the two orthogonal polarizations.

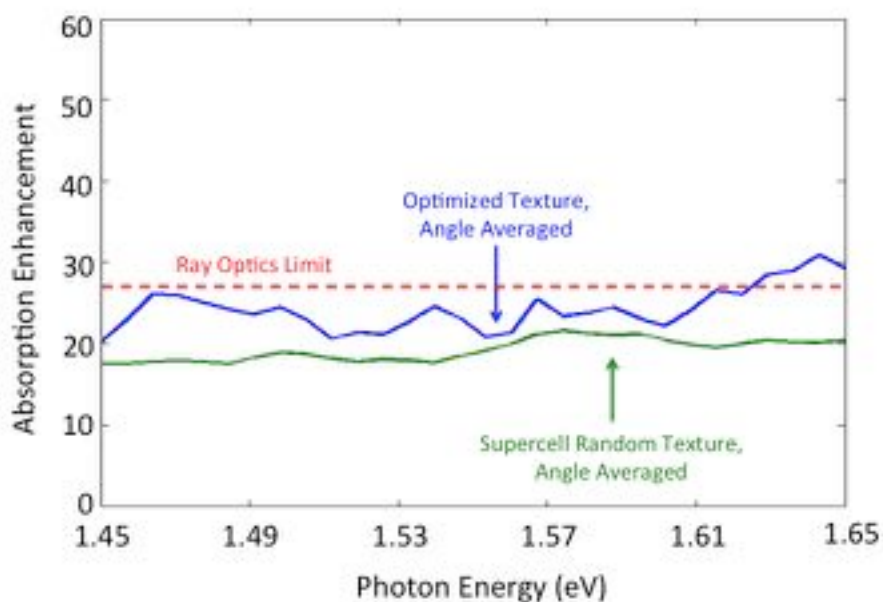


Figure 4.31: The absorption enhancement as a function of frequency, angle averaged, for the optimized texture from Fig. 4.15(b) (blue) compared with the median random texture with 2300 nm periodicity from Fig. 4.29 (green).

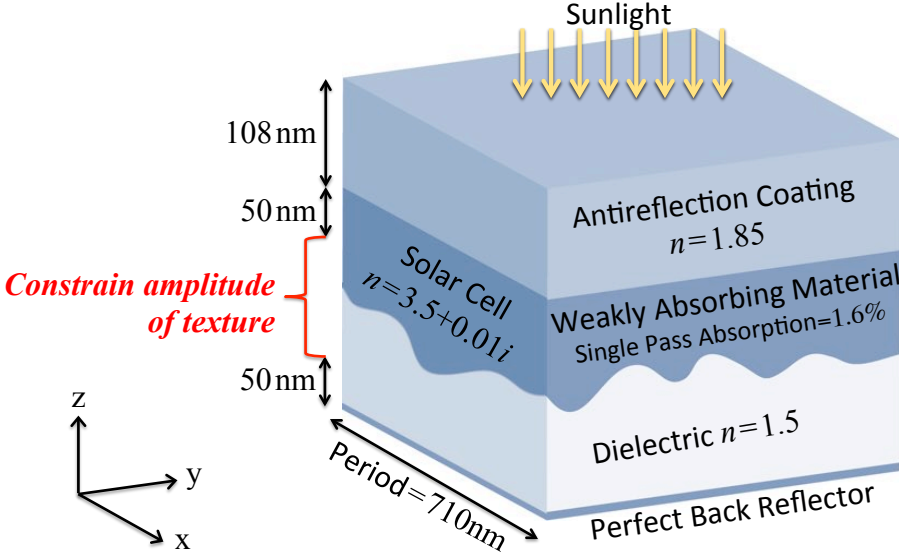


Figure 4.32: Setup for texture optimization with a height amplitude constraint.

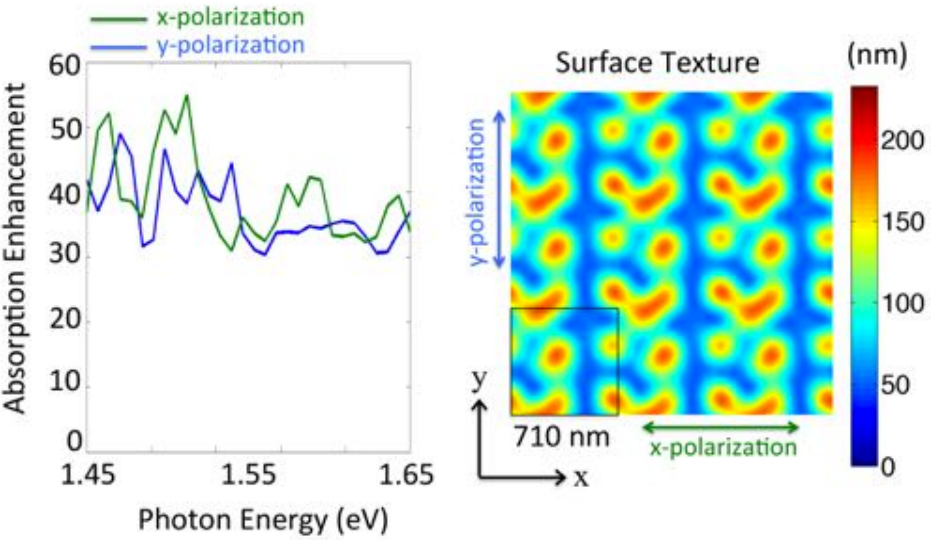


Figure 4.33: Final texture for the optimization with a height amplitude constraint and absorption enhancement for normal incidence light.

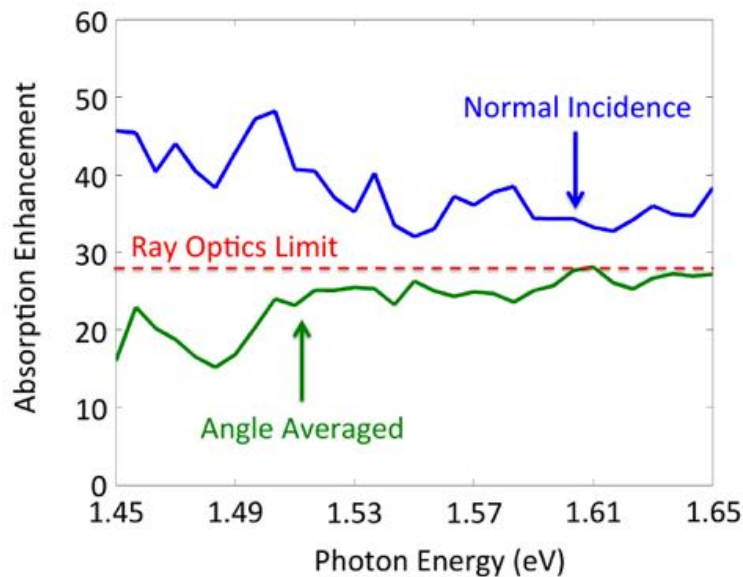


Figure 4.34: Angle averaged and normal incidence performance for the constrained height texture in Fig. 4.33.

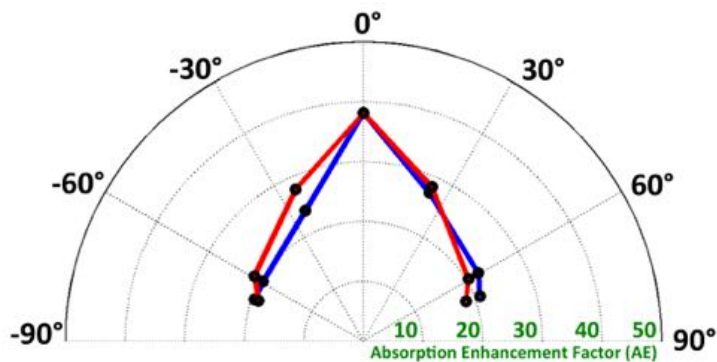


Figure 4.35: The absorption enhancement factor (AE) averaged over frequency and polarization, as a function of incident angle  $\theta$  in the  $xz$  plane (blue) and the  $yz$  plane (red) for the texture in Fig. 4.33.

## Chapter 5

# Thermophotovoltaics with the Photovoltaic Cell as the Spectral Filter

Thermophotovoltaics differ from solar photovoltaics as they convert thermal radiation from local hot sources around  $1200^{\circ}\text{C}$  to  $1500^{\circ}\text{C}$  to electricity, as opposed to converting radiation from the sun (an approximate blackbody at  $5600^{\circ}\text{C}$ ,  $1.5 \times 10^8$  km away from the Earth) to electricity. Due to the lower source temperatures in thermophotovoltaics, the main requirement for high efficiency is spectral filtering of the thermal radiation, so that the substantial amount of photons below the bandgap are reflected back to the hot source, and are not lost. We show that the back mirror of the record-breaking GaAs solar cell from Alta Devices serendipitously had the benefit of having unprecedented sub-bandgap photon reflectivity. The ability to create such a back mirror creates an opportunity for high efficiency in thermophotovoltaics, as the photovoltaic cell itself can act as the spectral filter, absorbing all the above bandgap photons and reflecting the below bandgap photons back to the hot source. In this chapter, we show robust pathways to  $> 50\%$  efficient heat to electricity conversion with thermophotovoltaics.

The hot source for thermophotovoltaics can be generated from combustion of fuel [74], concentrated sunlight [75], or a nuclear power source [76]. Photons radiate from the hot source, with the radiation spectrum depending on the temperature and material properties. As these sources are generally much cooler than the sun, the emitted thermal radiation will be mainly composed of very low energy photons, unusable by a photovoltaic cell. In order to efficiently convert from heat to electricity, low bandgap photovoltaic cells are needed, as well as a spectral filter to recycle the very low energy photons back to the source. Ideally, the spectral filter needs to allow above bandgap photons to be absorbed by the photovoltaic cell, while reflecting the below bandgap photons back to the source. The source itself can be in the spectral filter; in this case low emissivity of certain photon energies is analogous to having a high reflectivity of those photons back to the source. The emissivity spectrum needs to match the absorptivity spectrum of the photovoltaic cell.

The idea of thermophotovoltaics was established in 1956 [77], though at this point in time, photovoltaic cells, especially low bandgap cells, were too inefficient for the idea to take off. There was a re-emergence of interest in thermophotovoltaics in the 1990s, as III-V low bandgap cells such as GaSb emerged [74]. In the 2000s, efforts began to design a photonic crystal to be a selective hot emitter [78]. The photonic crystal would be engineered to suppress emission of the photons with energy below the photovoltaic bandgap, while allowing emission for photons with energy above the bandgap. Designing a photonic crystal with emissivity matching the absorptivity of the photovoltaic cell is a difficult challenge; in a recent effort with optimizing a 2D photonic crystal, the emissivity of below bandgap photons in a tantalum 2D photonic crystal emitter was 30% in simulation (analogous to 70% reflectivity of sub-bandgap photons) [79]. The photonic crystal also needs to be reliable at high temperatures, which is difficult for a structure that contains nano- and micro-structures. It has also been proposed to use a bulk refractory metal such as titanium nitride (TiN) for the hot source [80], but TiN has still has emissivity of 30% for low energy infrared photons [81].

It was recognized many years ago that the semiconductor band-edge itself could provide excellent spectral filtering for thermophotovoltaics, providing that the unused below bandgap radiation can be efficiently reflected back to the heat source [82]. The photovoltaic cell itself is the perfect filter, as all the above bandgap photons are absorbed, and all the below bandgap photons are transmitted to the back mirror of the cell, and get reflected back to the hot source. It is desirable to match the emissivity of the source to the semiconductor band-edge of the photovoltaic cell, i.e. we want a step function from low emissivity to high emissivity at the semiconductor band-edge. For a spectrally selective source, this is a large challenge. On the other hand, when using the photovoltaic cell with a back mirror as the spectral filter, we automatically get band-edge alignment. Additionally, the required spectral selectivity can be provided on the cold photovoltaic cell side, rather than on the hot radiant source side. Fig. 5 schematically shows the difference between using a selective emitter, such as a photonic crystal, for the spectral filter, and using the photovoltaic cell itself as the spectral filter.

Using the photovoltaic cell as the spectral filter puts a burden on the infrared reflectivity of photovoltaic cells toward their unused radiation. In the past, this unusable radiation has been ignored, and the infrared reflectivity of conventional solar cells is typically only 60%. A new breakthrough in record-breaking efficient thin-film solar cells has changed the situation. The current 28.8% single-junction solar efficiency record, by Alta Devices, was achieved in by recognizing that a good solar cell needs to have high back mirror reflectivity to allow internal luminescence to escape from the front surface of the cell [5]. At the maximum power point of a solar cell, a small percentage of photons are absorbed and not collected as current, but instead re-emitted internally in the cell. In order to obtain a high cell voltage, these re-emitted internal photons, which can be re-emitted with energies below the band-edge, must make it out of the front surface of the solar cell [5]. Thus it is important to have high back reflectivity of internal infrared band-edge radiation, to effectively recycle them out the front surface [5]. For high back reflectivity, it is essential to remove the original semiconductor

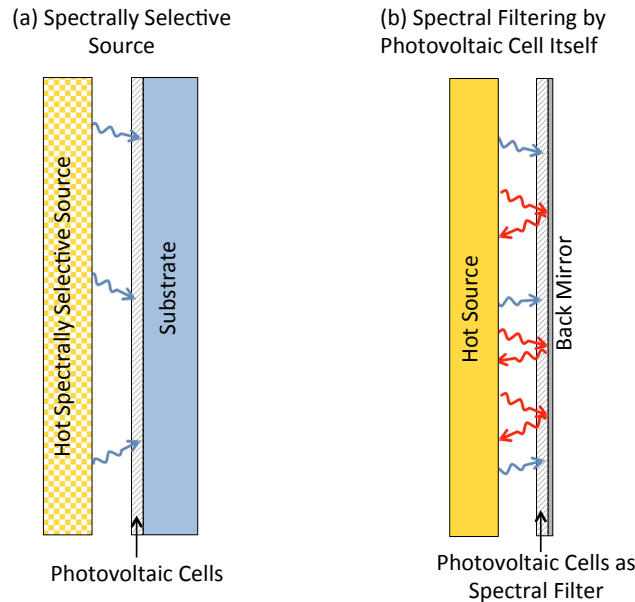


Figure 5.1: For high efficiency, below bandgap photons need to be recycled back to the hot source. This is done with either (a) a spectrally selective source, such as a photonic crystal, which exhibits low emissivity of below bandgap photons (low emissivity of photons is analogous to high reflectivity of photons back to the source) or (b) with a mirror on the back of the photovoltaic cells which reflects the infrared photons back to the source.

substrate, which absorbs infrared luminescence, and to replace it with a high reflectivity mirror, that reflects the luminescent photons and allows them to escape the front surface of the solar cell. The solar cell efficiency record crept up as the back reflectivity behind the photovoltaic film was increased, from 96% reflectivity, to 97%, to finally 98% luminescent reflectivity; each produced a new world efficiency record [4]. The effort to reflect band-edge luminescence in solar cells has serendipitously created the technology to reflect all infrared wavelengths, which can revolutionize thermophotovoltaics. Fig. 5 shows the reflectance as a function of wavelength, for a standard production Alta Devices Gallium Arsenide (GaAs) solar cell. The high back reflectivity is  $> 92\%$  for the sub-bandgap radiation, and we see a clear step function at the bandgap of  $\sim 870$  nm.

For a photovoltaic cell to act as the selective filter itself in thermophotovoltaics, the cell must have a back mirror. For record-breaking GaAs cells, Alta Devices epitaxially grows a film of GaAs on a substrate, with the film separated from the substrate by a thin sacrificial layer of Aluminum Arsenide (AlAs). The AlAs sacrificial layer is then chemically etched, and the film can be lifted off the substrate [10], [83]. This epitaxial lift-off procedure is

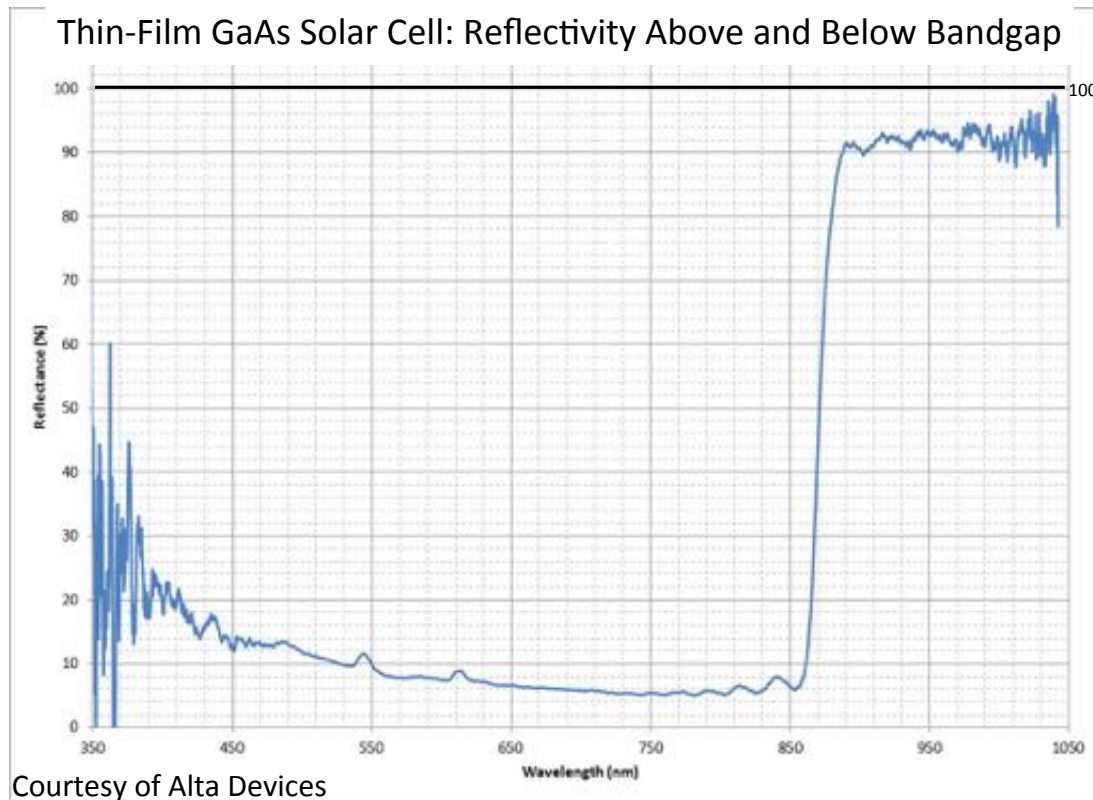


Figure 5.2: Reflectivity of a standard production GaAs solar cell from Alta Devices Inc. (The world record cell had even higher sub-bandgap reflectivity, 98%.) Achieving the same step function response, in an InGaAs alloy, would be ideal for thermophotovoltaics.

crucial to achieving high back mirror reflectivity, as it allows the substrate to be replaced by a back mirror.

The principle of using the photovoltaic cell as the spectral filter for thermophotovoltaics was demonstrated by Ref. [84] in 1978, with a silicon solar cell and a hot source at  $2000^{\circ}\text{C}$  degrees, achieving thermophotovoltaic efficiency of 26%. Both silicon and GaAs photovoltaic cells are well-developed technologies with high efficiencies achieved under sunlight. The problem with GaAs and Silicon cells is that they have bandgaps that are too large (1.4 eV and 1.1 eV, respectively) for cooler source temperatures of  $1200^{\circ}\text{C}$  to  $1500^{\circ}\text{C}$  desirable for thermophotovoltaic systems. It is thus desirable to fabricate epitaxially lifted off low bandgap cells for thermophotovoltaics. Preliminary results for epitaxially lifted off InGaAs cells with a bandgap of 0.74 eV have solar efficiency up to 7.4% [85].

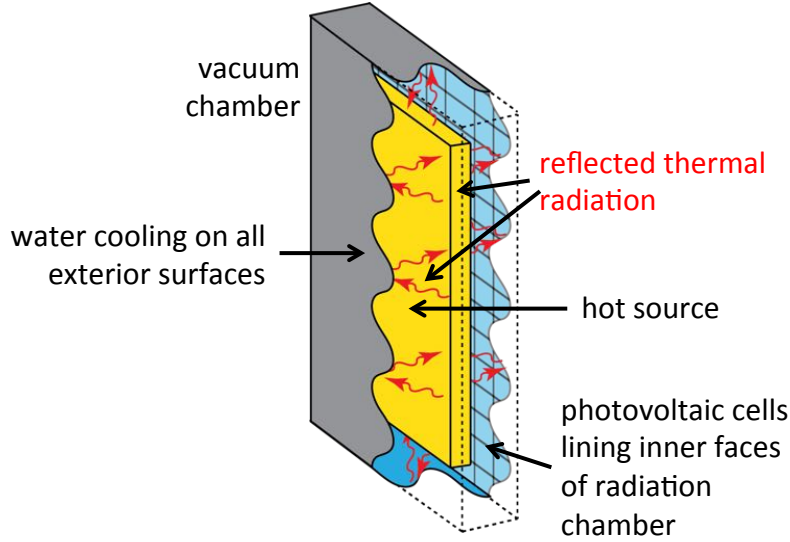


Figure 5.3: Perspective view of the thermophotovoltaic chamber.

## 5.1 Theory

We analyze a thermophotovoltaic system, as diagrammed in Figs. 5.1 and 5.1. A hot radiation source is enclosed by a cavity, the thermophotovoltaic chamber. Photovoltaic cells line the largest 2 inner faces of a thin rectangular cavity and are plane parallel to a hot radiation source. The other 4 inner faces of the cavity are lined with reflective mirrors. The inside of the cavity is under vacuum, and the hot radiation source emits thermal radiation as a blackbody at temperature  $T_{source} = T_s$ . There is water cooling on all the outside surfaces of the thermophotovoltaic chamber, maintaining the solar cells at a temperature  $T_{cell} = T_c$ . The photovoltaic cells have back mirrors with reflectivity as a function of photon energy. We denote the reflected sub-bandgap photons with red arrows.

We follow the formulation for solar cell efficiency, given in Refs. [5], [6], and detailed in Chapters 2 and 3, to derive the efficiency equation for thermophotovoltaics. The blackbody radiation from the hot radiation source incident on the cold photovoltaic cells is given as (averaged over flat plate, ignoring end effects):

$$b_s(E) = \frac{2\pi E^2}{c^2 h^3 \left( \exp\left(\frac{E}{k_B T_s}\right) - 1 \right)}, \quad (5.1)$$

where  $b_s(E)$  is the blackbody radiation in units of photons/time/area/energy,  $E$  is the

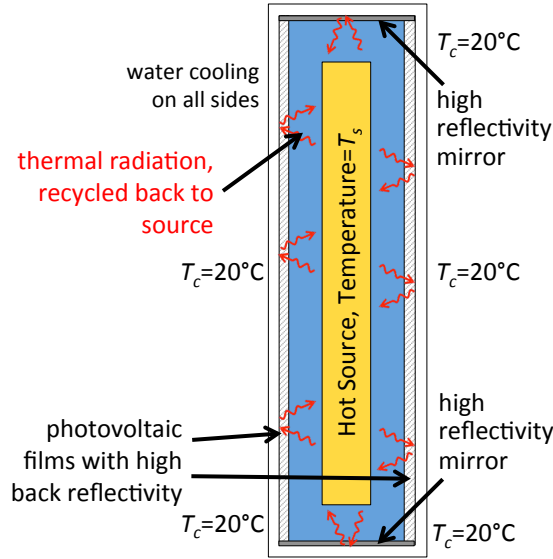


Figure 5.4: Cross-sectional view of the thermophotovoltaic chamber.

photon energy,  $c$  is the speed of light,  $h$  is Planck's constant,  $k_B$  is the Boltzmann constant, and  $T_s$  is the temperature of the hot radiation source.

We assume the photovoltaic cells have step function absorption, absorbing all photon energies above the bandgap,  $E_g$ . The short circuit current density of the cells,  $J_{sc}$ , is given by:

$$J_{sc}c = q \int_0^\infty A(E)b_s(E)dE = q \int_{E_g}^\infty b_s(E)dE, \quad (5.2)$$

where  $q$  is the charge of an electron and  $A(E)$  is the absorption as a function of photon energy. As we assume step function absorption, the equation simplifies to the expression on the right.

In the dark, the photovoltaic cells emit blackbody radiation at temperature  $T_c$ . The radiation emitted from the cells in the dark, similar to Eqn. (5.1), is given as:

$$b_c(E) = \frac{2\pi E^2}{c^2 h^3 \left( \exp\left(\frac{E}{k_B T_c}\right) - 1 \right)}, \quad (5.3)$$

where  $b_c(E)$  is the blackbody radiation from the photovoltaic cells in units of photons/time/area/energy. The cells have some external fluorescence yield of  $\eta_{ext}$  (defined here,

as in Ref. [5] as the ratio of radiative recombination out the front surface of the cell to the total recombination). The dark saturation current density  $J_0$  is thus given by:

$$J_0 = \frac{q}{\eta_{ext}} \int_0^\infty A(E)b_c(E)dE = \frac{q}{\eta_{ext}} \int_{E_g}^\infty b_c(E)dE. \quad (5.4)$$

The current-voltage relationship for a photovoltaic cell is similar to Eqn. (7) in Ref. [5], and is given as:

$$J(V) = J_{sc} - J_0 \exp\left(\frac{V}{k_B T_c}\right) = q \int_{E_g}^\infty b_s(E)dE - \frac{q}{\eta_{ext}} \exp\left(\frac{V}{k_B T_c}\right) \int_{E_g}^\infty b_c(E)dE, \quad (5.5)$$

where  $V$  is the voltage of the photovoltaic cell. We assume, in this analysis, perfect carrier collection, i.e. at short circuit, every absorbed photon creates an electron-hole pair that is collected by the contacts.

If we operate the photovoltaic cells at the maximum power point (the voltage  $V_{MPPT}$  at which the output power  $P = J \times V$  is maximized), the output power is denoted as  $J_{MPPT} V_{MPPT}$ , where  $J_{MPPT} = J(V_{MPPT})$ .

The thermophotovoltaic efficiency will be the ratio of output electrical power to input thermal power. The input thermal power is the above bandgap thermal radiation absorbed by the solar cells summed with the below bandgap thermal radiation lost due to imperfect cell reflectivity. The blackbody radiation from the hot source, in units of power/area/energy, is given as:

$$b_{s, \text{power}}(E) = \frac{2\pi E^3}{c^2 h^3 \left(\exp\left(\frac{E}{k_B T_s}\right) - 1\right)}. \quad (5.6)$$

The thermophotovoltaic efficiency  $\eta_{TPV}$  is thus given as:

$$\eta_{TPV} = \frac{J_{MPPT} V_{MPPT}}{\int_0^\infty b_{s, \text{power}}(E)dE - R \int_0^{E_g} b_{s, \text{power}}(E)dE}, \quad (5.7)$$

where  $R$  denotes the reflectivity of the photovoltaic cells to the sub-bandgap photons, modeled as a constant over all the sub-bandgap photon energies in this analysis. Any source of parasitic absorption of sub-bandgap photons, such as free carrier absorption, can be accounted for by penalizing  $R$ . The first term in the denominator is the total blackbody power incident on the cells, and the second term subtracts the power that is reflected back to the hot radiation source.

It should be noted that there is radiative emission out of the front of the cell, with the spectrum  $R_{rad}(E)$  in units of power/area/energy:

$$R_{rad}(E) = A(E) \frac{2\pi E^3}{c^2 h^3 \left(\exp\left(\frac{E-qV}{k_B T_c}\right) - 1\right)}, \quad (5.8)$$

where  $R_{rad}(E)$  is integrated over photon energy  $E$ , we get an additional amount of energy that is recycled back to the hot source. This term is however ignored in this analysis, as when we operate at the maximum power point of the cell, the contribution from this term is negligible.

## 5.2 Efficiency of Single Bandgap Thermophotovoltaics

We plot thermophotovoltaic efficiency  $\eta_{TPV}$  against reflectivity of sub-bandgap photons  $R$  in Figs. 5.2 and 5.2. For each value of  $R$ , we plot the cell bandgap  $E_g$  that maximizes  $\eta_{TPV}$ . In Fig. 5.2, we assume a hot radiation source temperature  $T_s = 1200^\circ C$ , and in Fig. 5.2, we have  $T_s = 1500^\circ C$ . We also assume  $\eta_{ext} = 30\%$  and  $T_c = 20^\circ C$ . By plotting the optimal efficiency as a function of back mirror reflectivity, we show that we can compensate for a poor back mirror by reducing the bandgap of the photovoltaic cell. A poor back mirror means that more of the sub-bandgap photons will be lost. This loss can be ameliorated by moving to a smaller bandgap that will absorb photons that would otherwise be lost. In Figs. 5.2 and 5.2, we mark 50% efficiency by a gray dashed line. For  $T_s = 1200^\circ C$  in Fig. 5.2, we can achieve 50% thermophotovoltaic efficiency with  $R \geq 98\%$ , and for  $T_s = 1500^\circ C$ , 50% efficiency can be achieved with  $R \geq 95\%$ . At  $1200^\circ C$ , a cell of bandgap 0.8eV with  $R=99\%$  can achieve 51% thermophotovoltaic efficiency. At  $1500^\circ C$ , a cell of bandgap 0.95eV with  $R=99\%$  can achieve 59% thermophotovoltaic efficiency.

Fig. 5.2 plots Eqn. (5.6), the blackbody spectrum in terms of power/area/energy. For the bandgap of 0.8 eV at  $1200^\circ C$ , we can integrate over the photon energies above 0.8eV (the region highlighted in blue), to find the power/area that are absorbed by the 0.8eV cell, and we can integrated over the photon energies below 0.8eV (the region highlighted in red) to find the sub-bandgap power/area that need to be reflected back to the source (Fig. 5.2 plots the short circuit current as a function of bandgap). At  $1200^\circ C$  for a 0.8 eV bandgap, there are  $27 \frac{W}{cm^2}$  of black body radiation, of which  $3.2 \frac{W}{cm^2}$  are absorbed, and  $1.56 \frac{W}{cm^2}$  are converted to electricity. Thus  $\sim 24 \frac{W}{cm^2}$  are re-thermalized on each reflection. The large percentage of sub-bandgap power highlights the need for high reflectivity back to the hot source.

## 5.3 Efficiency of Dual Bandgap Thermophotovoltaics

In Figs. 5.3 and 5.3, we plot the thermophotovoltaic efficiency  $\eta_{TPV}$  against reflectivity of sub-bandgap photons for dual bandgap photovoltaic cells. We assume dual bandgap cells that are not connected in series, instead each sub-cell has two terminal connections. We assume a sub-cell of bandgap  $E_{g1}$  stacked on top of a sub-cell with  $E_{g2}$ . The top sub-cell  $E_{g1}$  will absorb all of the above bandgap photons, and the remaining photons will be transmitted to the bottom sub-cell  $E_{g2}$ , which will then absorb all the photons remaining photons that are above its bandgap. We neglect the small amount of luminescence coupling [14] between the cells, and assume  $\eta_{ext} = 30\%$  for both top and bottom sub-cells. In Figs. 5.3 and 5.3, for

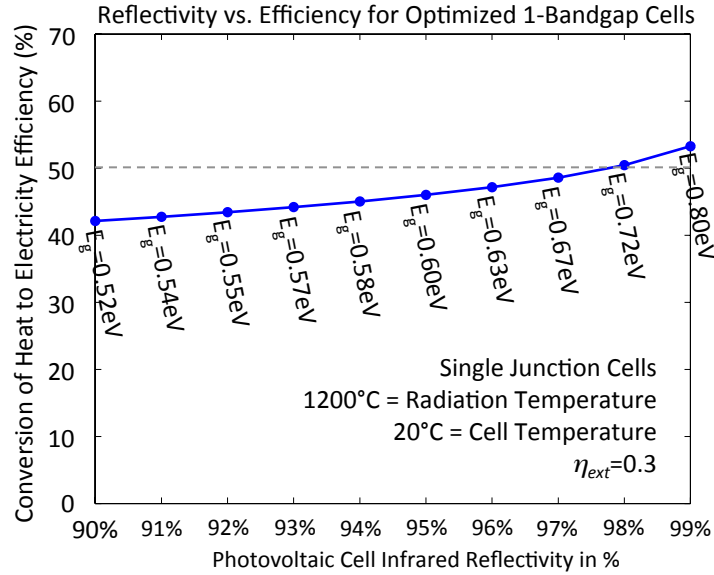


Figure 5.5: The efficiency as a function of photovoltaic cell infrared reflectivity for single junction cells. The source radiation temperature is  $1200^{\circ}\text{C}$ , the cell temperature is  $20^{\circ}\text{C}$ , and  $\eta_{ext} = 0.3$ .

each value of  $R$ , we plot the cell bandgaps  $E_{g1}$  and  $E_{g2}$  that maximize  $\eta_{TPV}$ , with Fig. 5.3 assuming a  $1200^{\circ}\text{C}$  source and Fig. 5.3 assuming a  $1500^{\circ}\text{C}$  source.

## 5.4 Selective Source and Reflective Back Mirror

We see that a reflective mirror on the backside of the photovoltaic cell has great importance to the thermophotovoltaic efficiency. The question arises, can we obtain a dual benefit from using a reflective back mirror *and* a selective source?

Let's say that our selective source has a sub-bandgap reflectivity  $R_s$  (with  $R_{source} = 0$  for above bandgap photons), and the sub-bandgap reflectivity of the photovoltaic cell back mirror is  $R_c$ . A sub-bandgap photon that is emitted from the source is lost from the system with a probability of  $P_{lost}$ , given by the infinite summation:

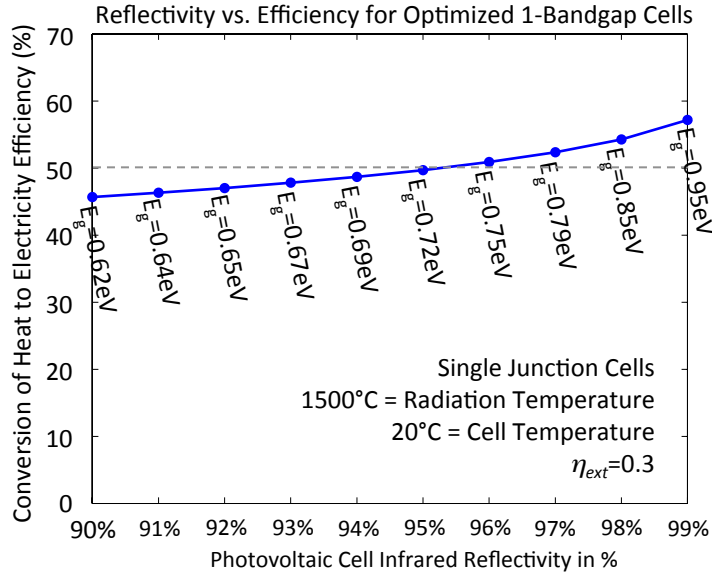


Figure 5.6: The efficiency as a function of photovoltaic cell infrared reflectivity for single junction cells. The source radiation temperature is  $1500^{\circ}\text{C}$ , the cell temperature is  $20^{\circ}\text{C}$ , and  $\eta_{ext} = 0.3$ .

$$\begin{aligned}
 P_{lost} &= (1 - R_c) + R_c R_s (1 - R_c) + R_c R_s R_c R_s (1 - R_c) \dots \\
 &= \sum_{n=0}^{\infty} R_c^n R_s^n (1 - R_c) \\
 &= \frac{1 - R_c}{1 - R_c R_s}.
 \end{aligned} \tag{5.9}$$

We can then re-write  $\eta_{TPV}$  in Eqn. (5.7) as:

$$\eta_{TPV} = \frac{J_{MPPT} V_{MPPT}}{\int_0^{\infty} (1 - R_s(E)) b_{s, \text{power}}(E) dE - (1 - P_{lost})(1 - R_s) \int_0^{E_g} b_{s, \text{power}}(E) dE}. \tag{5.10}$$

We plot Eqn. (5.10) in Fig. 5.4 for a photovoltaic cell with bandgap 0.8 eV and a hot source temperature of  $1200^{\circ}\text{C}$ . We see in Fig. 5.4 that there is no dual benefit from a selective source and a reflective back mirror when either  $R_s$  or  $R_c$  is close to 100%. At this limit, the higher reflectivity dominates.

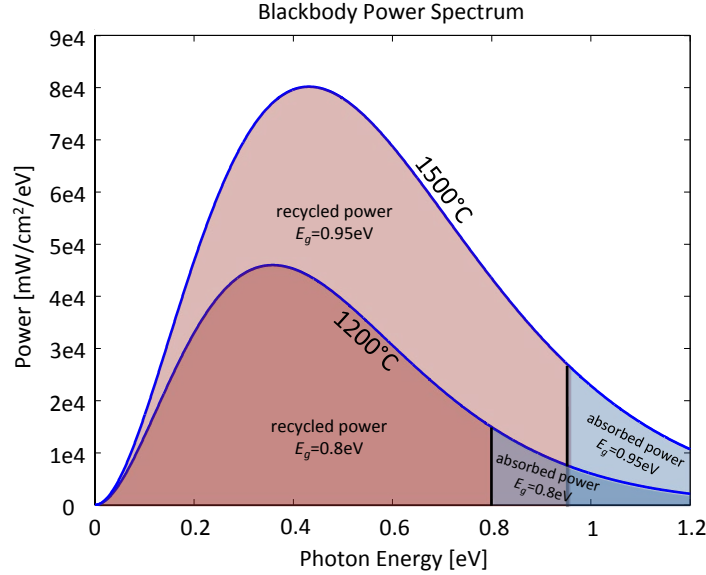


Figure 5.7: The blackbody power spectrum, for blackbody sources at  $1500^\circ\text{C}$  and  $1200^\circ\text{C}$ . For a  $0.8\text{eV}$  bandgap cell and a  $1200^\circ\text{C}$  source, the power absorbed by the solar cell is indicated by the blue region, and the power recycled back to the hot source is indicated by the red region. Similarly for a  $0.95\text{eV}$  bandgap cell and a  $1500^\circ\text{C}$  source, the regions of recycled power and absorbed photon are highlighted in red and blue, respectively.

## 5.5 Reaching Carnot Efficiency

Until now, we've focused on sub-bandgap reflectivity. Even though we match the optimal bandgap to the hot source spectrum, there are still thermalization losses due to absorption of photons that have energy greater than the bandgap. If we could add a filter to the system that reflects high energy photons back to the hot source before they reach the cell, we could eliminate these thermalization losses (however, the output power density would be lower). In Fig. 5.5, we plot the efficiency of a thermophotovoltaic system assuming 100% back reflectivity and  $\eta_{ext} = 100\%$ , as a function of the bandwidth above the bandgap that is transmitted to the cell (blue line). In calculating the efficiency, we used Eqn. 5.7, including the term in Eqn. 5.8, optimizing  $V$  for highest efficiency. In the limit of a small bandwidth, we reach the Carnot efficiency of 80.1%. However, when we drop to 99% reflectivity of sub-bandgap photons, keeping  $\eta_{ext} = 100\%$ , we have the situation illustrated by the red line. The optimal point on the red line is a bandwidth of 0.22 eV, corresponding to an efficiency of 62.3%, compared to 59.5%, the efficiency if none of the above bandgap photons are filtered.

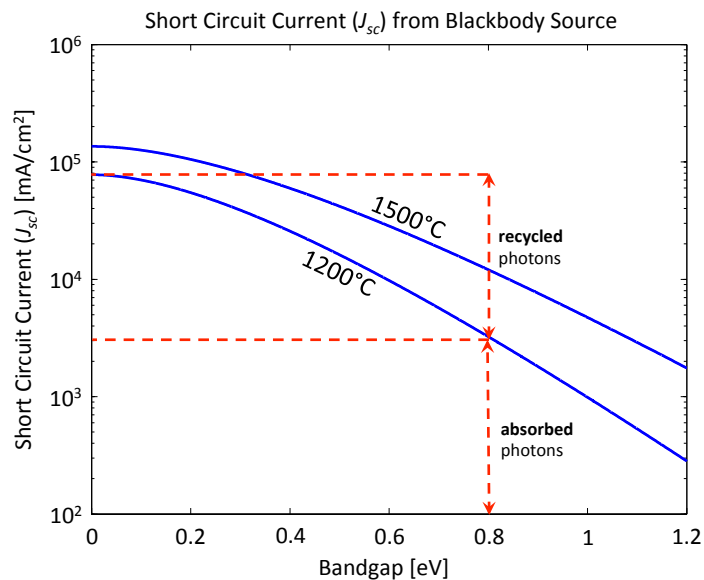


Figure 5.8: The short circuit current ( $J_{sc}$ ) as a function of bandgap, for blackbody sources at  $1500^{\circ}C$  and  $1200^{\circ}C$ . For a  $0.8\text{ eV}$  bandgap cell and a  $1200^{\circ}C$  hot source, 4% of the photons emitted by the blackbody are above bandgap and thus absorbed by the photovoltaic cell, while 96% are recycled back to the hot source, as indicated by the red dashed lines.

In practice, the benefit achieved by filtering the high energy photons may be offset by the added complexity of adding a second filter.

## 5.6 Chapter Summary

Thermophotovoltaics has the potential to be a highly efficient method of heat to electricity conversion, and it is portable and compact, containing no moving parts. The design of a photovoltaic cell back mirror with very high sub-bandgap reflectivity is the path to a high efficiency thermophotovoltaic system. Without special attention to the sub-bandgap photon reflectivity, a standard production Alta Devices solar cell reached  $R > 92\%$ , and the recording breaking GaAs cell had  $98\%$  sub-bandgap photon reflectivity.  $R > 99\%$  is achievable. With a  $1200^{\circ}C$  source, if all photons above  $\sim 0.8\text{ eV}$  can be used, and  $99\%$  of unabsorbed photons below  $\sim 0.8\text{ eV}$  energy can be recycled to the heat source, the conversion from heat to electricity can be  $> 50\%$  efficient.

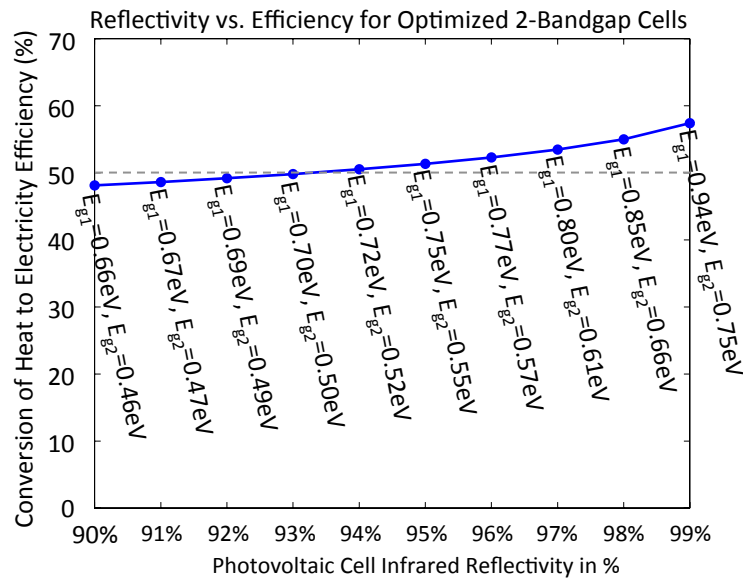


Figure 5.9: The efficiency as a function of photovoltaic cell infrared reflectivity for dual junction cells.  $E_{g1}$  is the bandgap of the top cell in the dual junction stack, and  $E_{g2}$  is the bandgap of the bottom cell. The source radiation temperature is  $1200^{\circ}\text{C}$ , the cell temperature is  $20^{\circ}\text{C}$ , and for both top and bottom cells,  $\eta_{ext} = 0.3$ .

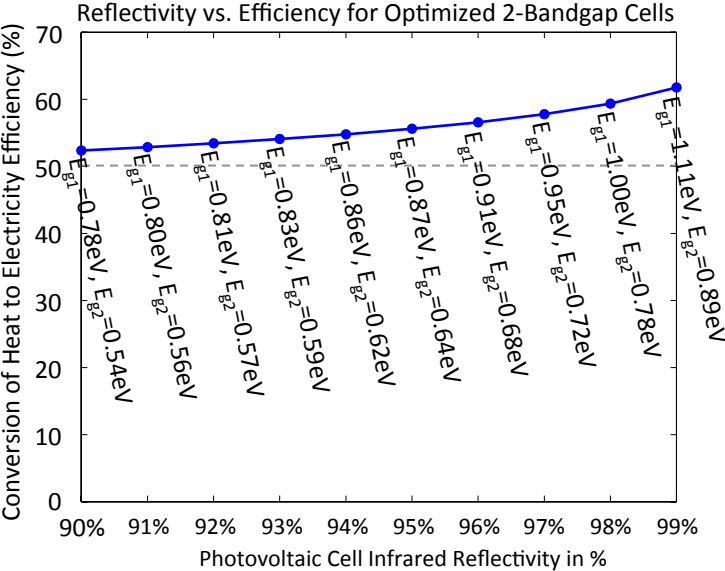


Figure 5.10: The efficiency as a function of photovoltaic cell infrared reflectivity for dual junction cells.  $E_{g1}$  is the bandgap of the top cell in the dual junction stack, and  $E_{g2}$  is the bandgap of the bottom cell. The source radiation temperature is  $1500^{\circ}\text{C}$ , the cell temperature is  $20^{\circ}\text{C}$ , and for both top and bottom cells,  $\eta_{ext} = 0.3$ .

Efficiency for a Selective Source and Reflective Back Mirror

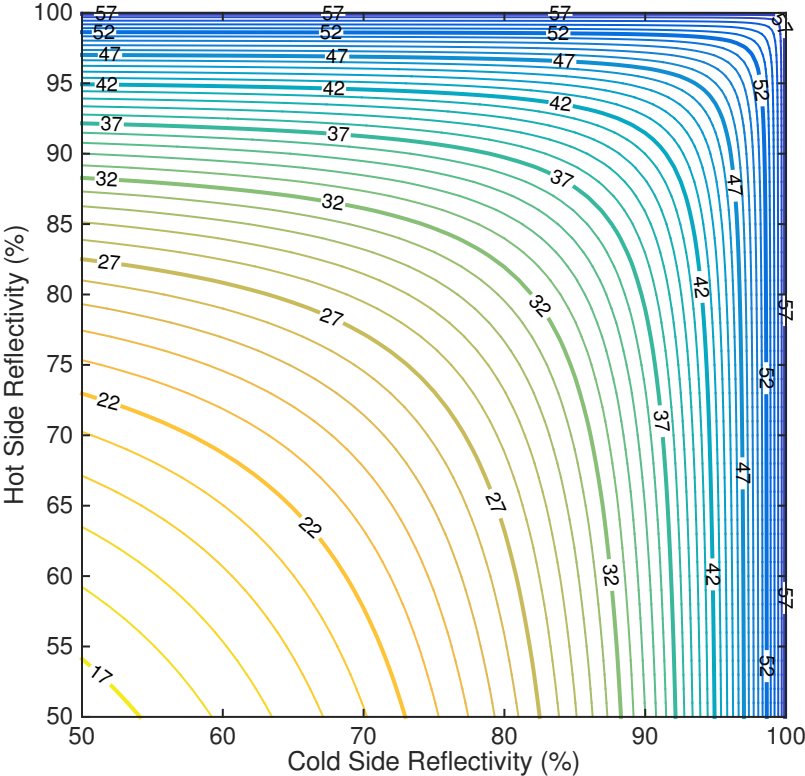


Figure 5.11: The thermophotovoltaic efficiency plotted as a function of the hot source sub-bandgap reflectivity and the cold side sub-bandgap reflectivity for a photovoltaic cell with bandgap 0.8 eV and a hot source temperature of 1200°C.

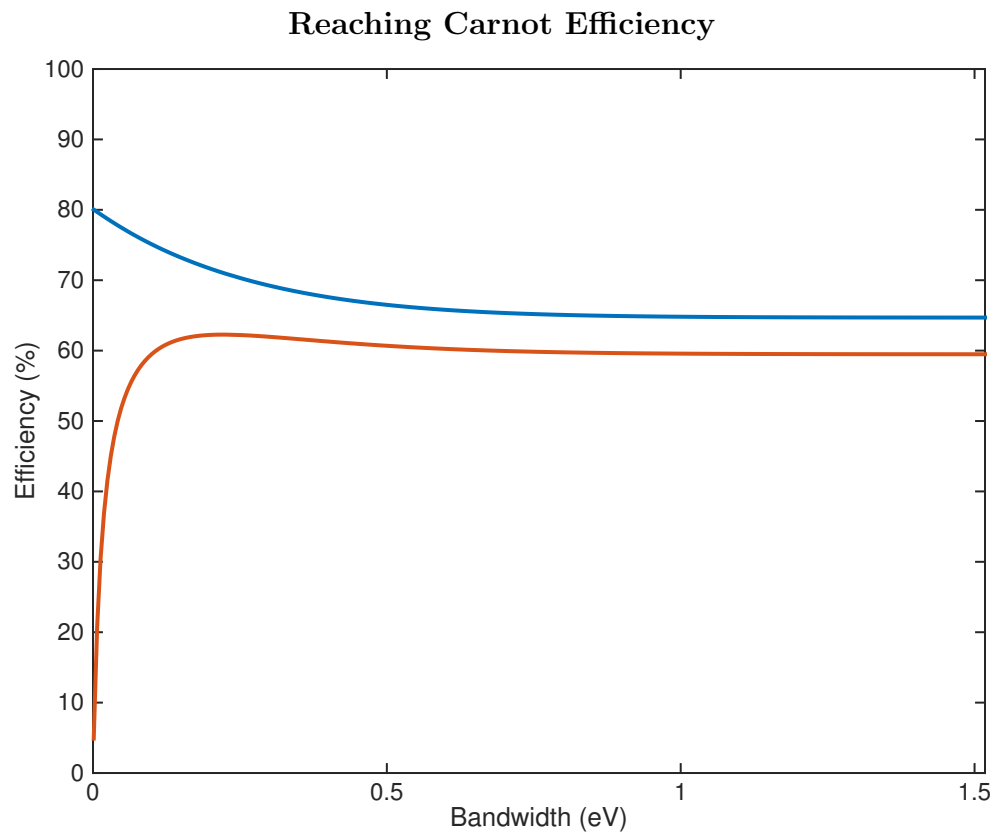


Figure 5.12: The efficiency of a thermophotovoltaic system assuming 100% back reflectivity and  $\eta_{ext} = 100\%$ , as a function of the bandwidth above the bandgap that is transmitted to the cell (blue line) and assuming 99% back reflectivity (red line).

## Chapter 6

# Concentrating Solar Technologies

If sunlight comes directly from the sun to the Earth's surface, without experiencing any scattering, then the light will be within an angular range from  $\theta = 0^\circ$  to  $\theta = 0.27^\circ$ , where  $\theta$  is the angle from the normal to the Earth's surface. We can make use of this fact in 2 ways: (1) limiting the acceptance angle of the solar cell, using a structure that admits light in the angular range of  $\theta = 0^\circ$  to  $\theta = 0.27^\circ$ , but rejects light outside this range, or (2) concentrating the sunlight to the maximum concentration of:

$$C_{max} = \left( \frac{1}{(\sin(0.27^\circ))^2} \right) = 46211. \quad (6.1)$$

Each of these options causes a voltage increase in the cell. This can be seen from the equation for open circuit voltage,  $V_{oc}$ :

$$V_{oc} = \frac{kT}{q} \ln \left( \frac{\int_{E_g}^{\infty} C \times S(E) dE}{\int_0^{\infty} \int_0^{\theta_{max}} b(E) \sin \theta \cos \theta dE} \right) - \frac{kT}{q} \ln \left( \frac{1}{\eta_{ext}} \right), \quad (6.2)$$

where  $\theta_{max}$  is the maximum angle that is admitted into the solar cell and  $C$  is the factor by which the sunlight is concentrated. In option (1),  $\theta_{max} = 0.27^\circ$  and  $C = 1$ . In option (2),  $\theta_{max} = \frac{\pi}{2}$  and  $C = 46211$ . Both options yield an open-circuit voltage increase of  $\frac{kT}{q} \ln(46211) \approx 270$  mV at an ambient temperature of  $20^\circ\text{C}$ . Though the approaches differ practically, they have identical limiting efficiencies. In this chapter, when we refer to sunlight concentration, it will refer to either option (1) or option (2).

This voltage boost, and correspondingly, the efficiency increase due to concentration is tantalizing. However, the solar cell won't be able to absorb the diffuse radiation that has been scattered from the atmosphere (which can be a significant fraction depending on location), and there must be a tracking mechanism for the solar cell to track the position of the sun in the sky. In this chapter, we use the Direct+Circumsolar spectrum from the National Renewable Energy Laboratory [26], and ignore the diffuse radiation when calculating efficiency. This approach is limited, but will allow us to compare between concentrating technologies (but not compare a concentrating solar technology to an unconcentrating one).

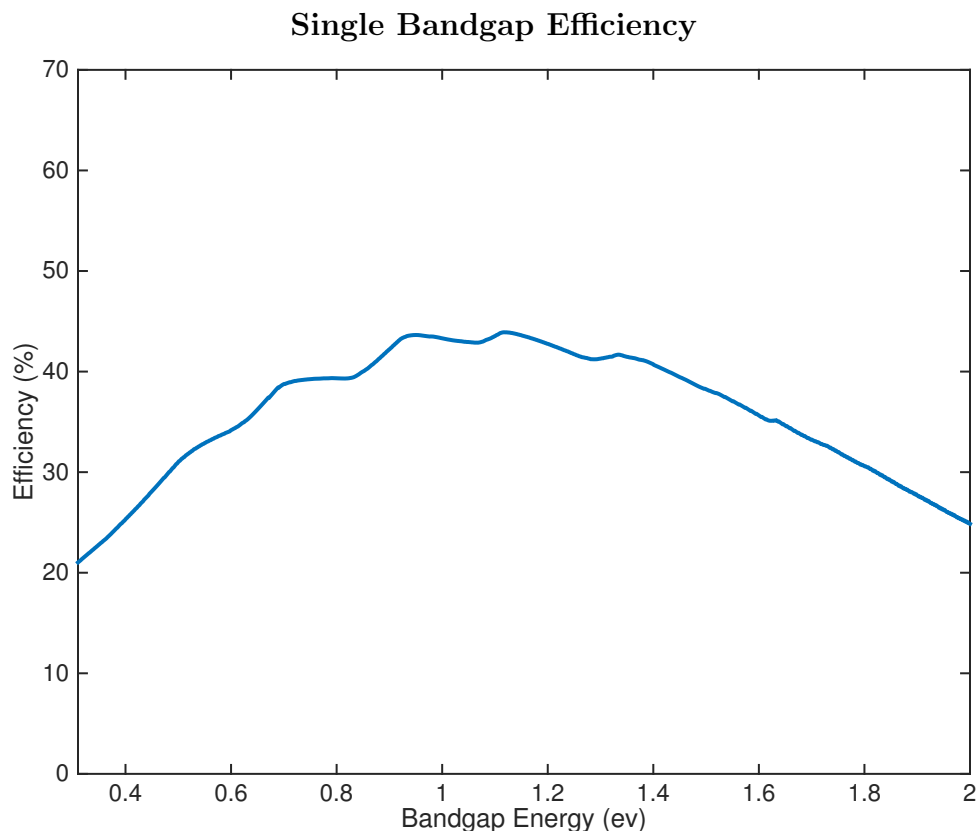


Figure 6.1: Efficiency of single bandgap solar cells under maximum concentration.

## 6.1 Single Bandgap Cells Under Concentration

We first calculate the efficiency of a single bandgap cell under concentration, see Fig. 6.1. We use the procedure illustrated in Chapter 2, assuming maximum concentration factor of 46211 and  $\eta_{ext} = 0.3$ . The best efficiency is 43.9% with an optimal bandgap of 1.12 eV.

## 6.2 Dual Bandgap Cells Under Concentration

We now calculate the efficiency for dual bandgap cells under concentration, see Fig. 6.2. We assume  $\eta_{ext} = 0.3$  for both the top and bottom sub-cells. The highest efficiency achieved is 60.3%, with bandgaps of  $E_{g1} = 1.52$  eV and  $E_{g2} = 0.70$  eV. As expected, the limiting efficiency with two bandgaps is greater than with one bandgap.

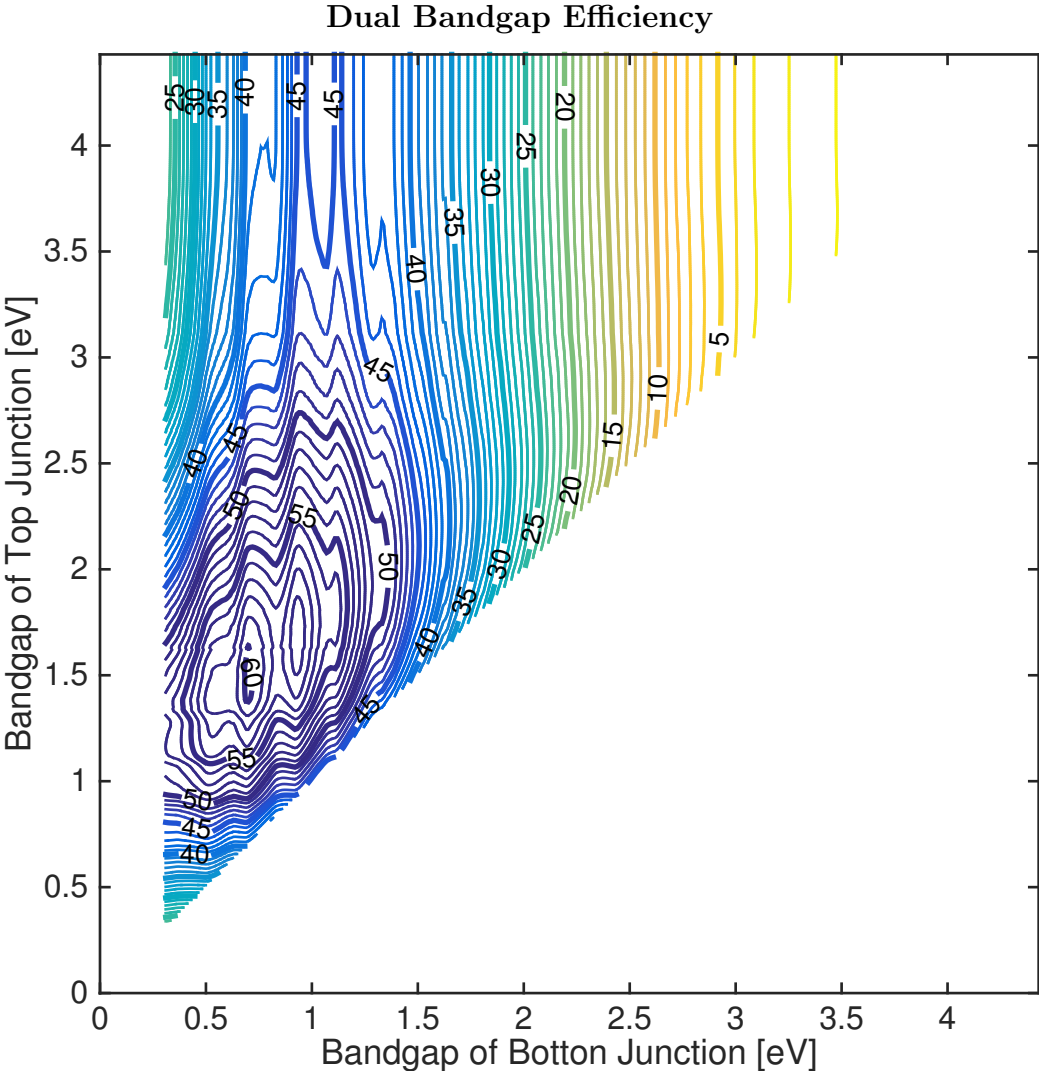


Figure 6.2: Efficiency of dual bandgap solar cells under maximum concentration.

### 6.3 Solar Thermophotovoltaics

We now want to compare the efficiency of a dual bandgap cell with the efficiency of solar thermophotovoltaics. In solar thermophotovoltaics, an intermediate layer absorbs the incident solar radiation. This intermediate layer heats up and emits according to its temperature, emissivity, and the blackbody spectrum. This intermediate layer blackbody emission is absorbed by photovoltaic cells and converted to electricity. If the photovoltaic cells have back mirrors, they can reflect the sub-bandgap photons back to the intermediate source. We derive the efficiency of a solar thermophotovoltaic system, following the work in [86] and [87].

In order to obtain the efficiency of a solar thermophotovoltaic system, we find the temperature of the intermediate layer in steady-state. We assume that the intermediate layer is a perfect blackbody, with unity emissivity. In our analysis, as previously in this chapter, we use the direct solar spectrum, so we can assume that the incident sunlight is within an angular range from  $\theta = 0^\circ$  to  $\theta = 0.27^\circ$ . We assume there is a concentrator with concentration factor  $C$  focusing the sunlight onto the intermediate layer. There is an input area  $A_i$  through which sunlight is admitted through onto the intermediate layer, and an output area  $A_o$  from which blackbody radiation from the intermediate layer is transferred to the photovoltaic cells. We assume the cells and intermediate layer are in vacuum, and the total surface area of the intermediate layer is  $A_i + A_o$ . We balance all the radiative fluxes in order to get the steady-state temperature of the intermediate blackbody layer:

$$\begin{aligned}
 A_i \int_0^\infty C \times S(\lambda) = & \\
 A_i \frac{\pi C}{46211} \int_0^\infty \frac{2hc^2}{\lambda^5} \frac{1}{\exp\left(\frac{hc}{\lambda k_B T_{source}}\right) - 1} & \quad (6.3) \\
 + A_o \pi \int_0^\infty (1 - R) \frac{2hc^2}{\lambda^5} \frac{1}{\exp\left(\frac{hc}{\lambda k_B T_{source}}\right) - 1}, &
 \end{aligned}$$

where  $\lambda$  is the photon wavelength,  $T_{source}$  is the temperature of the intermediate layer,  $R = 0$  for  $\lambda < \lambda_g$ , and  $R$  is a constant reflectivity for  $\lambda > \lambda_g$ , where  $\lambda_g$  is the bandgap wavelength. The term on the left of the represents the incoming sunlight, the first term on the right represents the emission of the intermediate layer into the sky, and the second term on the right represents the emission of the intermediate layer into the photovoltaic cells (minus the sub-bandgap reflection back onto the intermediate layer). We denote  $a = A_i C / A_o$  and we simplify the equation to:

$$\begin{aligned}
a \int_0^\infty S(\lambda) = & \\
a \frac{\pi}{46211} \int_0^\infty \frac{2hc^2}{\lambda^5} \frac{1}{\exp(\frac{hc}{\lambda k_B T_{source}}) - 1} & \quad (6.4) \\
+ \pi \int_0^\infty (1 - R) \frac{2hc^2}{\lambda^5} \frac{1}{\exp(\frac{hc}{\lambda k_B T_{source}}) - 1} &
\end{aligned}$$

We then numerically solve this equation to find  $T_{source}$ . We find the power output of the solar cells with the incident spectrum as the blackbody spectrum with temperature  $T_{source}$ . The efficiency is the power output over the input solar energy. Given a value for the sub-bandgap reflectivity of the photovoltaic cell back mirrors, we find the optimal efficiency as a function of cell bandgap and  $a$ . Efficiency as a function of back mirror sub-bandgap reflectivity is shown in Fig. 6.3. In this calculation, we assume  $\eta_{ext} = 0.3$  for the photovoltaic cells.

## 6.4 Chapter Summary

We see that with solar thermophotovoltaics, we reach an efficiency of  $\approx 60\%$ , a value very similar to that reached by dual bandgap cells. However, in solar thermophotovoltaics, there are two important caveats. The first is that to reach this efficiency, in solar thermophotovoltaics, we also need a 99% sub-bandgap back mirror reflectivity. Additionally, solar thermophotovoltaics requires an intermediate layer at 2224°C, which poses a materials reliability problem. Thus, we can conclude that working on the multiple bandgap cell with air gap intermediate mirrors is the best pathway to high efficiency.

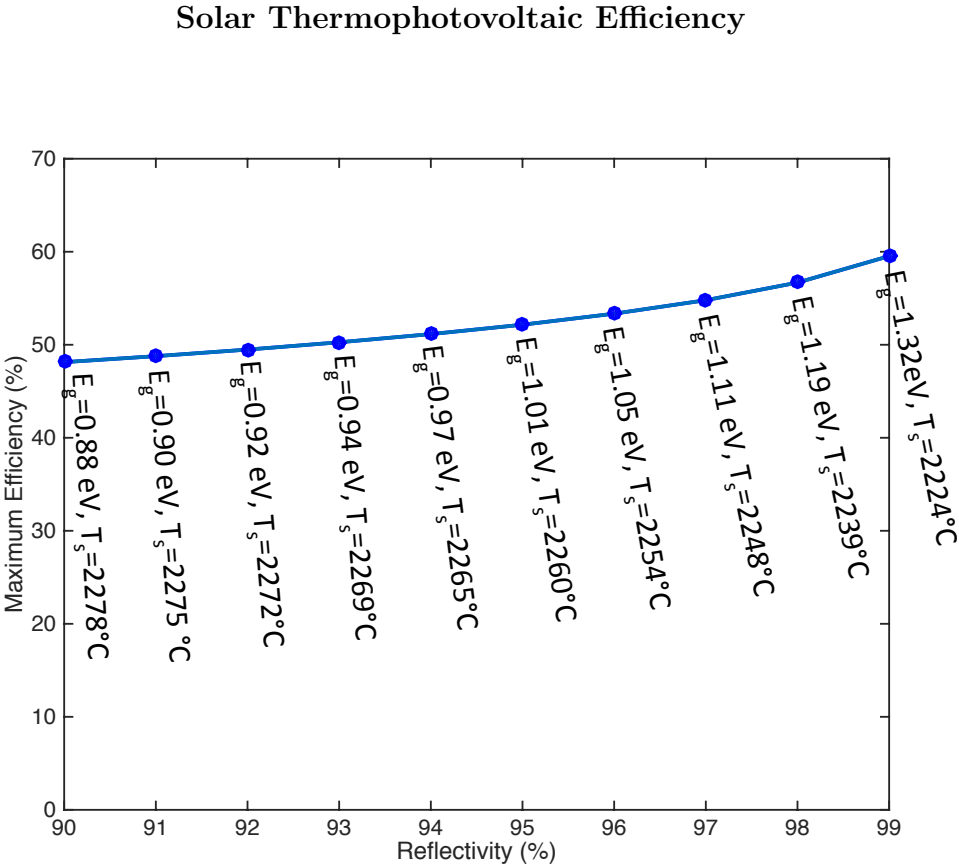


Figure 6.3: Efficiency of solar thermophotovoltaics as a function of back mirror sub-bandgap reflectivity. We denote the temperature of the intermediate layer and the bandgap at each point.

# Bibliography

- [1] Solar Energy Industries Association. (2014). Solar Energy Facts: Q3 2014, [Online]. Available: <http://www.seia.org> (visited on 01/30/2015).
- [2] Shell. (2015). New Lens Scenarios, [Online]. Available: <http://www.shell.com> (visited on 01/30/2015).
- [3] D. Feldman, G. L. Barbose, R. Margolis, N. R. Darghouth, T. James, S. Weaver, A. Goodrich, and R. H. Wiser, “Photovoltaic system pricing trends: historical, recent, and near-term projections - 2013 edition”, Sep. 2013.
- [4] M. A. Green, K. Emery, Y. Hishikawa, W. Warta, and E. D. Dunlop, “Solar cell efficiency tables (version 43): Solar cell efficiency tables”, *Progress in Photovoltaics: Research and Applications*, vol. 22, no. 1, pp. 1–9, Jan. 2014. DOI: 10.1002/pip.2452.
- [5] O. D. Miller, E. Yablonovitch, and S. R. Kurtz, “Strong Internal and External Luminescence as Solar Cells Approach the Shockley-Queisser Limit”, *IEEE Journal of Photovoltaics*, vol. 2, no. 3, pp. 303–311, Jul. 2012. DOI: 10.1109/JPHOTOV.2012.2198434.
- [6] W. Shockley and H. J. Queisser, “Detailed Balance Limit of Efficiency of pn Junction Solar Cells”, *Journal of Applied Physics*, vol. 32, no. 3, pp. 510–519, Mar. 1961. DOI: 10.1063/1.1736034.
- [7] R. T. Ross, “Some Thermodynamics of Photochemical Systems”, *The Journal of Chemical Physics*, vol. 46, no. 12, pp. 4590–4593, Jun. 1967. DOI: 10.1063/1.1840606.
- [8] G. L. Araujo and A. Marti, “Absolute limiting efficiencies for photovoltaic energy conversion”, *Solar Energy Materials and Solar Cells*, vol. 33, no. 2, pp. 213–240, Jun. 1994. DOI: 10.1016/0927-0248(94)90209-7.
- [9] G. Bauhuis, P. Mulder, E. Haverkamp, J. Huijben, and J. Schermer, “26.1% thin-film GaAs solar cell using epitaxial lift-off”, *Solar Energy Materials and Solar Cells*, vol. 93, no. 9, pp. 1488–1491, Sep. 2009. DOI: 10.1016/j.solmat.2009.03.027.
- [10] B. M. Kayes, H. Nie, R. Twist, S. G. Spruytte, F. Reinhardt, I. C. Kizilyalli, and G. S. Higashi, “27.6% Conversion efficiency, a new record for single-junction solar cells under 1 sun illumination”, *IEEE*, Jun. 2011, pp. 4–8. DOI: 10.1109/PVSC.2011.6185831.
- [11] U. Rau, “Reciprocity relation between photovoltaic quantum efficiency and electroluminescent emission of solar cells”, *Physical Review B*, vol. 76, no. 8, p. 085303, Aug. 2007. DOI: 10.1103/PhysRevB.76.085303.

- [12] M. A. Green, “Radiative efficiency of state-of-the-art photovoltaic cells”, *Progress in Photovoltaics: Research and Applications*, vol. 20, no. 4, pp. 472–476, Jun. 2012. DOI: 10.1002/pip.1147.
- [13] E. Yablonovitch, “Statistical ray optics”, *Journal of the Optical Society of America*, vol. 72, no. 7, p. 899, Jul. 1982. DOI: 10.1364/JOSA.72.000899.
- [14] V. Ganapati, C.-S. Ho, and E. Yablonovitch, “Air Gaps as Intermediate Selective Reflectors to Reach Theoretical Efficiency Limits of Multibandgap Solar Cells”, *IEEE Journal of Photovoltaics*, vol. 5, no. 1, pp. 410–417, Jan. 2015. DOI: 10.1109/JPHOTOV.2014.2361013.
- [15] M. A. Steiner, J. F. Geisz, I. Garcia, D. J. Friedman, A. Duda, and S. R. Kurtz, “Optical enhancement of the open-circuit voltage in high quality GaAs solar cells”, *Journal of Applied Physics*, vol. 113, no. 12, p. 123109, 2013. DOI: 10.1063/1.4798267.
- [16] T. Tiedje, E. Yablonovitch, G. Cody, and B. Brooks, “Limiting efficiency of silicon solar cells”, *IEEE Transactions on Electron Devices*, vol. 31, no. 5, pp. 711–716, May 1984. DOI: 10.1109/T-ED.1984.21594.
- [17] M. D. Sturge, “Optical Absorption of Gallium Arsenide between 0.6 and 2.75 eV”, *Physical Review*, vol. 127, no. 3, pp. 768–773, Aug. 1962. DOI: 10.1103/PhysRev.127.768.
- [18] F. Urbach, “The Long-Wavelength Edge of Photographic Sensitivity and of the Electronic Absorption of Solids”, *Physical Review*, vol. 92, no. 5, pp. 1324–1324, Dec. 1953. DOI: 10.1103/PhysRev.92.1324.
- [19] National Renewable Energy Laboratory. (2013). NREL Reports 31.1% Efficiency for III-V Solar Cell, [Online]. Available: <http://www.nrel.gov/news/press/2013/2226.html> (visited on 04/24/2015).
- [20] A. S. Brown and M. A. Green, “Detailed balance limit for the series constrained two terminal tandem solar cell”, *Physica E: Low-dimensional Systems and Nanostructures*, vol. 14, pp. 96–100, Apr. 2002. DOI: 10.1016/S1386-9477(02)00364-8.
- [21] C. H. Henry, “Limiting efficiencies of ideal single and multiple energy gap terrestrial solar cells”, *Journal of Applied Physics*, vol. 51, no. 8, pp. 4494–4500, Jul. 2008. DOI: 10.1063/1.328272.
- [22] A. Martí and G. L. Araújo, “Limiting efficiencies for photovoltaic energy conversion in multigap systems”, *Solar Energy Materials and Solar Cells*, vol. 43, no. 2, pp. 203–222, Sep. 1996. DOI: 10.1016/0927-0248(96)00015-3.
- [23] J. E. Parrott, “The limiting efficiency of an edge-illuminated multigap solar cell”, *Journal of Physics D: Applied Physics*, vol. 12, no. 3, pp. 441–450, Mar. 1979. DOI: 10.1088/0022-3727/12/3/014.

- [24] I. Tobas and A. Luque, “Ideal efficiency of monolithic, series-connected multijunction solar cells”, *Progress in Photovoltaics: Research and Applications*, vol. 10, no. 5, pp. 323–329, Aug. 2002. DOI: 10.1002/pip.427.
- [25] A. D. Vos, “Detailed balance limit of the efficiency of tandem solar cells”, *Journal of Physics D: Applied Physics*, vol. 13, no. 5, p. 839, May 1980. DOI: 10.1088/0022-3727/13/5/018.
- [26] National Renewable Energy Laboratory. (2015). Reference Solar Spectral Irradiance: Air Mass 1.5, [Online]. Available: [rredc.nrel.gov/solar/spectra/am1.5](http://rredc.nrel.gov/solar/spectra/am1.5) (visited on 05/20/2014).
- [27] B. M. Kayes, L. Zhang, R. Twist, I.-K. Ding, and G. S. Higashi, “Flexible Thin-Film Tandem Solar Cells With >30% Efficiency”, *IEEE Journal of Photovoltaics*, vol. 4, no. 2, pp. 729–733, Mar. 2014. DOI: 10.1109/JPHOTOV.2014.2299395.
- [28] T. Takamoto, E. Ikeda, H. Kurita, M. Ohmori, M. Yamaguchi, and M.-J. Yang, “Two-Terminal Monolithic In<sub>0.5</sub>Ga<sub>0.5</sub>P/GaAs Tandem Solar Cells with a High Conversion Efficiency of Over 30%”, *Japanese Journal of Applied Physics*, vol. 36, no. Part 1, No. 10, pp. 6215–6220, Oct. 1997. DOI: 10.1143/JJAP.36.6215.
- [29] X. Sheng, M. H. Yun, C. Zhang, A. M. Al-Okaily, M. Masouraki, L. Shen, S. Wang, W. L. Wilson, J. Y. Kim, P. Ferreira, X. Li, E. Yablonovitch, and J. A. Rogers, “Solar Cells: Device Architectures for Enhanced Photon Recycling in Thin-Film Multijunction Solar Cells (Adv. Energy Mater. 1/2015)”, *Advanced Energy Materials*, vol. 5, no. 1, Jan. 2015. DOI: 10.1002/aenm.201570006.
- [30] O. Miller, “Photonic design: from fundamental solar cell physics to computational inverse design”, PhD thesis, EECS Department, University of California, Berkeley, May 2012.
- [31] G. Lush and M. Lundstrom, “Thin film approaches for high-efficiency III-V cells”, *Solar Cells*, vol. 30, pp. 337–344, May 1991. DOI: 10.1016/0379-6787(91)90066-X.
- [32] M. A. Green, “Enhanced evanescent mode light trapping in organic solar cells and other low index optoelectronic devices”, *Progress in Photovoltaics: Research and Applications*, vol. 19, no. 4, pp. 473–477, Jun. 2011. DOI: 10.1002/pip.1038.
- [33] Z. Yu, A. Raman, and S. Fan, “Fundamental limit of nanophotonic light trapping in solar cells”, *Proceedings of the National Academy of Sciences*, vol. 107, no. 41, pp. 17 491–17 496, Sep. 2010. DOI: 10.1073/pnas.1008296107.
- [34] H. R. Stuart and D. G. Hall, “Thermodynamic limit to light trapping in thin planar structures”, *Journal of the Optical Society of America A*, vol. 14, no. 11, p. 3001, Nov. 1997. DOI: 10.1364/JOSAA.14.003001.
- [35] Z. Yu and S. Fan, “Angular constraint on light-trapping absorption enhancement in solar cells”, *Applied Physics Letters*, vol. 98, no. 1, p. 011 106, 2011. DOI: 10.1063/1.3532099.

- [36] Z. Yu, A. Raman, and S. Fan, “Thermodynamic upper bound on broadband light coupling with photonic structures”, *Physical Review Letters*, vol. 109, no. 17, Oct. 2012. DOI: 10.1103/PhysRevLett.109.173901.
- [37] —, “Fundamental limit of light trapping in grating structures”, *Optics Express*, vol. 18, no. S3, A366, Aug. 2010. DOI: 10.1364/OE.18.00A366.
- [38] L. Zeng, Y. Yi, C. Hong, J. Liu, N. Feng, X. Duan, L. C. Kimerling, and B. A. Alamariu, “Efficiency enhancement in si solar cells by textured photonic crystal back reflector”, *Applied Physics Letters*, vol. 89, no. 11, p. 111111, 2006. DOI: 10.1063/1.2349845.
- [39] E. Garnett and P. Yang, “Light trapping in silicon nanowire solar cells”, *Nano Letters*, vol. 10, no. 3, pp. 1082–1087, Mar. 2010. DOI: 10.1021/nl100161z.
- [40] D. Shir, J. Yoon, D. Chanda, J.-H. Ryu, and J. A. Rogers, “Performance of ultrathin silicon solar microcells with nanostructures of relief formed by soft imprint lithography for broad band absorption enhancement”, *Nano Letters*, vol. 10, no. 8, pp. 3041–3046, Aug. 2010. DOI: 10.1021/nl101510q.
- [41] P. Bermel, C. Luo, L. Zeng, L. C. Kimerling, and J. D. Joannopoulos, “Improving thin-film crystalline silicon solar cell efficiencies with photonic crystals”, *Optics Express*, vol. 15, no. 25, p. 16986, 2007. DOI: 10.1364/OE.15.016986.
- [42] C. Heine and R. H. Morf, “Submicrometer gratings for solar energy applications”, *Applied Optics*, vol. 34, no. 14, p. 2476, May 1995. DOI: 10.1364/AO.34.002476.
- [43] N. Senoussaoui, M. Krause, J. Maller, E. Bunte, T. Brammer, and H. Stiebig, “Thin-film solar cells with periodic grating coupler”, *Thin Solid Films*, vol. 451-452, pp. 397–401, Mar. 2004. DOI: 10.1016/j.tsf.2003.10.142.
- [44] M. D. Kelzenberg, S. W. Boettcher, J. A. Petykiewicz, D. B. Turner-Evans, M. C. Putnam, E. L. Warren, J. M. Spurgeon, R. M. Briggs, N. S. Lewis, and H. A. Atwater, “Enhanced absorption and carrier collection in si wire arrays for photovoltaic applications”, *Nature Materials*, Feb. 2010. DOI: 10.1038/nmat2635.
- [45] K. X. Wang, Z. Yu, V. Liu, Y. Cui, and S. Fan, “Absorption enhancement in ultrathin crystalline silicon solar cells with antireflection and light-trapping nanocone gratings”, *Nano Letters*, vol. 12, no. 3, pp. 1616–1619, Mar. 2012. DOI: 10.1021/nl204550q.
- [46] D. Madzharov, R. Dewan, and D. Knipp, “Influence of front and back grating on light trapping in microcrystalline thin-film silicon solar cells”, *Optics Express*, vol. 19, no. S2, A95, Jan. 2011. DOI: 10.1364/OE.19.000A95.
- [47] P. Kowalczewski, M. Liscidini, and L. C. Andreani, “Engineering gaussian disorder at rough interfaces for light trapping in thin-film solar cells”, *Optics Letters*, vol. 37, no. 23, p. 4868, Nov. 2012. DOI: 10.1364/OL.37.004868.
- [48] S. Eyderman, S. John, and A. Deinega, “Solar light trapping in slanted conical-pore photonic crystals: beyond statistical ray trapping”, *Journal of Applied Physics*, vol. 113, no. 15, p. 154315, 2013. DOI: 10.1063/1.4802442.

- [49] I. Tobias, A. Luque, and A. Marti, “Light intensity enhancement by diffracting structures in solar cells”, *Journal of Applied Physics*, vol. 104, no. 3, p. 034502, 2008. DOI: 10.1063/1.2960586.
- [50] C. Wang, S. Yu, W. Chen, and C. Sun, “Highly efficient light-trapping structure design inspired by natural evolution”, *Scientific Reports*, vol. 3, Jan. 2013. DOI: 10.1038/srep01025.
- [51] E. R. Martins, J. Li, Y. Liu, J. Zhou, and T. F. Krauss, “Engineering gratings for light trapping in photovoltaics: the supercell concept”, *Physical Review B*, vol. 86, no. 4, Jul. 2012. DOI: 10.1103/PhysRevB.86.041404.
- [52] A. Abass, K. Q. Le, A. Al, M. Burgelman, and B. Maes, “Dual-interface gratings for broadband absorption enhancement in thin-film solar cells”, *Physical Review B*, vol. 85, no. 11, Mar. 2012. DOI: 10.1103/PhysRevB.85.115449.
- [53] Z. Xia, Y. Wu, R. Liu, Z. Liang, J. Zhou, and P. Tang, “Misaligned conformal gratings enhanced light trapping in thin film silicon solar cells”, *Optics Express*, vol. 21, no. S3, A548, May 2013. DOI: 10.1364/OE.21.00A548.
- [54] P. Sheng, “Wavelength-selective absorption enhancement in thin-film solar cells”, *Applied Physics Letters*, vol. 43, no. 6, p. 579, 1983. DOI: 10.1063/1.94432.
- [55] M. B. Dühring and O. Sigmund, “Optimization of extraordinary optical absorption in plasmonic and dielectric structures”, *Journal of the Optical Society of America B*, vol. 30, no. 5, p. 1154, Apr. 2013. DOI: 10.1364/JOSAB.30.001154.
- [56] J. Zhu, C.-M. Hsu, Z. Yu, S. Fan, and Y. Cui, “Nanodome solar cells with efficient light management and self-cleaning”, *Nano Letters*, vol. 10, no. 6, pp. 1979–1984, Jun. 2010. DOI: 10.1021/nl9034237.
- [57] P. N. Saeta, V. E. Ferry, D. Pacifici, J. N. Munday, and H. A. Atwater, “How much can guided modes enhance absorption in thin solar cells?”, *Optics Express*, vol. 17, no. 23, p. 20975, Nov. 2009. DOI: 10.1364/OE.17.020975.
- [58] D. Zhou and R. Biswas, “Photonic crystal enhanced light-trapping in thin film solar cells”, *Journal of Applied Physics*, vol. 103, no. 9, p. 093102, 2008. DOI: 10.1063/1.2908212.
- [59] Y. Park, E. Drouard, O. El Daif, X. Letartre, P. Viktorovitch, A. Fave, A. Kaminski, M. Lemiti, and C. Seassal, “Absorption enhancement using photonic crystals for silicon thin film solar cells”, *Optics Express*, vol. 17, no. 16, p. 14312, Jul. 2009. DOI: 10.1364/OE.17.014312.
- [60] C. Eisele, C. E. Nebel, and M. Stutzmann, “Periodic light coupler gratings in amorphous thin film solar cells”, *Journal of Applied Physics*, vol. 89, no. 12, p. 7722, 2001. DOI: 10.1063/1.1370996.

- [61] V. E. Ferry, M. A. Verschuuren, H. B. T. Li, E. Verhagen, R. J. Walters, R. E. I. Schropp, H. A. Atwater, and A. Polman, “Light trapping in ultrathin plasmonic solar cells”, *Optics Express*, vol. 18, no. S2, A237, Jun. 2010. DOI: 10.1364/OE.18.00A237.
- [62] S. Fahr, T. Kirchartz, C. Rockstuhl, and F. Lederer, “Approaching the lambertian limit in randomly textured thin-film solar cells”, *Optics Express*, vol. 19, no. S4, A865, Jun. 2011. DOI: 10.1364/OE.19.00A865.
- [63] J. Grandidier, D. M. Callahan, J. N. Munday, and H. A. Atwater, “Light absorption enhancement in thin-film solar cells using whispering gallery modes in dielectric nanospheres”, *Advanced Materials*, vol. 23, no. 10, pp. 1272–1276, Mar. 2011. DOI: 10.1002/adma.201004393.
- [64] F. Pratesi, M. Buresi, F. Riboli, K. Vynck, and D. S. Wiersma, “Disordered photonic structures for light harvesting in solar cells”, *Optics Express*, vol. 21, no. S3, A460, Apr. 2013. DOI: 10.1364/OE.21.00A460.
- [65] D. M. Callahan, J. N. Munday, and H. A. Atwater, “Solar cell light trapping beyond the ray optic limit”, *Nano Letters*, vol. 12, no. 1, pp. 214–218, Jan. 2012. DOI: 10.1021/nl203351k.
- [66] X. Sheng, S. G. Johnson, J. Michel, and L. C. Kimerling, “Optimization-based design of surface textures for thin-film si solar cells”, *Optics Express*, vol. 19, no. S4, A841–A850, Jul. 2011. DOI: 10.1364/OE.19.00A841.
- [67] MATLAB, *version 8.4.0 (R2014b)*. Natick, Massachusetts: The MathWorks Inc., 2014.
- [68] M. B. Giles and N. A. Pierce, “An introduction to the adjoint approach to design”, *Flow, Turbulence and Combustion*, vol. 65, no. 3-4, pp. 393–415, 2000.
- [69] (2015). Lumerical Solutions, Inc., [Online]. Available: <http://www.lumerical.com/tcad-products/fdtd/>.
- [70] W. Murray and M. L. Overton, “A projected lagrangian algorithm for nonlinear min-max optimization”, *SIAM Journal on Scientific and Statistical Computing*, vol. 1, no. 3, pp. 345–370, Sep. 1980. DOI: 10.1137/0901025.
- [71] V. Ganapati, L. Waller, and E. Yablonovitch, “Adjoint Method for Phase Retrieval”, in *Classical Optics 2014*, ser. OSA Technical Digest (online), Optical Society of America, Jun. 2014, CW4C.2. DOI: 10.1364/COSI.2014.CW4C.2.
- [72] G. Scranton, S. Bhargava, V. Ganapati, and E. Yablonovitch, “Single spherical mirror optic for extreme ultraviolet lithography enabled by inverse lithography technology”, *Optics Express*, vol. 22, no. 21, pp. 25 027–25 042, Oct. 2014. DOI: 10.1364/OE.22.025027.
- [73] C. Battaglia, C.-M. Hsu, K. Sderstrm, J. Escarr, F.-J. Haug, M. Charriare, M. Boccard, M. Despeisse, D. T. L. Alexander, M. Cantoni, Y. Cui, and C. Ballif, “Light trapping in solar cells: can periodic beat random?”, *ACS Nano*, vol. 6, no. 3, pp. 2790–2797, Mar. 2012. DOI: 10.1021/nn300287j.

- [74] L. Fraas and L. Minkin, “TPV History from 1990 to Present & Future Trends”, vol. 890, AIP, 2007, pp. 17–23. DOI: 10.1063/1.2711716.
- [75] N.-P. Harder and P. Wurfel, “Theoretical limits of thermophotovoltaic solar energy conversion”, *Semiconductor Science and Technology*, vol. 18, no. 5, S151–S157, May 2003. DOI: 10.1088/0268-1242/18/5/303.
- [76] V. L. Teofilo, P. Choong, J. Chang, Y.-L. Tseng, and S. Ermer, “Thermophotovoltaic Energy Conversion for Space ”, *The Journal of Physical Chemistry C*, vol. 112, no. 21, pp. 7841–7845, May 2008. DOI: 10.1021/jp711315c.
- [77] R. E. Nelson, “A brief history of thermophotovoltaic development”, *Semiconductor Science and Technology*, vol. 18, no. 5, S141–S143, May 2003. DOI: 10.1088/0268-1242/18/5/301.
- [78] J. Gee, J. Moreno, Shawn-Yu Lin, and J. Fleming, “Selective emitters using photonic crystals for thermophotovoltaic energy conversion”, IEEE, 2002, pp. 896–899. DOI: 10.1109/PVSC.2002.1190724.
- [79] Y. X. Yeng, W. R. Chan, V. Rinnerbauer, J. D. Joannopoulos, M. Soljacic, and I. Celanovic, “Performance analysis of experimentally viable photonic crystal enhanced thermophotovoltaic systems”, *Optics Express*, vol. 21, no. S6, A1035, Nov. 2013. DOI: 10.1364/OE.21.0A1035.
- [80] U. Guler, A. Boltasseva, and V. M. Shalaev, “Refractory Plasmonics”, *Science*, vol. 344, no. 6181, pp. 263–264, Apr. 2014. DOI: 10.1126/science.1252722.
- [81] G. V. Naik, J. L. Schroeder, X. Ni, A. V. Kildishev, T. D. Sands, and A. Boltasseva, “Titanium nitride as a plasmonic material for visible and near-infrared wavelengths”, *Optical Materials Express*, vol. 2, no. 4, p. 478, Apr. 2012. DOI: 10.1364/OME.2.000478.
- [82] J. J. Werth, “Thermo-photovoltaic converter with radiant energy reflective means”, pat. US3331707 A, U.S. Classification 136/253, 136/205, 136/256; International Classification H01L31/04; Cooperative Classification Y02E10/50, H01L31/0406; European Classification H01L31/04B, Jul. 1967.
- [83] E. Yablonovitch, T. Gmitter, J. P. Harbison, and R. Bhat, “Extreme selectivity in the lift-off of epitaxial GaAs films”, *Applied Physics Letters*, vol. 51, no. 26, p. 2222, 1987. DOI: 10.1063/1.98946.
- [84] R. Swanson, “Silicon photovoltaic cells in thermophotovoltaic energy conversion”, IRE, 1978, pp. 70–73. DOI: 10.1109/IEDM.1978.189354.
- [85] H. A. Atwater, personal communication, Nov. 3, 2014.
- [86] R. Swanson, “A proposed thermophotovoltaic solar energy conversion system”, *Proceedings of the IEEE*, vol. 67, no. 3, pp. 446–447, 1979. DOI: 10.1109/PROC.1979.11270.

- [87] P. Würfel and W. Ruppel, “Upper limit of thermophotovoltaic solar-energy conversion”, *IEEE Transactions on Electron Devices*, vol. 27, no. 4, pp. 745–750, Apr. 1980. DOI: 10.1109/T-ED.1980.19931.